2010

# Optimization Of Process Parameters For Reduced Thickness Cigses Thin Film Solar Cells

Shirish A. Pethe
*University of Central Florida*

# OPTIMIZATION OF PROCESS PARAMETERS FOR REDUCED THICKNESS CIGSeS THIN FILM SOLAR CELLS

by

SHIRISH A. PETHE
B.S. University of Mumbai, 2001
M.S. University of South Florida, 2004

A dissertation submitted in partial fulfillment of the requirements
for the degree of Doctor of Philosophy
in the Department of Electrical Engineering and Computer Science
in the College of Engineering and Computer Science
at the University of Central Florida
Orlando, Florida

Fall Term
2010

Major Professor: Neelkanth G. Dhere

# ABSTRACT

With the advent of the 21st century, one of the serious problems facing mankind is harmful effects of global warming. Add to that the ever increasing cost of fuel and the importance of development of clean energy resources as alternative to fossil fuel has becomes one of the prime and pressing challenges for modern science and technology in the 21st century. Recent studies have shown that energy related sources account for 50% of the total emission of carbon dioxide in the atmosphere. All research activities are focused on developing various technologies that are capable of converting sunlight into electricity with high efficiency and can be produced using a cost-effective process. One of such technologies is the $CuIn_{1-x}Ga_xSe_2$ (CIGS) and its alloys that can be produced using cost-effective techniques and also exhibit high photo-conversion efficiency. The work presented here discusses some of the fundamental issues related to high volume production of CIGS thin film solar cells. Three principal issues that have been addressed in this work are effect of reduction in absorber thickness on device performance, micrononuniformity involved with amount of sodium and its effect on device performance and lastly the effect of working distance on the properties of molybdenum back contact. An effort has been made to understand the effect of absorber thickness on PV parameters and optimize the process parameters accordingly. Very thin (<1 μm) absorber film were prepared by selenization using metallorganic selenium source in a conventional furnace and by RTP using Se vapor. Sulfurization was carried out using $H_2S$ gas. Devices with efficiencies reaching 9% were prepared for very thin (<1 μm) CIGS and CIGSeS thin films. It was shown through this work that the absorber thickness reduction of 64% results in the efficiency drop of only 32%. With further optimization of the reaction process of the absorber layer as well as the other layers

higher efficiencies can be achieved. The effect of sodium on the device performance is experimentally verified in this work. To the best of our knowledge the detrimental effect of excess sodium has been verified by experimental data and effort has been made to correlate the variation in PV parameter to theoretical models of effect of sodium. It has been a regular practice to deposit thin barrier layer prior to molybdenum deposition to reduce the micrononuniformities caused due to nonuniform out diffusion of sodium from the soda lime glass. However, it was proven in this work that an optimally thick barrier layer is necessary to reduce the out diffusion of sodium to negligible quantities and thus reduce the micrononuniformities. Molybdenum back contact deposition is a bottleneck in high volume manufacturing due to the current state of art where multi layer molybdenum film needs to be deposited to achieve the required properties. In order to understand and solve this problem experiments were carried out. The effect of working distance (distance between the target and the substrate) on film properties was studied and is presented in this work. During the course of this work efforts were taken to carry out a systematic and detailed study of some of the fundamental issues related to CIGS technology and particular for high volume manufacturing of CIGS PV modules and lay a good foundation for further improvement of PV performance of CIGS thin film solar cells prepared by the two step process of selenization and sulfurization of sputtered metallic precursors.

# ACKNOWLEDGMENTS

I would like to take this opportunity to express my deepest gratitude to Dr. Neelkanth G. Dhere for giving me an opportunity to work on a stimulating topic like CIGSeS thin film solar cells. It was a great experience to work under him and I learned a lot under him and would like to show my appreciation for constant guidance and help. I would also like to thank Dr. Aarvinda Kar, Dr. Helge Heinrich, Dr. Kalpathy Sundaram and Dr. Kristine Klemenz for agreeing to be on my dissertation committee and also for their invaluable suggestions during the course of this research. I would like to thank the following people for their assistance during this research: Dr. Helio Moutinho, Bobby To, Keith Emery from National Renewable Energy Laboratory.

Special words of thanks go to my colleagues Dr. Sachin Kulkarni, Dr. Vinay Hadagali, Dr. Parag Vasekar, Dr. Anant Jahagirdar, Dr. Ankur Kadam, Mr. Bhaskar Kumar, Mr. Ashwani Kaul, Ms. Jyoti Shirolikar, Mr. Upendra Avachat, Dr. Dhaval Shah, and all other people at the Florida Solar Energy Center (FSEC) and my friends Dr. Ajay Karakoti, Dr Vinu Krishnan. You guys made my stay at FSEC and UCF wonderful and memorable.

Last but not the least I would like to thank my parents and my wife, Meenal for their strong belief in me and also for their constant understanding and support.

# TABLE OF CONTENTS

# LIST OF FIGURES

# LIST OF TABLES

# LIST OF ACRONYMS

| | |
|---|---|
| CIS | Copper Indium Diselenide |
| CIGS | Copper Indium Gallium Diselenide |
| CIGSeS | Copper Indium Gallium Selenide Sulfide |
| CdS | Cadmium Sulfide |
| i:ZnO | Intrinsic Zinc Oxide |
| ZnO:Al | Aluminum doped Zinc Oxide |
| J | Current Density ($mA/cm^2$) |
| $J_0$ | Reverse Saturation Current Density ($mA/cm^2$) |
| $J_D$ | Dark Current Density ($ma/cm^2$) |
| Q | Electronic Charge, $1.6 \times 10^{-19}$ C |
| A | Diode Ideality Factor |
| K | Botlzmann's Constant , $8.61 \times 10^{-5}$ eV/°C |
| $R_s$ | Series Resistance (Ohm) |
| $R_p$ | Shunt or Parallel Resistance (Ohm) |
| V | Biased Voltage (Volts) |
| $J_{ph}$ | Photo generated Current Density ($mA/cm^2$) |
| $J_m$ | Maximum Current Density ($mA/cm^2$) |
| $V_m$ | Maximum Voltage (Volts) |
| $W_d$ | Depletion Width |
| $V_{oc}$ | Open Circuit Voltage (Volts) |
| $J_{sc}$ | Short Circuit Current Density ($mA/cm^2$) |
| FF | Fill Factor (%) |
| $P_s$ | Irradiated Power Density ($mW/cm^2$) |
| $\eta$ | Efficiency (%) |
| $V_{bi}$ | Built-in Voltage (Volts) |
| kV | kilo volts |
| eV | electron volts |
| EPMA | Electron Probe Micro Analysis |

| | |
|---|---|
| SEM | Scanning Electron Microscopy |
| AES | Auger Electron Spectroscopy |
| EDS | Energy Dispersive X-ray Spectroscopy |
| EBSD | Electron Backscattered Diffraction |
| XRD | X-ray diffraction |
| QE | Quantum Efficiency |
| nm | Nanometer ($10^{-9}$ meter) |
| μm | Micrometer ($10^{-6}$ meter) |

# CHAPTER 1 INTRODUCTION

With the advent of the 21st century, one of the serious problems facing mankind is harmful effects of global warming. With increasing pollution and the increase in concentration of carbon dioxide and other greenhouse gases (methane, nitrous oxide, PFCs, HFCs and $SF_6$) the effect of global warming on climatic changes seems to be multiplying with every passing year. Add to that the ever increasing cost of fossil fuel and the importance of development of clean energy resources as alternative to fossil fuel has becomes one of the prime and pressing challenges for modern science and technology in the 21st century.

Recent studies have shown that energy related sources account for 50% of the total emission of carbon dioxide in the atmosphere [1]. Finding alternative energy sources becomes the principal path towards stabilization of the greenhouse gas emission. Some of the major contenders for the alternative clean resources are hydroelectric, tidal, nuclear, wind and solar energy. Of all these renewable energy sources, photovoltaic is the most promising one as a future energy technology. The solar cells and modules are already cost effective in many stand-alone applications in remote locations. Examples are telecommunications towers, weather monitors, railroad crossings, forest fire watch towers, water pumping, agriculture, health care, vaccine refrigerators, village education, farm houses, and consumer products, household appliances, etc. From the utilities point of view, three of the most attractive advantages of photovoltaic at present are its reliability, the possibility to provide energy to shave off peak loads in certain areas and distributed generation. For this purpose, the cost of photovoltaic (PV) electricity must be reduced from the present 21-30¢/kWh to 6-8¢/kWh. A photovoltaic generation station 140 x 140 km in area at an average US location could generate all the electricity needed in the US ($2.5 \times 10^{12}$ kW-

h/yr), assuming a system efficiency of 10%, a balance-of-systems efficiency of 81% and a system packing factor of 50% [2]. Therefore, all research activities are focused on developing various technologies that are capable of converting sunlight into electricity with high efficiency and can be produced using a cost-effective process. One of such technologies is the $CuIn_{1-x}Ga_x$ Se and its alloys that can be produced using cost-effective techniques and also exhibit high photo-conversion efficiency. The research carried out on this technology is presented in the following chapters. In order to improve the performance of the solar cell, it is essential to understand the semiconductor fundamentals that are discussed in the following paragraphs. Chapter two discusses the materials aspects of CIGS thin film solar cells including the other layers involved in formation of a complete device. The experimental techniques in terms of the preparation of the solar cell device as well as the characterization techniques that were used in this research are discussed in chapter three. The study carried out and the obtained results are presented in chapter four followed by the conclusions and suggestion for some future work in chapter five.

## 1.1 Overview of Photovoltaics

The photovoltaic effect is the process of direct conversion of sunlight into electrical energy. This effect was first observed by Henri Becquerel in 1839. The major advantage of these photovoltaic systems is that they tap an almost inexhaustible resource that is free and globally available. Even though the photovoltaic effect was first observed in 1839, the first practical cell with an efficiency of 6% was developed by Chapin et al at Bell Labs in 1954 [3]. Also in the same year Reynolds et al developed a heterojunction $CdS/CuS_2$ solar cell also with an efficiency

of 6% [4]. There are two main categories of solar cell technologies; crystalline silicon and thin film.

## 1.2 Thin Film Solar Cells

Currently the photovoltaics market is dominated by crystalline silicon; however, the thin film technologies are slowly increasing their total market share. One of the major reasons for the interest and development of thin film solar cells is their potential low cost. Moreover, silicon is an indirect bandgap material so the thickness required for absorption of most of the solar spectrum is 100-200 μm. On the other hand, direct bandgap materials require thickness of only 1-2 μm. The thin film technologies use simpler device processing techniques such as evaporation, sputtering, etc. for large area modules. The designs of most thin film technologies have common processing techniques so the manufacturing costs are very similar. Hence, the choice of any technology is based on the factors such as highest achievable conversion efficiency, reliability, availability of materials and environmental concerns.

At present, research is being carried out on the alloys of amorphous hydrogenated silicon (a-Si:H), Cadmium Telluride (CdTe), and Copper Indium Diselenide (CIS) as major contenders for large scale production, as all of them are direct bandgap semiconductors. Another factor which works in favor of the thin film technologies is the processing cost. The chronological evolution of thin film solar cells is shown in figure 1 [5]. Highest efficiency of 20.3% has been achieved for CIGS thin film solar cells and 16.5% efficiency has been achieved for CdTe thin film solar cells. The highest independently confirmed terrestrial cell and sub-module efficiencies are tabulated in table I [6].

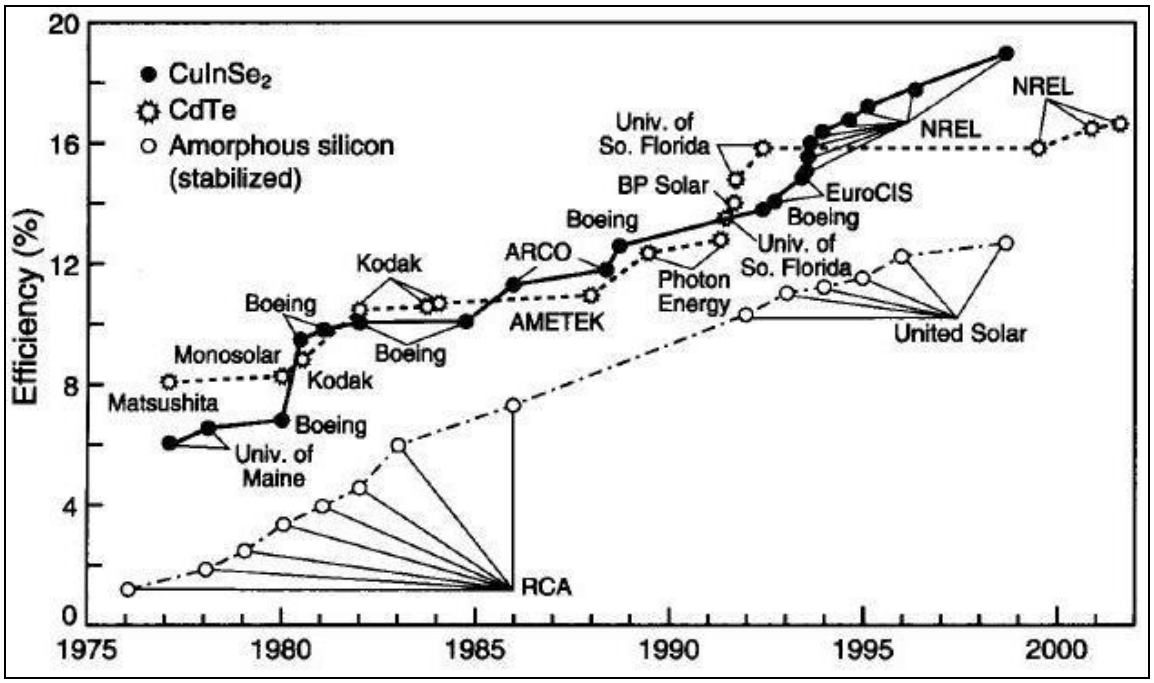


Figure 1.1: Chronological Evolution of Small Area Thin Film Solar Cell Efficiencies

Table 1.1: Confirmed Terrestrial Cell and Submodule Efficiencies Measured under the Global AM1.5 Spectrum (1000 W/m2) at 25 °C

| Classification | Eff. (%) | Area ($cm^2$) | $V_{oc}$ (V) | $J_{sc}$ (mA/$cm^2$) | FF (%) | Test Center (date) | Description |
|---|---|---|---|---|---|---|---|
| Silicon Cells | | | | | | | |
| Si (crystalline) | 24.7±0.5 | 4 (da) | 0.706 | 42.2 | 82.8 | Sandia (3/99) | UNSW PERL |
| Si (multicrystalline) | 20.3±0.5 | 1.002 (ap) | 0.664 | 37.7 | 80.9 | NREL (5/04) | FhG-ISE |
| Si (thin film transfer) | 16.6±0.4 | 4.017 (ap) | 0.645 | 32.8 | 78.2 | FhG-ISE (7/01) | Uni. Of Stuttgart (45µm thick) |
| Si (thin film submodule) | 10.4±0.3 | 94.0 (ap) | 0.492 | 29.5 | 72.1 | FhG-ISE (8/07) | CSG Solar (1–2mm on glass; 20 cells) |
| III-V cells | | | | | | | |
| GaAs (crystalline) | 25.1±0.8 | 3. 91 (t) | 1.022 | 28.2 | 87.1 | NREL (3/90) | Kopin, AlGaAs window |

| | | | | | | | |
|---|---|---|---|---|---|---|---|
| GaAs (thin film) | 24.5±0.5 | 1.002 (ap) | 1.029 | 28.8 | 82.5 | FhG-ISE (5/05) | Radboud U., NL |
| GaAs (multicrystalline) | 18.2 ±0.5 | 4.011 (t) | 0.994 | 23.0 | 79.7 | NREL (11/95) | RTI, Ge substrate |
| InP (crystalline) | 21.9±0.7 | 4.02 (t) | 0.878 | 29.3 | 85.4 | NREL (4/90) | Spire, epitaxial |
| Polycrystalline thin film cells | | | | | | | |
| CIGS (cell) | 18.8±0.6 | 1.00(ap) | 0.703 | 34.0 | 78.7 | FhG-ISE (8/06) | NREL, CIGS on glass |
| CIGS (submodule) | 16.6±0.4 | 16.0 (ap) | 0.661 | 33.4 | 75.1 | FhG-ISE (3/00) | U. Uppsala, 4 serial cells |
| CdTe (cell) | 16.5±0.5 | 1.032 (ap) | 0.845 | 25.9 | 75.5 | NREL (9/01) | NREL, mesa on glass |
| Amorphous/Nanocrystalline Si cells | | | | | | | |
| Si (amorphous) | 9.5± 0.3 | 1.070 (ap) | 0.859 | 17.5 | 63.0 | NREL (4/03) | U. Neuchatel |
| Si (nanocrystalline) | 10.1±0.2 | 1.199 (ap) | 0.539 | 24.4 | 76.6 | JQA (12/97) | Kaneka (2 μm on glass) |
| Photochemical cells | | | | | | | |
| Dye sensitized | 10.4±0.3 | 1.004 (ap) | 0.729 | 21.8 | 65.2 | AIST (8/05) | Sharp |
| Dye sensitized (submodule) | 7.9± 0.3 | 26.48 (ap) | 6.27 | 2.01 | 62.4 | AIST (6/07) | Sharp |
| Organic | | | | | | | |
| Organic Polymer | 5.15±0.3 | 1.021 (ap) | 0.876 | 9.40 | 62.5 | NREL (12/06) | Konarka |
| Multijunction devices | | | | | | | |
| GaInP/GaAs/Ge | 32.0±1.5 | 3.989(t) | 2.622 | 14.37 | 85.0 | NREL (1/03) | Spectrolab (monolithic) |
| GaInP/GaAs | 30.3 | 4.0(t) | 2.488 | 14.22 | 85.6 | JQA (4/96) | Japan Energy (monolithic) |
| GaAs/CIS (thin film) | 25.8±1.3 | 4.00(t) | - | - | - | NREL (11/89) | Kopin/ Boeing (4 terminal) |
| a-Si/μc-Si (thin submodule) | 11.7±0.4 | 14.23 (ap) | 5.462 | 2.99 | 71.3 | AIST (9/04) | Kaneka (thin film) |

## 1.3 CIS Thin Film Technology

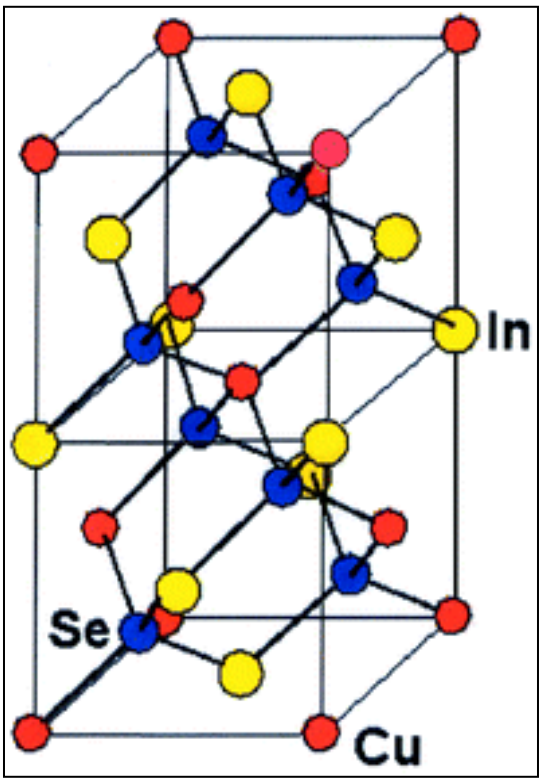


Figure 1.2: Chalcopyrite structure of CIS Alloy

$CuInSe_2$ (CIS) is a ternary alloy belonging to the I-III-VI2 compound semiconductor group. As shown in figure 1.2 CIS lattice elements are tetrahedrally coordinated like all adamanite semiconductors. Each Cu and In atom has four bonds with Se (VI) atom. In turn each Se atom has two bonds to Cu and two more to In. Since the strength of the I-VI and III-VI bonds are in general different, the ratio of lattice constants c/a is not exactly 2. The quantity 2-c/a (which is –0.01 in $CuInSe_2$, +0.04 in $CuGaSe_2$) is a measure of the tetragonal distortion in chalcopyrites. CuInSe2 exhibits 142d symmetry, its atomic coordinates are as follows: four copper atoms at (0,0,0); (½,½,½); (½,0,¾); and (0,½,¼); four indium atoms at (0,0,½); (½,½,0); (½,0,¼); and (0,½,¾); and eight selenium atoms at (u,¼,⅛); (-u,¾,⅛); (¾,u,⅞); (¼,-u, ⅞); (½+u,¾,⅝); (½-u,¼,⅝); (¼,u+½,⅜); and (¾,½-u, ⅜). CIS has a bandgap of ~1.0 eV and one of

the highest reported absorption coefficients (3.6E5 $cm^{-1}$) [7]. The distinguishing characteristic of the family of these materials as compared to other semiconductors is the large number of crystal structures and phases. Moreover, none of these phases are a line compound that is the phases are observed over a range of composition. Even the pure single phases exhibit about 1% (~$10^{20}/cm^3$) point defects such as vacancies without decomposition.

The properties of CIS depend strongly on its composition, and the doping of CIS is controlled by the intrinsic defects. Hence, either p-type or n-type CIS can be obtained if the material is grown Cu-poor and p-type if Cu-rich film is grown. When the film is grown in the slightly Cu-poor regime the presence of copper vacancies (acceptor defects) can make the film p-type. However, if the material is grown in more Cu-poor regime then the excess indium takes the position of copper sites in the lattice ($In_{Cu}$, indium on copper antisites, donor defects). This leads to the film being grown as a n-type film. The Cu-rich films are highly conductive due to acceptor defects (copper atoms on indium sites). The n-type In-rich films are highly resistive due to the donor defects (indium on copper sites) and acceptor defects (copper vacancies) occurring at the same time. Even with total potential lattice defect concentrations of ~$10^{20}$ /$cm^3$ the net carrier concentrations in CIS absorber films are typically ~$10^{16\text{-}17}/cm^3$. This means that there must be either complete compensation or only a small fraction of the total defect population can be electrically active (or both) [8].

The presence of a thin surface layer of $CuIn_3Se_5$ has been indicated in some recent studies. This is termed as the ordered vacancy compound (OVC), a defect chalcopyrite which is In rich [9]. The OVC has a bandgap of ~1.3 eV. As compared to binary compounds the ternary compound CIS is more tolerant to small deviations from stoichiometry. As mentioned earlier CIS

films grown in the Cu-rich regime can be highly conductivity and p-type. However, this results in degradation of device performance and this could be attributed to the formation of copper selenide species that are highly conductive and can result in short circuit of the junction. This behavior is explained based on the Cu-In-Se ternary phase diagram [10] shown in figure 1.3. In order to achieve good device performance, the composition needs to be slightly In rich. As the metal ratio (I/III) approaches unity the carrier concentration increases which results in better cell performance. In Se rich films, both Cu and In vacancies yield strongly p-type films. Simultaneous formation of oppositely charged defects in the In rich films may lead to a highly compensated, highly resistive n or p-type films. The efficient self-doping ability of $CuInSe_2$ has been attributed to the exceptionally low formation energy of Cu vacancies and to the existence of a shallow Cu vacancy acceptor level.

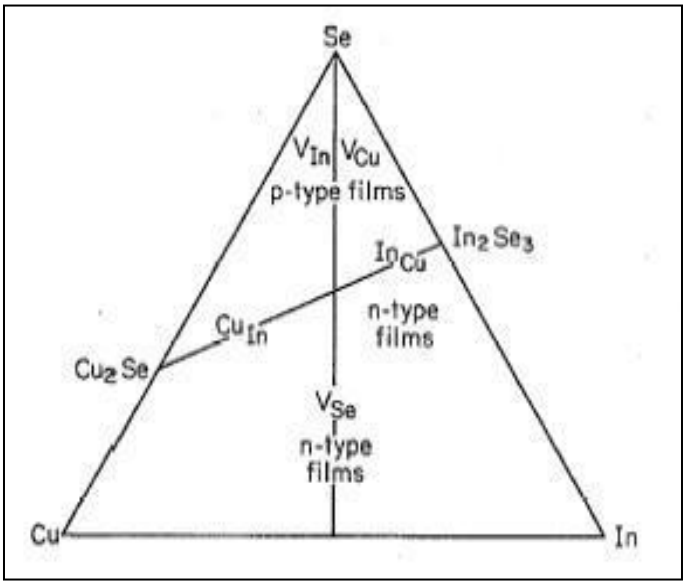


Figure 1.3: Ternary Phase Diagram for Cu-In-Se system

This complex ternary diagram can be reduced to a simpler pseudo-binary phase diagram along the tie line between $Cu_2Se$ and $In_2Se_3$ [11]. The simplified pseudo binary phase diagram is

shown in figure 1.4. As seen from the phase diagram, the α-phase (CuInSe2) lies in a very narrow range of 24 to 24.5% of copper at room temperature. At growth temperature between 500 °C to 550 °C, the α-phase exists in the range of 22 to 24.5 at% Cu. As per the phase diagram the cooling of slightly Cu-poor composition indicates the presence of additional β-phase ($CuIn_3Se_5$) also known as ordered defect compound.

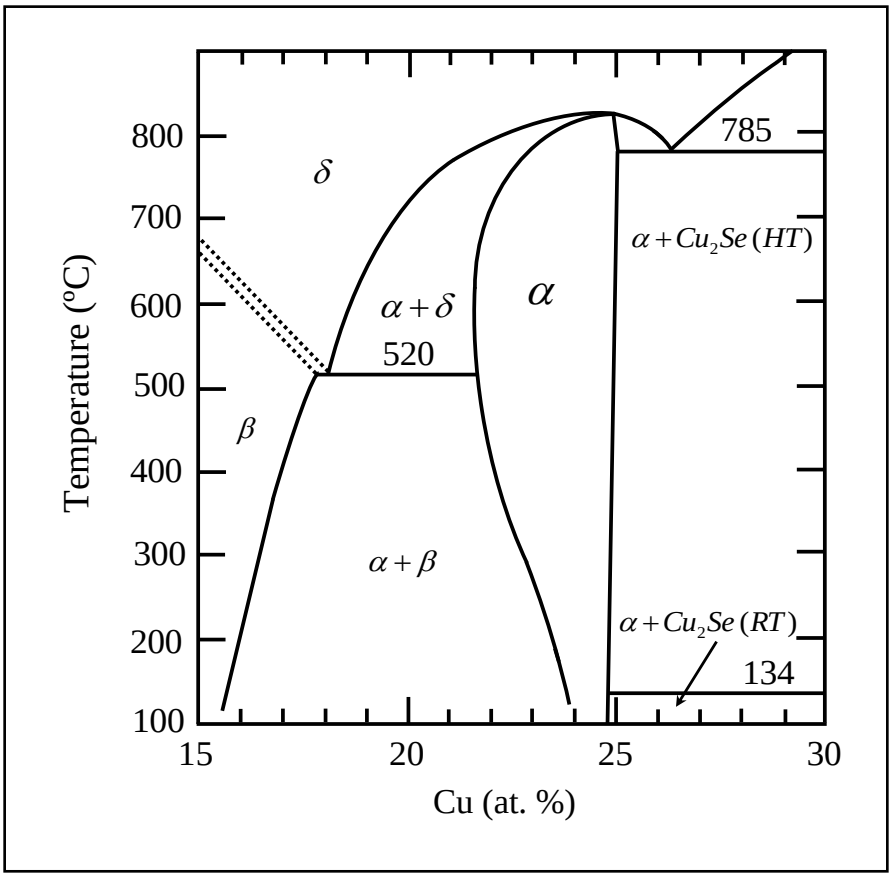


Figure 1.4: Pseudobinary In2Se3–Cu2Se equilibrium phase diagram for compositions around the CuInSe2 chalcopyrite phase (Redrawn) [11]

The first thin film CIS solar cell was produced by the evaporation of CIS as a compound [12]. Some of the techniques being researched for deposition of CIS films include three-source evaporation [13][14][15], laser ablation [16][17], flash evaporation [18][19], vapor transport

[20], spray pyrolysis [21][22], sputtering [23], liquid phase epitaxy [24][25], electrodeposition [26][27], screen printing [28] and selenization of metallic layers [29][30][31]. CIS films can be produced by co-evaporation or sequential evaporation of elemental sources. In co-evaporated CIS films, the composition of the materials with regard to the metal ratios corresponds to the evaporation rates whereas in sequentially evaporated CIS films, it corresponds to the thickness. Co-evaporation of the elemental sources gives better device quality films as compared to films prepared by the two step process. But for commercial purposes two step process is preferred over co-evaporation because it does not require as stringent control over evaporation rates. The technique of sputtering of precursors for the $CuInSe_2$ absorber layer was pioneered by ARCO Solar. Later Shell Solar developed the process further. The two stage process was developed by ARCO Solar [2]. The two stage process consists of the deposition of the Cu-In metallic precursors on Mo coated substrate by sputtering. The metallic precursors are later annealed in diluted $H_2Se$ ambient. $H_2Se$ breaks down to produce selenium which reacts with the metallic precursors to form $CuInSe_2$. However, $H_2Se$ gas is very toxic and hazardous with the time weighted average threshold limit value (TWA-TLV) of 0.05 ppm. $H_2Se$ is usually stored in high pressure cylinders (~20 $kgf/cm^2$). Metalorganic selenides, such as diethyl selenide (DESe), dimethyl selenide (DMSe) and ditertialbutylselenide are being used as alternative candidates for the Se source for metal organic chemical vapor deposition (MOCVD) of ZnSe and other chalcogenides [32]. The metalorganic selenides are liquids at room temperature and are stored at atmospheric pressure in glass or stainless steel bubblers. Hence it involves less danger of wide spread leakage as compared to $H_2Se$. Even though the TWA-TLV of DESe or DMSe is 0.2 mg/m3, they are regarded as safer alternatives to $H_2Se$ in potential leakage risk. Chichibu et al.

first demonstrated the possibility of using DESe as selenium source for the preparation of I-III-VI2 based absorber [32]. Earlier, $CuIn_{1-x}Ga_xSe_{2-y}S_{2y}$ (CIGSeS) thin film solar cell with an efficiency of 13.73% has been fabricated at the FSEC PV Materials Laboratory using DESe as selenium source [33].

## 1.4 CIGS Thin Film Solar Cells

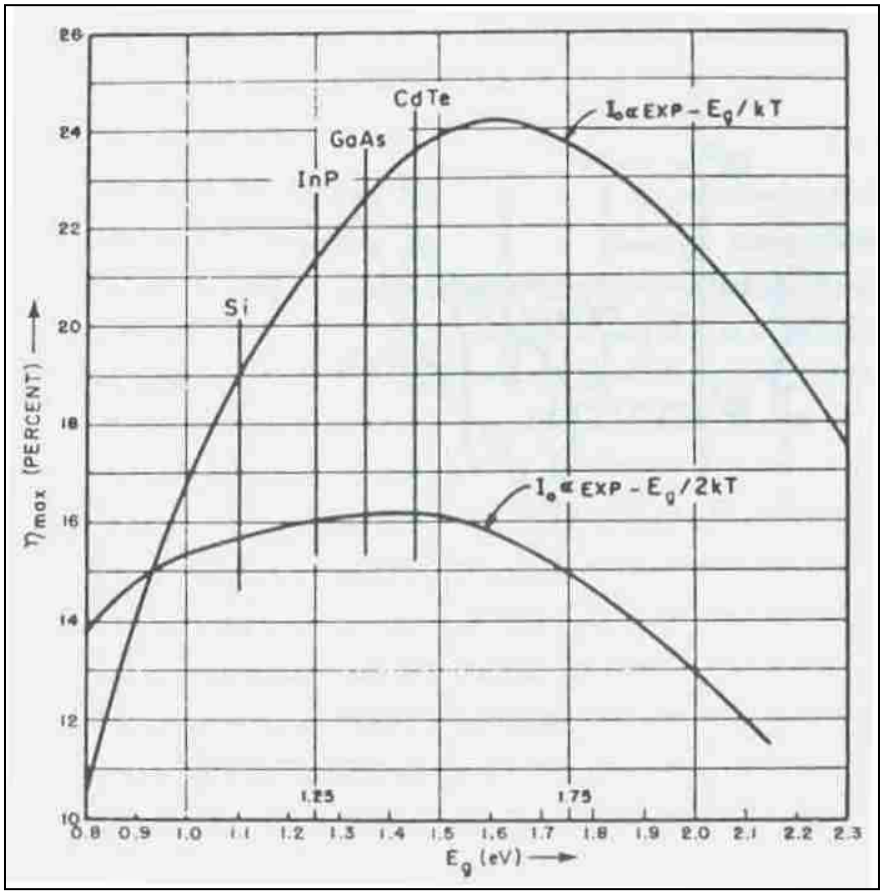


Figure 1.5: Theoretical Analysis of Device Efficiency versus Semiconductor Bandgap

The most optimum condition for application of solar cells would be to maximize both the short circuit current density ($J_{sc}$) and the open circuit voltage ($V_{oc}$). Jsc can be maximized by absorbing as much incident light as possible that means to have a semiconductor with small bandgap with a high absorption coefficient over a wide energy range. Moreover, the material

properties need to be improved, such that the minority carrier lifetime increases leading to increased collection of electrons at the contacts without recombination. $V_{oc}$ can be maximized by decreasing the forward current driven by the photo-induced potential difference to be as small as possible. This forward current reduces the voltage built up by the incident light. The forward current is primarily dependent on the bandgap of the material. Thus, maximization of $V_{oc}$ needs higher bandgap. Hence, it can be concluded that an optimum bandgap exists that maximizes both $J_{sc}$ and $V_{oc}$. Theoretical analysis has shown that this optimum bandgap is ~1.5 eV and results of some of first calculation for various semiconductors are shown in figure 1.5[34].

The bandgap of CIS is ~1.02 eV which is lower than the optimum bandgap. This led to the incorporation of gallium in the ternary CIS semiconductor resulting in the formation of the pseudo-quaternary $CuIn_{1-x}Ga_xSe_2$ (CIGS) semiconductor. The incorporation of gallium is done in such a way that it is used to substitute an equivalent amount of indium. This substitution raises the bandgap of the material. The bandgap can be varied from 1.02 eV (CIS bandgap) to 1.7 eV (CGS bandgap). Figure 1.5 shows the variation of bandgap with gallium content varied over a full composition range [35]. The bandgap variation for $CuIn_{1-x}Ga_xSe_2$ is given by [36];

$$E_g = 1.011 + 0.664x - 0.249x(1-x) \quad \text{[Stochiometric CIGS]} \tag{1.1}$$

$$E_g = 1.0032 + 0.71369x \quad \text{[Cu poor CIGS]} \tag{1.2}$$

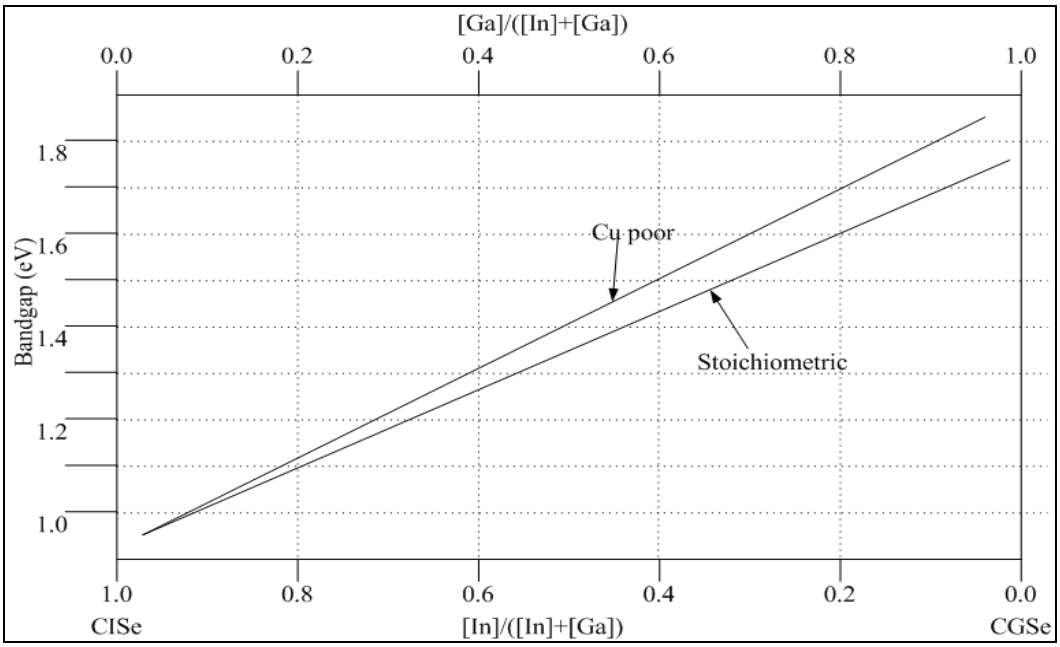


Figure 1.6: Bandgap Variation as Function of Gallium Content

Another advantage of gallium incorporation in CIS films is better adhesion of the absorber film to the molybdenum back contact. Also gallium incorporation can cause a graded bandgap which leads to better collection of charge carriers. Gallium has the tendency to segregate to the back of the device that causes abrupt changes in the carrier concentration near the back contact. Indium and copper have higher reactivity with selenium as compared to gallium. Hence, indium and copper diffuse to the surface during selenization process. After complete consumption of indium into $CuInSe_2$ and some $CuSe_2$ at the surface, selenization of gallium and its interaction with $CuSe_2$ begins towards the back contact forming a higher bandgap $CuGaSe_2$ towards the back contact. This leads to an electric field that acts as minority carrier mirror and reflects all the minority charge carriers. This electric field is called a back surface field (BSF). BSF also prevents recombination of electron-hole pairs at the back contact.

The best device efficiencies for CIGS thin film solar cells have been achieved on devices with bandgap around 1.1 eV. It has been observed that device efficiencies tend to decline as the bandgap increases above 1.3 eV and the gallium content, x increases beyond 0.5 due to reducing fill factors and short circuit current density [37]. Another feature of addition of gallium to the $CuInSe_2$ matrix is a possibility of bandgap engineering. By controlled variation of gallium concentration over the depth of the absorber layer bandgap grading can be achieved.

Figure 1.6 depicts two different structures, one with a single bandgap throughout the absorber layer, and the other with a graded bandgap (the bandgap increasing towards the back). In CIGS, the bandgap increase arising because of Ga incorporation, seems to be accommodated by the conduction band minimum moving to higher energies [38]. If a single bandgap exists throughout the thickness of the absorber layer, then the band bending is confined to the front portion of the layer, in the region where the depletion region penetrates. (This, of course, depends on the doping level in the film.) Hence, there is no electric field outside this region, towards the back of the device. Therefore, the minority carriers (electrons in the conduction band) that are generated outside the depletion region must rely on the diffusion mechanism to reach the junction. However, if the minority carrier diffusion length is small, compared to the depth of the absorber layer beyond the depletion region, then carriers generated far away from the depletion region (i.e., towards the back of the layer) have only a small probability of being collected by the junction, and of contributing to the photocurrent. In the other structure, a bandgap grading and the resulting conduction band edge bending exist. In this case, the electric field helps the electrons move towards the junction, thereby increasing the probability of their collection [39].

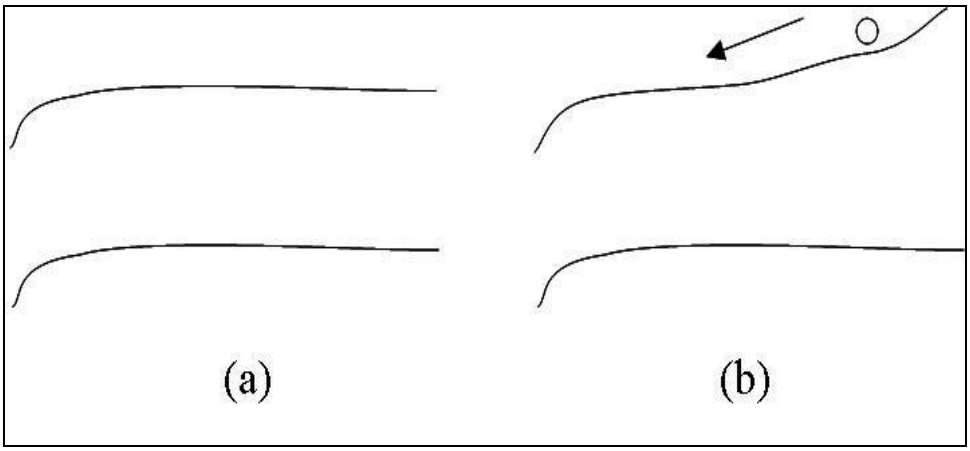


Figure 1.7: Band Bending with (a) No Grading (b) Grading

Also the formation energy for a $Ga_{Cu}$ defect is higher than the formation energy of $In_{Cu}$. This destabilizes the formation of defect pairs of $2V_{Cu}+In_{Cu}$ thereby reducing the tendency for the formation of ODC and enhancing the α-CIGS region. The highest reported efficiency for a small area CIGS solar cell is 20.3 % by ZSW [40].

## 1.5 CIGSeS Thin Film Solar Cells

As mentioned earlier, gallium has tendency to segregate to the back near the Mo interface. This leads to a favorable bandgap grading as it creates a BSF thus reducing recombination of electrons at the back contact. However, in case of two step processing of CIGS thin film solar cells, it is not possible to have gallium near the junction or the space charge region. In a two step process the metallic precursors are deposited either by sputtering or evaporation in the first step. In the second step these metallic precursors are annealed in selenium ambient, known as selenization, to form CIGS absorber layer. Hence, the whole purpose of adding gallium to the CIS matrix for achieving increase in voltages is not served for CIGS solar cell prepared by the two step process.

Extensive research has been carried out on $CuInGaS_2$ (CIGS2) thin film solar cells. CIGS2 absorber layers have a bandgap of ~1.5 eV. As the bandgap of this absorber is more than that of CIGS absorber layer a bandgap grading can be achieved by combining these two absorber materials. For this reason, addition of sulfur to the CIGS matrix is considered to achieve higher voltages that are necessary for high efficiency copper based chalcogenized modules. The bandgap variation for $CuIn_{1-x}Ga_x(Se_{1-y}S_y)_2$ is given by [41];

$$E_g(eV) = 1 + 0.13x^2 + 0.08x^2y + 0.13xy + 0.55x + 0.54y$$

Figure 1.8 [33] shows the graded bandgap that can be achieved in $CuIn_{1-x}Ga_xSe_{2-y}S_{2y}$ (CIGSeS) thin film absorbers by addition of gallium and sulfur to the CIS matrix. As can be seen in the figure addition of sulfur tends to move the valence band maximum to lower energies leading to a higher bandgap in the space charge region and so higher voltages. This becomes an added advantage in comparison to increase in bandgap by moving of the conduction band minimum to higher energy as lowering of the valence band maximum to lower energies results in an electric field that opposes the movement of holes towards the junction.

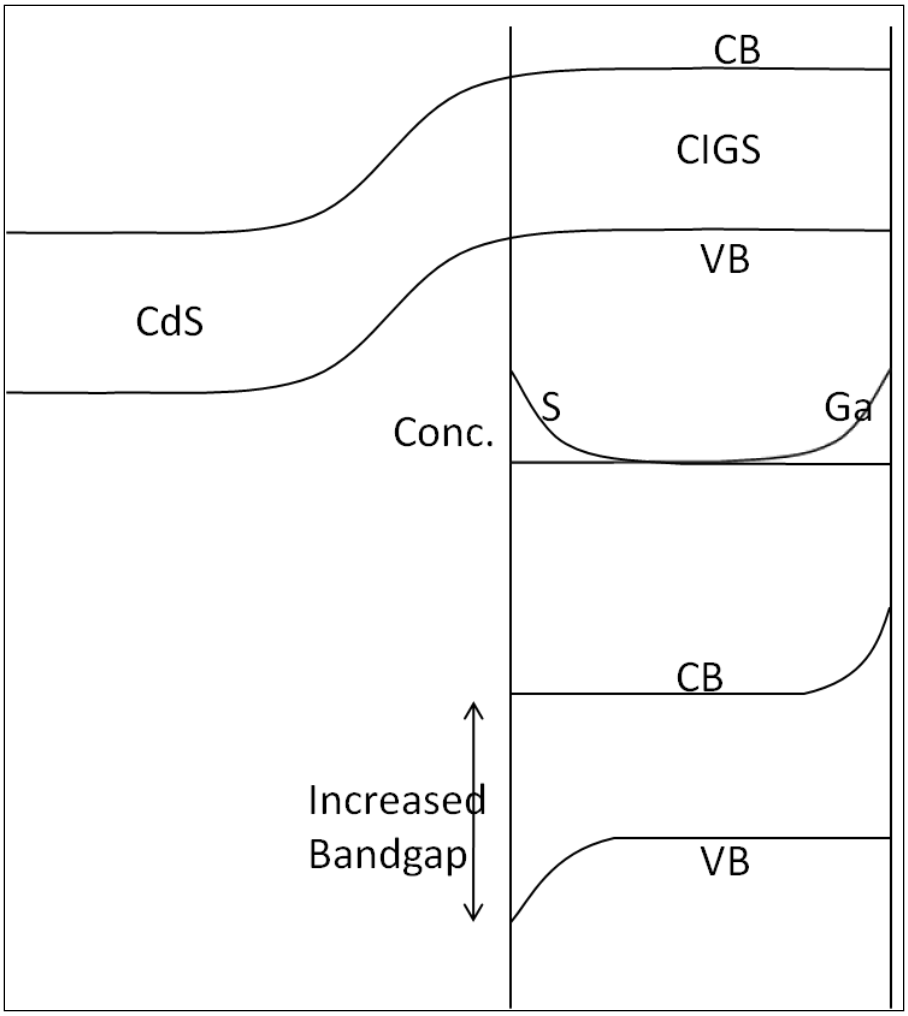


Figure 1.8: Bandgap Engineering by Addition of gallium and Sulfur

CIGS thin film absorber layer can be converted to CIGSeS absorber by annealing the CIGS absorber layer in sulfur ambient. This process is known as sulfurization. On sulfurization the sulfur atoms may occupy selenium vacancies or replace selenium. Replacement of selenium is possible due to the higher reactivity of sulfur compared to selenium. This leads to reduction in the number of compensating donors and moreover, it leads to passivation of the surfaces and interfaces [42].

## 1.6 Role of Sodium

Sodalime glass (SLG) is the most commonly used substrate in fabrication of CIGS thin film solar cells. SLG is known to contain significant amount of sodium in the form of $Na_2O$. Sodium tends to diffuse into the absorber film when CIGS films are deposited at high temperatures, which is the case in most of the efficient CIGS thin film solar cells. It has been shown that diffusion of small amounts of sodium in the CIGS absorber film tends to have a favorable effect on the film and device properties. One of the favorable alterations includes increase in p-type conductivity [43]. It has been reported that sodium promotes increase in grain size and preferential orientation [44] and a reduced sensitivity of devices to the metal ratio.

Several models that have been devised to elucidate the effect of sodium are as follows;

1. Occupation of copper site in the lattice by sodium reduces the number of ($Cu_{In}$-$In_{Cu}$) defect pair. This reduces the cation disorder and improves the fill factors and the voltages.
2. Sodium passivates the surface and the grain boundaries due to improved incorporation of oxygen [45].
3. Sodium ions diffuse to the absorber surface along the grain boundaries and subsequently react with selenium to form sodium polyselenide ($Na_2Se_x$) compound where x = 1-6, $\neq$ 5. $Na_2Se_x$ compounds act as a Se source during the absorber growth. $Na_2Se_x$ compounds retard the growth of the CIGS phase and thus aid in improved incorporation of selenium into the absorber film. If the partial pressure of the selenium is low then $Na_2Se$, a very stable compound is formed. The release of selenium from $Na_2Se$ is unlikely thus leading to poor

absorber growth [46]. $NaInSe_2$ forms during absorber preparation, this directs the CuInSe2 film to the (112) preferred orientation [47].

The "standard" method to incorporate Na into CIGS absorber layers is to use a sodalime glass substrate without an alkali barrier layer between the substrate and the Mo back contact layer, where the Na diffuses into the absorber during growth. World-record efficiency cells have been fabricated by using this technique. The typical sodium concentrations found in such CIGS layers are of the order of 0.1 at% [48]. Sodium diffusion from the SLG is a passive sodium incorporation technique that depends on the properties of the SLG and also the properties of the Mo back contact. The diffusion of sodium by the passive incorporation technique is non-uniform and also is not well-controlled.

The non-uniform out diffusion of sodium from the SLG substrate can be avoided by using an alkali barrier. The typical diffusion barriers employed are $Si_3N_4$ [49], $SiO_2$, $Al_2O_3$ [50] etc. Na containing precursor film is usually deposited prior to the precursor deposition on the Mo back contact layer. Na containing compounds used are NaF [51], $Na_2Se$ [52], $Na_2S$ or $Na_xO$ [53].

Sodium has also been incorporated into the film after the precursor deposition but before the selenization/sulfurization process. However, this method of sodium incorporation adds another step in the process and may not be suitable for large volume production.

## 1.7 Interfacial Layer between Mo and Absorber Layer

A thin interfacial layer is formed at the molybdenum and absorber interface during absorber preparation. The interfacial layer can be $MoSe_2$ and $Mo(Se_{1-x}S_x)_2$ depending on the process. Both the compounds have hexagonal lattice structure. The lattice constants of $MoSe_2$ are $a_0 = 3.288\pm0.002$ Å and $c_0 = 12.92\pm0.01$ Å. The $MoSe_2$ layer is formed at temperatures >350 ºC

[54]. The material is stable between 0 ºC – 1200 ºC and at 67 at.% selenium. The heat of formation of $MoSe_2$ is -242.2± 3.3 kJ/mol at 298.15 °K and p = 101.325 kPa [55]. The bandgap of $MoSe_2$ is 1.3 – 1.4 eV and is inherently highly p-type in nature.

The formation of this layer depends on several parameters. Studies have shown that the formation of the interfacial layer affects the performance of the solar cell. The Mo/CIGS contact, without the $MoSe_2$ layer formation, results in a Schottky type of contact that causes recombination losses at the back contact. Formation of a thin $MoSe_2$ layer is essential to facilitate a quasi-ohmic electrical contact across the CIGS–Mo interface. This quasi-ohmic contact results in reduced recombination losses and thus improves cell efficiency [56]. The $MoSe_2$ layer also improves the adhesion of the absorber layer to the molybdenum back contact [57].

The thickness and crystallographic orientation of the $MoSe_2$ layer determine the adhesion and electrical properties of the CIGS–Mo interface. The conductivity of $MoSe_2$ layer is anisotropic hence the orientation of the layer can have a direct effect on the transport properties at the interface. Conductivity through the parallel $MoSe_2$ layer is about two times higher than the $MoSe_2$ layers oriented perpendicular to the molybdenum substrate [58].

# CHAPTER 2 PHYSICS OF SEMICONDUCTOR AND SOLAR CELL

One of the simplest forms of a solar cell is a p-n junction with incident light as the external source of excitation for producing excess charge carriers. Thus it is essential to comprehend the semiconductor fundamentals in order to understand the principle and operation of solar cells.

## 2.1 Energy Levels of Isolated Atoms

An electron of an isolated atom can have discrete energy levels as given by the following approximation;

$$E_n = \frac{-Z^2 m_0 q^4}{8\varepsilon_0^2 h^2 n^2} \tag{2.1}$$

Where,

q- Electron charge;

Z- Atomic Number;

$m_0$- Mass of free electron;

$\varepsilon_0$- Permittivity of free space;

h- Plank's constant;

n- Principal quantum number

When two such identical atoms are brought in close proximity the energy level for the electron will be split into two levels by the interaction between the two atoms. Now let us consider a solid where there are N atoms very closely packed. The outer orbits of each atom then overlap and interact with each other. This results in shifting of the energy levels and N separate narrowly spaced energy levels are formed and for larger values of N which is generally the case

in solids it results in a continuous band of energy. Figure 2.1 illustrates the formation of energy bands in solids.

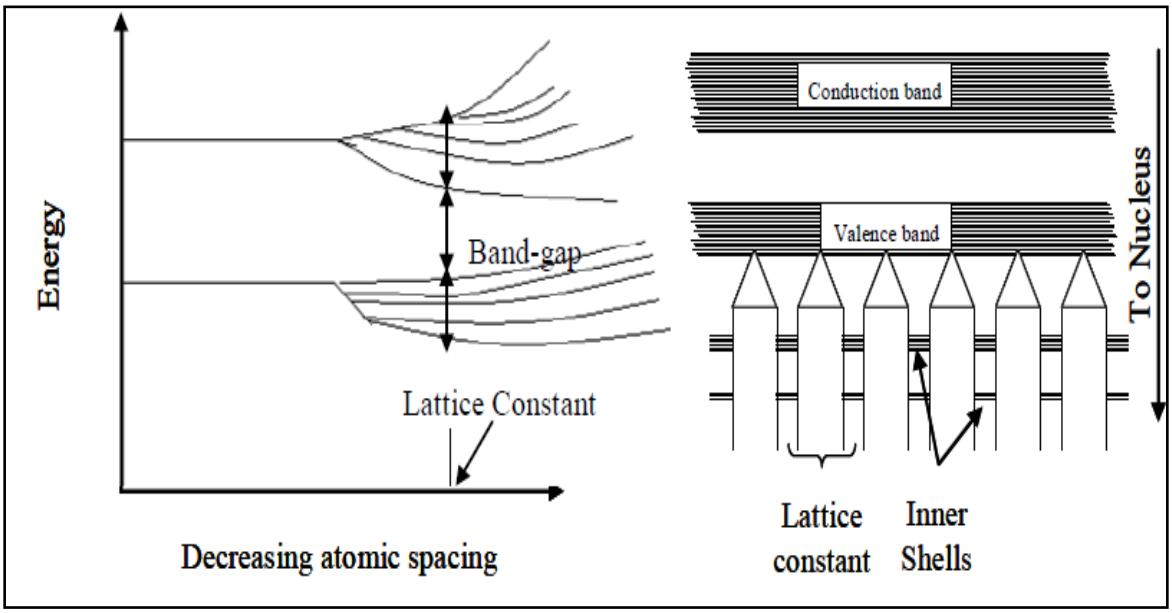


Figure 2.1: Formation of Energy Bands from Discrete Energy levels

## 2.2 What is a Semiconductor

Materials can be classified as metals, insulators or semiconductors. In metals the conduction band overlaps with the valence band (figure 2.1) so that there is no bandgap. As a result the electrons can move the net higher available energy level with only a small applied field. Hence, metals exhibit high conductivity. In insulators the valence electrons form a strong bond between neighboring atoms that is difficult to break. Due to this there are no free electrons available for current conduction at room temperature. In insulators the valence band is completely filled and the conduction band is completely empty with a large bandgap as shown in figure 2.1 resulting in poor conductivity. In semiconductors, at T = 0 °K the valence band is completely filled. However, the forbidden energy bandgap is not very large (figure 2.1). Hence at room temperature the loosely bound electrons are provided enough energy to break the bond and

hop from the valence band to the conduction band. As the conduction band has many empty energy states the electrons can move even with a small electric field. Thus, semiconductor conductivity lies somewhere in between those of metals and insulators.

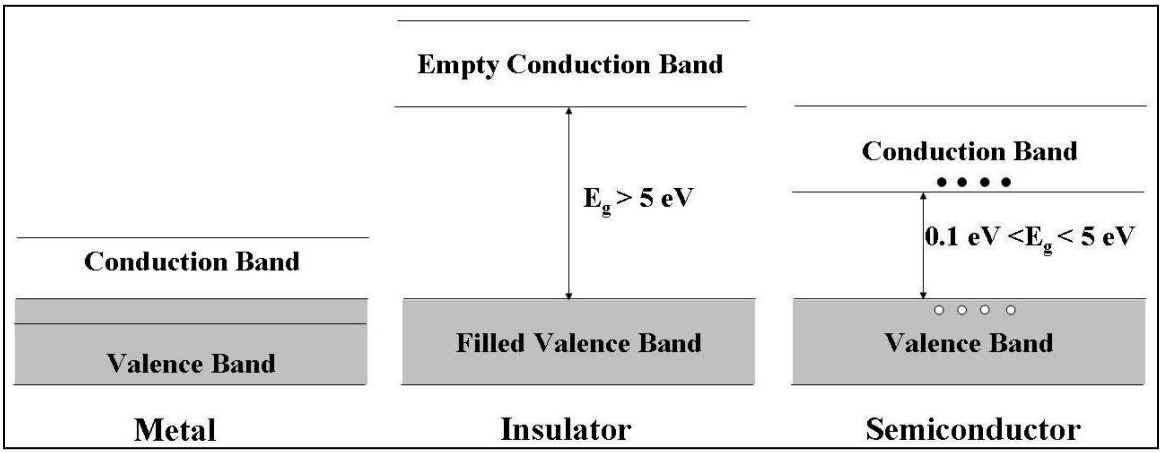


Figure 2.2: Energy Band Diagram for Metal, Insulator and Semiconductor

A semiconductor can be classified as intrinsic or extrinsic. An intrinsic semiconductor is extremely pure with a very low concentration of impurities. When an intrinsic semiconductor is doped with impurities it is known as an extrinsic semiconductor. An extrinsic semiconductor can be classified as n-type and p-type. An extrinsic semiconductor doped with donor impurities that provide an extra electron is known as n-type material and one doped with acceptor impurities that accept electron and provide an extra hole is known as p-type material.

In any semiconductor there is a forbidden energy region in which allowed states cannot exist. The energy band above this energy gap is called the conduction band and the one below is called the valence band. And the forbidden energy region is called the Energy Bandgap (Eg) which is one of the most important parameters in semiconductors. Physically, Eg is essentially the energy required to break a bond and free an electron into the conduction band and leave a hole in the valence band.

The Fermi level is defined as the energy level below which all states will have at most two electrons of opposite spin according to Pauli's exclusion principle [59]. It can be also defined as the energy level where the probability of finding an electron is ½. The occupation of the conduction and the valence band states is governed by the Fermi-Dirac statics and is given by

$$f(E) = \frac{1}{1 + e^{(E - E_F)/kT}} \tag{2.2}$$

Where,

k - Boltzman's constant;

T - Absolute temperature;

$E_F$ - Fermi energy.

Essentially, it defines the probability of electron presence in the conduction band and 1- F(E) gives the probability of hole being present in the valence band. If the Fermi energy level is not very close to either of the band edges i.e. $E_c$-$E_f$ » kT or $E_f$-$E_v$ » kT then for all practical purposes the Fermi Dirac statistics can be replaced by the Boltzman factor;

$$\exp(-\frac{E - E_f}{kT}) \qquad \text{and} \qquad \exp(-\frac{E_f - E}{kT}) \tag{2.3}$$

for electrons in the conduction band and holes in the valence band respectively.

For an intrinsic semiconductor the Fermi level lies approximately in the middle of the bandgap. This Fermi level shifts towards the conduction band for n-type and towards the valence band for p-type semiconductors. The Fermi levels can be calculated using the following equations [59];

For n-type $E_F - E_C = kT.\ln(N_D / N_C)$ (2.4)

For p-type $E_V - E_F = kT.\ln(N_A / N_V)$ (2.5)

where $E_C$ - conduction band minimum;

$E_V$ - valence band maximum;

$N_D$ - Donor concentration;

$N_A$ – Acceptor concentration;

$N_C$ and $N_V$ are the effective density of state in the conduction band and valence band respectively and are given by;

$$N_C = 2(\frac{2\pi m_e^* kT}{h^2})^{3/2} \quad \text{and} \quad N_V = 2(\frac{2\pi m_h^* kT}{h^2})^{3/2} \tag{2.6}$$

## 2.3 p-n Junction

When two isolated n-type and p-type material are electrically connected they form a metallurgical p-n junction. When a p-n junction is formed, there exists a large carrier concentration gradient at the junction. This leads to diffusion of electrons from the n-side to the p-side and diffusion of holes from the p-side to the n-side. As the electrons continue to diffuse to the p-side some of the positive donor ions are left uncompensated on the n-side as they are fixed in the lattice. Similarly diffusion of hole to the n-side causes some of the negative acceptor ions to be left uncompensated on the p-side. This results in a negative space charge being formed near the p-side of the junction and a positive space charge being formed near the n-side of the junction as shown in figure 2.2. The space charge region creates an electric field that is directed from the positive charge to the negative, thus opposing the diffusion tendency of majority carriers. A potential buildup occurs across the junction due to the electric field. The electric field and the potential distribution are shown in figures 2.3 and 2.4 respectively.

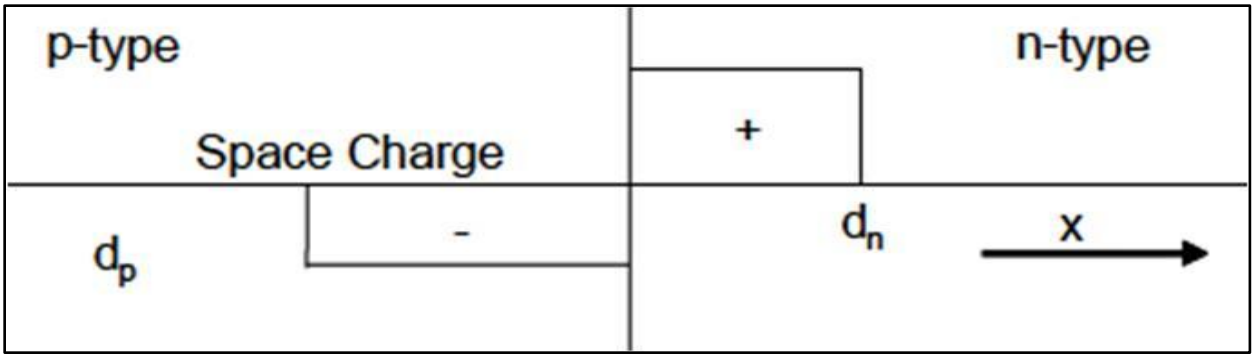


Figure 2.3: Space Charge Region

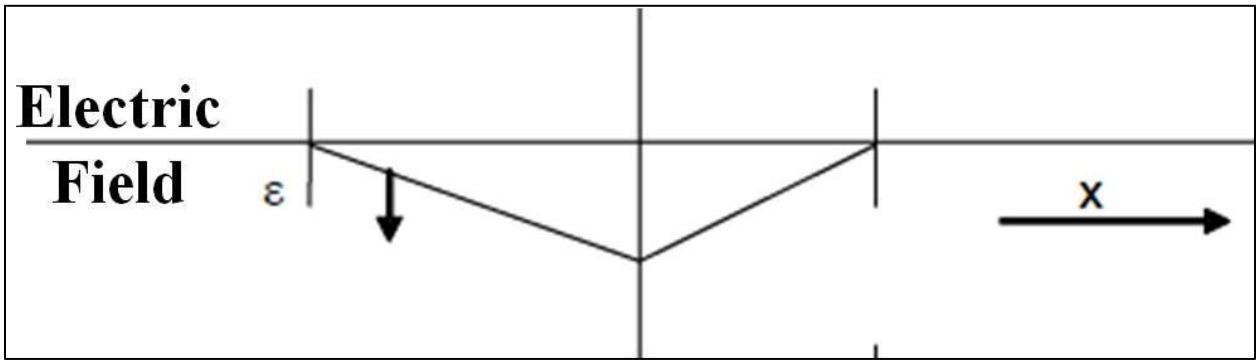


Figure 2.4: Electric Field Developed across the Junction

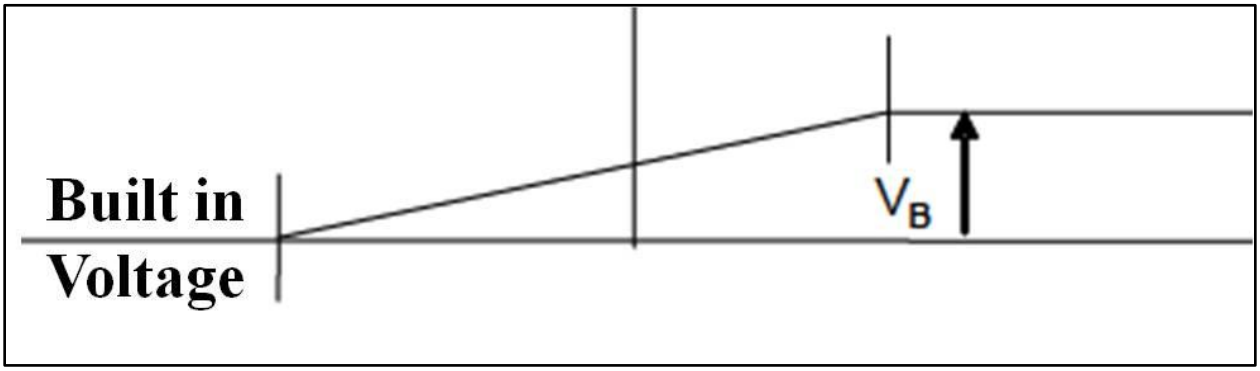


Figure 2.5: Potential Distribution across the Junction

Under thermal equilibrium the electron and hole current densities are given by;

$$J_n = \mu_n . n . \partial E_F / \partial x = 0 \quad (2.7)$$

$$J_p = \mu_p . p . \partial E_F / \partial x = 0 \quad (2.8)$$

where $\mu_n$ – Electron mobility;

$\mu_p$ - Hole mobility;

$E_F$ - Fermi energy;

n – Electron concentration;

p - Hole concentration.

For net zero electron and hole current densities it is essential that the Fermi level is constant through the sample. This result in the bending of the energy bands that leads to a potential being developed. The developed potential is known as the built in voltage ($V_B$). The band bending occurring in a p-n junction is shown in figure 2.5.

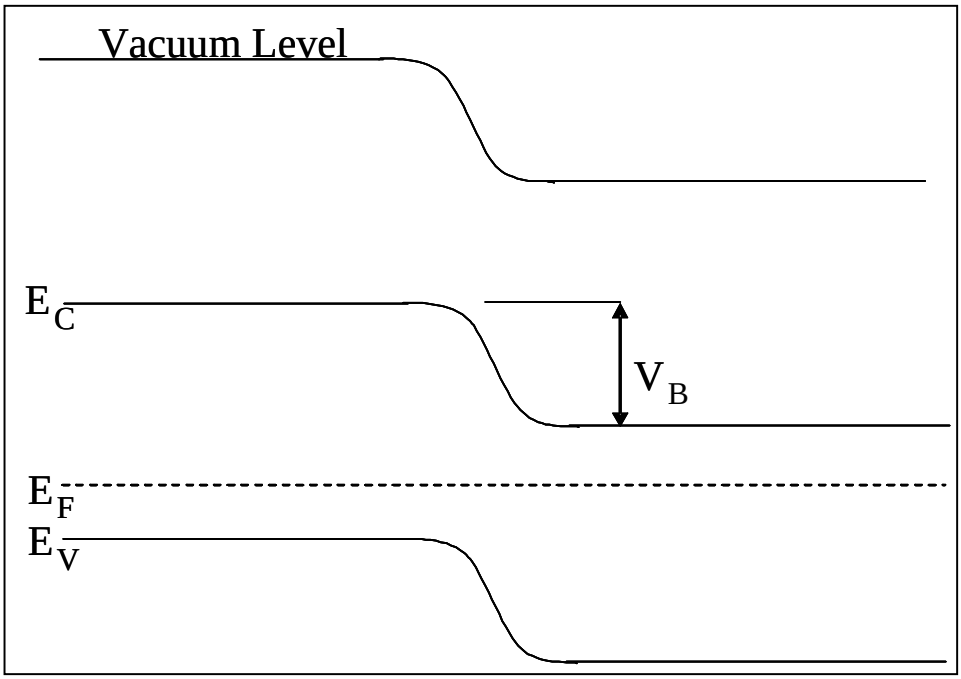


Figure 2.6: Band Bending in a p-n junction

The build in voltage is given by;

$$V_B = kT\ln(N_A.N_D / n_i^2) \tag{2.9}$$

where $N_A$ – Acceptor concentration;

$N_D$ - Donor concentration;

$n_i$ - intrinsic concentration.

Under equilibrium conditions the net electric field in the neutral region should be equal to zero. This means that the total charges on the n side are equal and opposite of the total charges on the p side. This leads to the charge neutrality equation given by [59];

$$N_A.x_p = N_D.x_n \tag{2.10}$$

where $x_p$ – Width of the depletion region on the p side of the junction;

$x_n$ - Width of the depletion region on the n side of the junction.

The total space charge width is given by [59];

$$W = \sqrt{\frac{2\varepsilon_s (N_A + N_D)(V_B - V)}{qN_A N_D}} \tag{2.11}$$

The space charge region and the corresponding electric field gives rise to a junction capacitance that is given by the following equation [59];

$$C = \sqrt{\frac{q\varepsilon_s N_A}{2(V_B - V)}} \qquad \text{for } N_A >> N_D \tag{2.12}$$

where q – electron charge;

$N_A$ – Acceptor concentration;

$N_D$ – Donor concentration;

$\varepsilon_s$ – Permittivity of the material;

$V_B$ – Applied bias voltage.

As can be seen from eq. 2.12 the graph of $1/C^2$ versus voltage will give a straight line. The slope of this line will provide the acceptor concentration and the intercept at y=0 will

provide the built in potential. In our research such capacitance-voltage measurements will be used to calculate the net carrier concentration and the built in potential.

## 2.4 Heterojunction

p-n junction can be classified into two types homojunction and heterojunction. Homojunction is a junction between two n-type and p-type of the same material e.g. silicon. Heterojunction is a junction between two dissimilar semiconductor materials. Heterojunctions are of two types; isotype and anisotype heterojunctions. Isotype heterojunctions are the one formed with materials of same conductivity and anisotype are formed with materials of different conductivities. Semiconductor properties such as electron affinity, work function and material properties such as lattice constant differ for each element. These differences result in band discontinuities at the interface that act as traps or recombination centers.

Figure 2.7 shows the band structure of two materials before formation of a junction. The two semiconductors have different bandgaps $E_{g1}$ and $E_{g2}$, different work functions $\Phi_{m1}$ and $\Phi_{m2}$, different electron affinities $\chi_1$ and $\chi_2$ and different permittivities $\varepsilon_1$ and $\varepsilon_2$. Figure 2.8 shows the energy band diagram of a heterojunction. The band discontinuities are given by;

$$\Delta E_C = \chi_1 - \chi_2 \tag{2.13}$$

$$\Delta E_V = E_{g1} - E_{g2} - \Delta E_C \tag{2.14}$$

The total built in potential $V_d$ is sum of electrostatic potentials $V_{d1}$ and $V_{d2}$ of the two semiconductors. In homojunction solar cells, minority charge carriers created by photons absorbed in the n-type region are lost due to recombination. Heterojunction solar cells have the advantage of using higher bandgap n-type heterojunction partner so that lesser number of charge

carriers are lost due to recombination. The thin film solar cells that are extensively researched are basically heterojunctions.

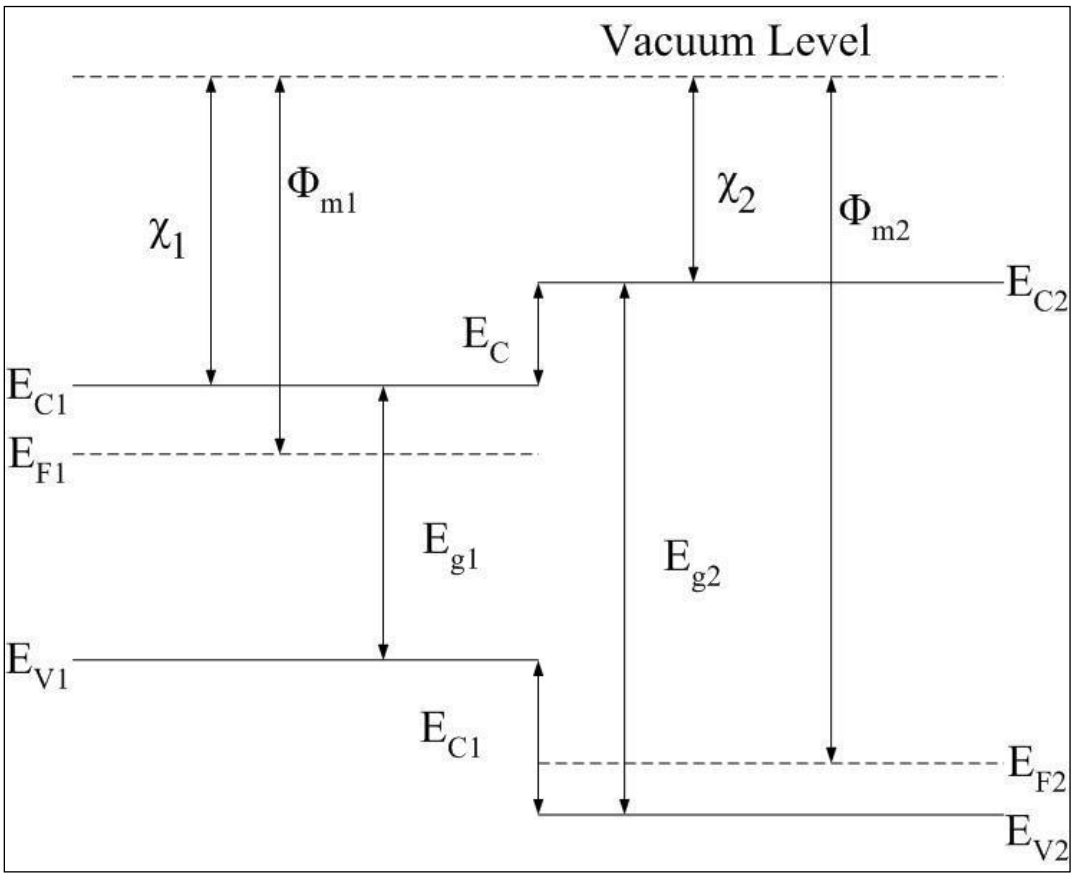


Figure 2.7: Energy Band Structure of Isolated Semiconductors

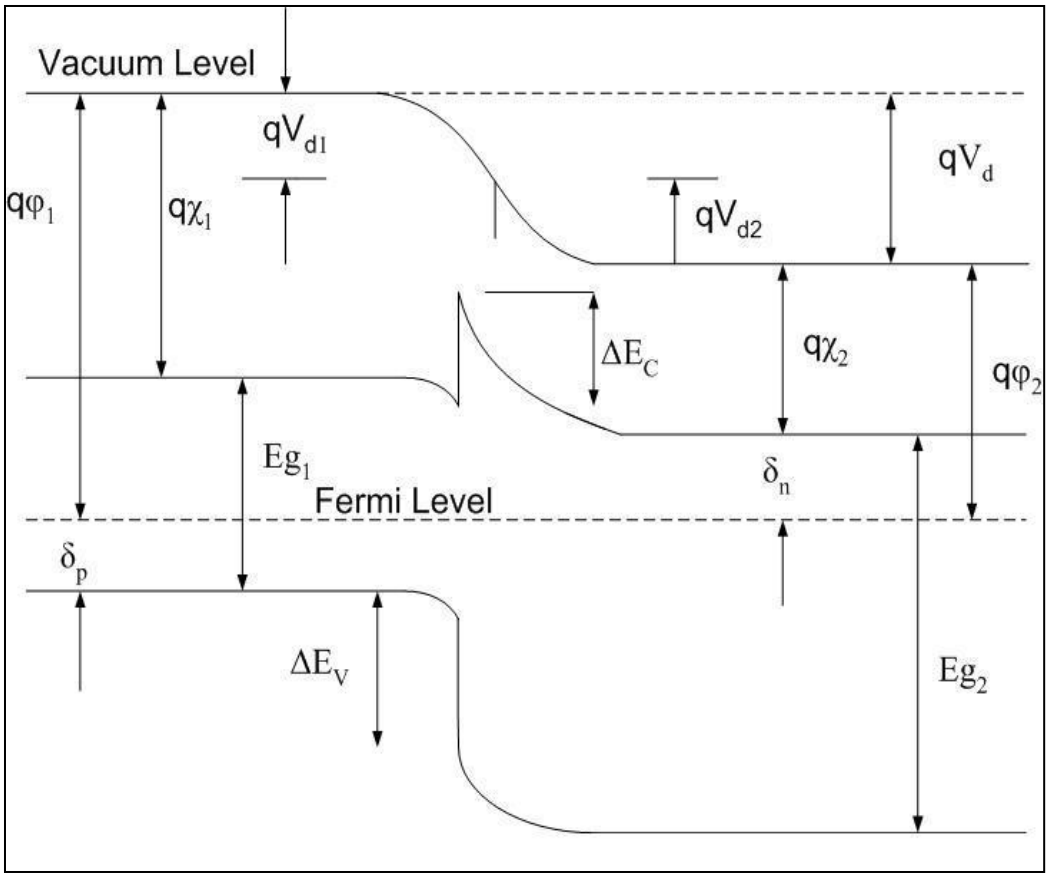


Figure 2.8: Energy Band Diagram of Heterojunction

## 2.5 Solar Cells

When a light is made incident on a semiconductor photons with energy greater than the bandgap of the semiconductor are absorbed in the semiconductor and photons with energy less than the bandgap are transmitted.

In a solar cell these absorbed photons create electron-hole pairs. The minority charge carriers generated within the diffusion length of the junction can easily diffuse to the junction and then are swept across the junction by drift. Once on the other side of the junction these charge carriers are majority charge carriers and hence are conducted to the contacts. This results in a photo generated current ($I_L$) to flow through the external circuit. The phenomenon of solar

energy conversion thus involves the processes of absorption of photons, generation of carriers, diffusion of the minority carriers to the junction, collection of the separated carriers at the external contacts, and finally the utilization of the power generated. If $L_p$ and $L_n$ are the minority carrier diffusion lengths of holes and electrons respectively, W is the depletion width and G is the generation rate of electron-hole pairs, then [60]

$$I_L = q.A.G.(L_n + L_p + W) \tag{2.15}$$

Depending upon the intended application, the diode can be operated either in the third or the fourth quadrants of the I-V characteristic. Power is delivered to the device from the external circuit when both the current and junction voltage are either positive or negative. If operated in the fourth quadrant, however, power is delivered from the junction to the external circuit, and this is the principle of operation of a solar cell device. As mentioned at the beginning of this chapter a solar cell is essentially a p-n junction diode. Hence in the dark condition a solar cell behaves like a diode following the diode equation given by [59];

$$I = I_O\left[e^{qV/kT} - 1\right] \tag{2.16}$$

where $I_O$ – Reverse saturation current;

V – Applied bias voltage.

Under illumination the photocurrent is generated and hence the net current flowing through the external circuit is the combination of the diode current and the photocurrent which is given by [59];

$$I = I_O\left[e^{qV/kT} - 1\right] - I_L \tag{2.17}$$

where $I_L$ – Photogenerated current.

The first term in eq. 2.17 gives the voltage driven current and the second term gives the light generated current. As can be seen from the above equation under short circuit conditions the voltage V is zero and so the first term in eq. 2.17 tends to zero. Hence the short circuit current is equal to the photo generated current. Thus,

$$I_{SC} = I_L \tag{2.18}$$

The open circuit voltage can be found out by setting the net current equal to zero and is given by [59];

$$V_{OC} = \frac{kT}{q}\ln\left[\frac{I_L}{I_0}+1\right] \approx \frac{kT}{q}\ln\left[\frac{I_L}{I_0}\right] \tag{2.19}$$

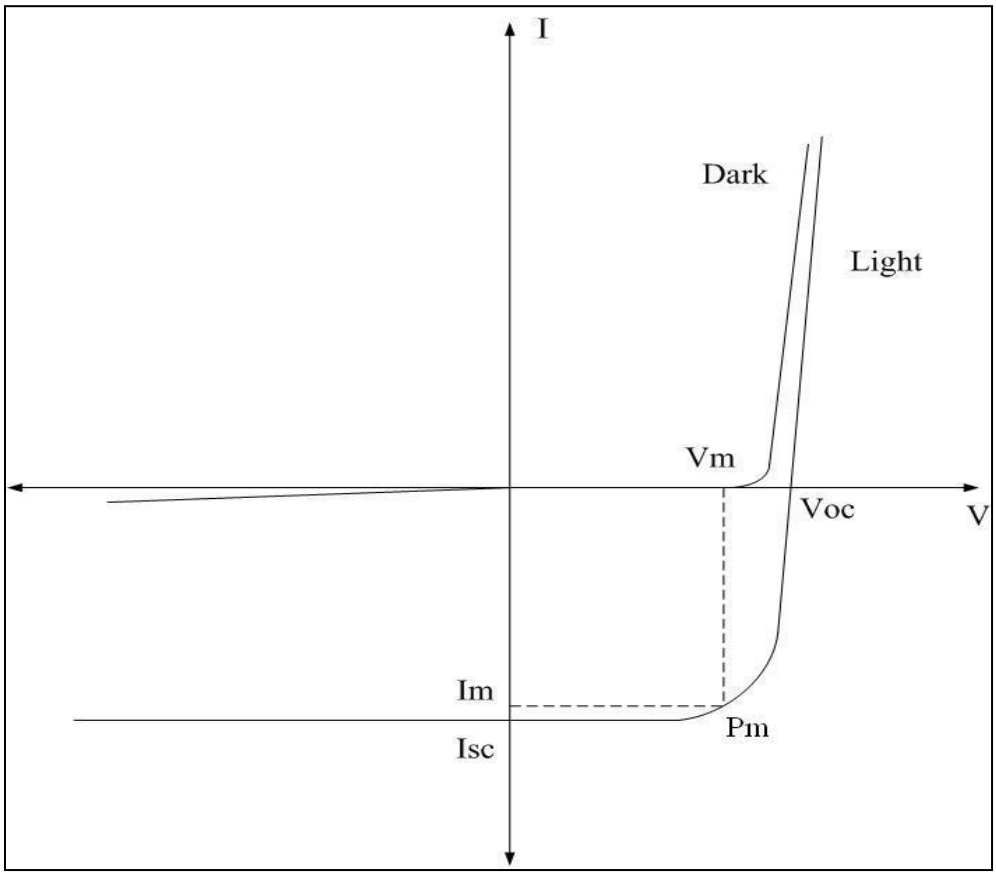


Figure 2.9: Ideal I-V Curve of Solar Cell under Light and Dark Conditions

Ideal current-voltage characteristics of solar cell under dark and illuminated conditions are shown in figure 2.9.

## 2.6 Equivalent Circuit of Solar Cell

Figure 2.10 a) shows the equivalent circuit of an ideal solar cell and 2.10 b) shows a real solar cell. A real solar cell has a series resistance $R_s$ and a shunt resistance $R_{sh}$. The current source in the circuit is the photogenerated current.

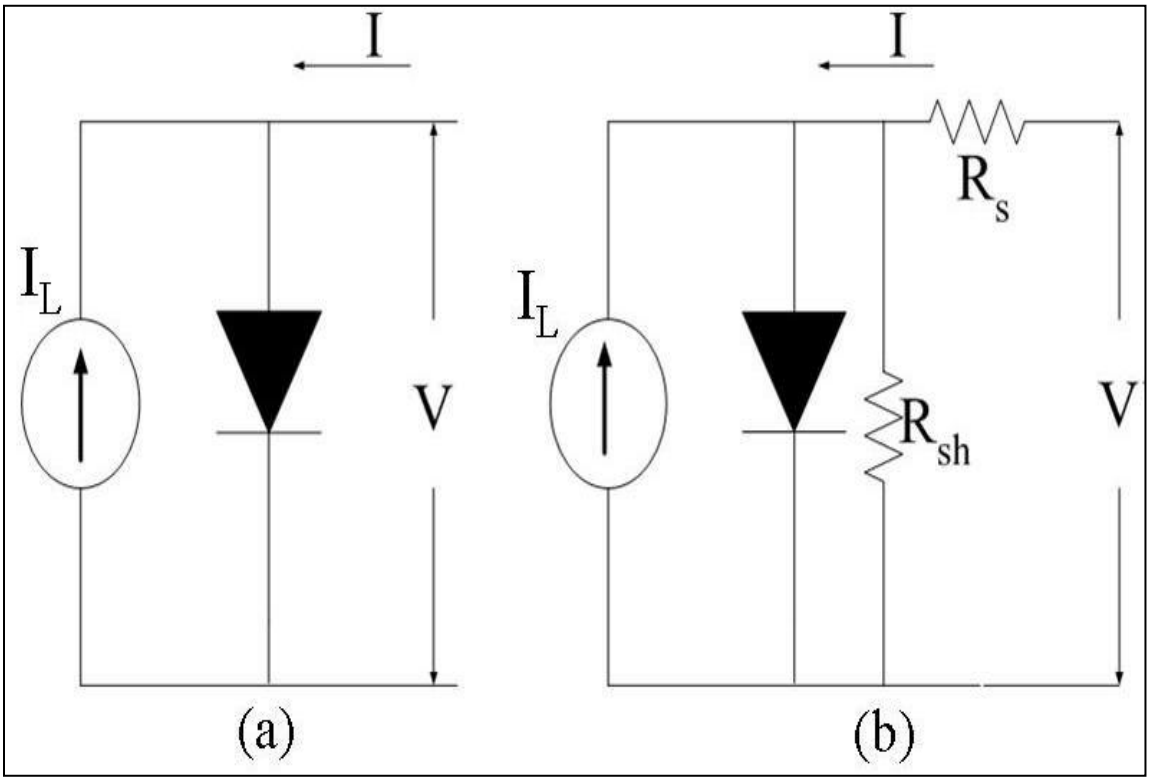


Figure 2.10: Equivalent Circuit of Solar Cell (a) Ideal; (b) With Series and Shunt Resistance

The series resistance $R_s$ is the combination of the bulk resistance of the absorber material, metallic contact resistance and the resistance between the contacts and the probe. The shunt resistance $R_{sh}$ takes into account the parallel current paths due to recombination in the absorber material and the value of $R_{sh}$ reduces as the number of shunt paths increase. As can be seen from

figure 2.10 the ideal values of $R_s$ and $R_{sh}$ are zero and infinity respectively. The effect of the series and shunt resistance on the ideal I-V curve of a solar cell is illustrated in figures 2.11 and 2.12 respectively. It can be seen from figure 2.11 that $R_s$ can be calculated by taking the reciprocal of the slope of the curve at the open circuit voltage point and $R_{sh}$ can be calculated by taking the reciprocal of slope of the curve at the short circuit current point.

The current equation given in eq. 2.17 does not take into account the effect of series and shunt resistance. The eq. 2.17 is modified to accommodate the effects of series and shunt resistance and is given by [59];

$$\ln\left[\left(I+\frac{I_L}{I_0}\right)-\frac{V-I.R_s}{I_0.R_{sh}}+1\right]=\frac{q(V-I.R_s)}{kT} \tag{2.20}$$

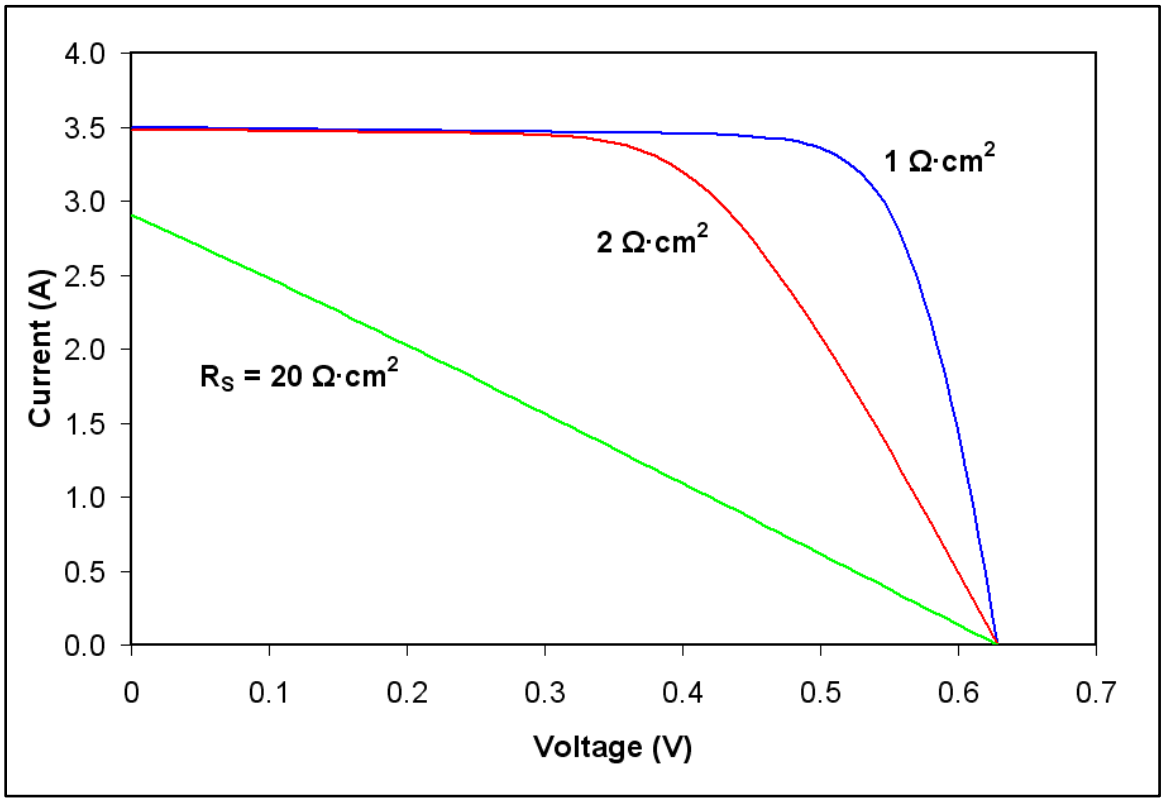


Figure 2.11: Effect of Series Resistance on I-V Curve

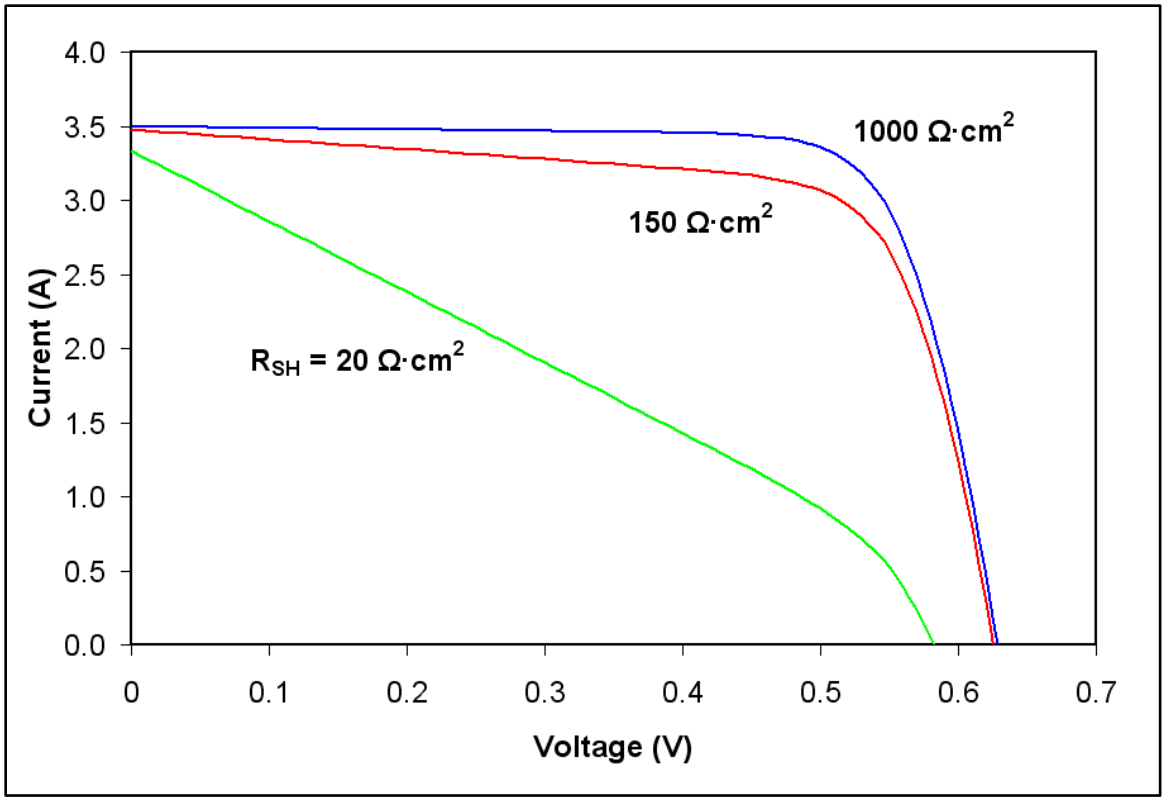


Figure 2.12: Effect of Shunt Resistance on I-V curve

Power cannot be delivered either at open circuit or short circuit conditions. As can be seen from the I-V curve in figure 2.9 the power delivered at any point can be calculated from the area under the rectangle in the fourth quadrant. The maximum power is delivered at point $P_m$ with optimum values of current $I_m$ and voltage $V_m$. This leads us to the definition of another important parameter known as the fill factor (FF). Fill factor can be defined as the squareness of the I-V curve at the maximum power point and is given by;

$$FF = \frac{V_m . I_m}{V_{oc} . I_{sc}} \tag{2.21}$$

where $V_m$ – Voltage at maximum power;

$I_m$ – Current at maximum power.

The conversion efficiency of solar cell is given by;

$$\eta = \frac{P_m}{P_{in}} = \frac{FF.V_{oc}.I_{sc}}{P_{in}} \tag{2.22}$$

where $P_{in}$ – Incident power.

Current-voltage measurements will be used in this research to calculate the PV parameters such as $V_{oc}$, $I_{sc}$, FF, η.

## 2.7 Spectral Response

The absorption of light in a semiconductor can be explained by considering the optical transmission equation given by;

$$\Gamma(\lambda) = \Gamma_0 \exp(-\alpha(\lambda)x) \tag{2.23}$$

where $\Gamma_0$ - Intensity of light incident on the semiconductor; α - Absorption coefficient which is a function of wavelength; *x* - Depth of material from surface of incidence.

The value of the absorption coefficient must be high for the absorber material used in a solar cell device, so that most of the light is absorbed in a useful way. Figure 2.12 shows the optical absorption coefficient spectral dependence for various semiconductors used in PV applications [61]. The figure clearly shows that CIS has the highest absorption coefficient of all semiconductors used for PV application.

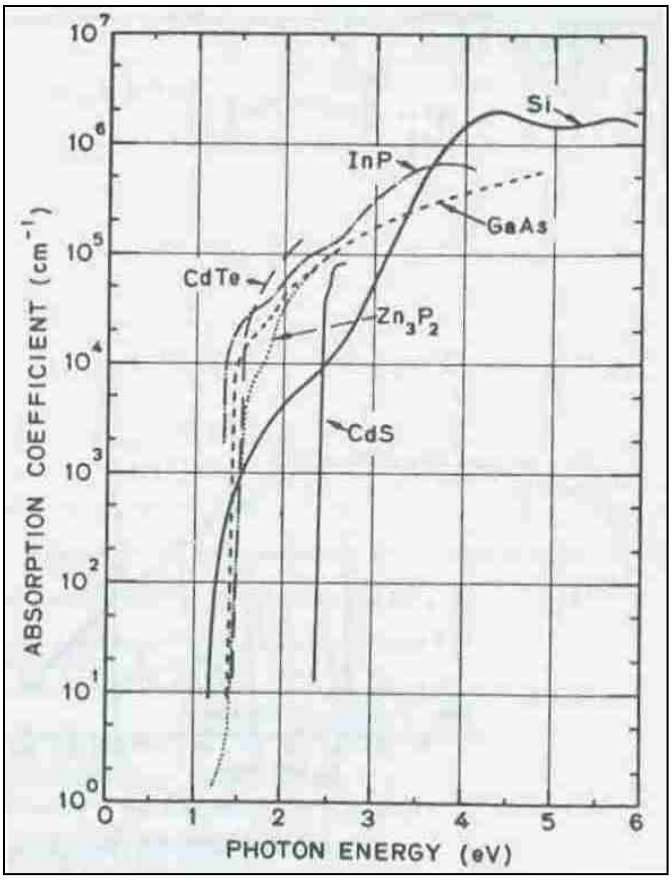


Figure 2.13: Optical Absorption Coefficient Spectral Dependence for Various Semiconductors

As mentioned earlier photons with energies greater than the bandgap of the semiconductor are absorbed in the semiconductor at some depth. These absorbed photons create electron-hole pairs at a depth of x from the surface. The generation rate of the charge carriers is given by [59];

$$G(\lambda, x) = \alpha(\lambda).F(\lambda).[1 - R(\lambda)]\exp[-\alpha(\lambda)x] \tag{2.24}$$

where F(λ) - Number of incident photons per $cm^2$ per unit bandwidth;

R(λ) - Fraction of these photons reflected from the surface.

Assuming low injection condition the internal spectral response can be derived as;

$$SR(\lambda) = \frac{1}{q.F(\lambda).[1-R(\lambda)]}\left[J_p(\lambda) + J_n(\lambda) + J_{dr}(\lambda)\right] \quad (2.25)$$

where $J_p(\lambda)$ - Photocurrent contributions from the p-region;

$J_n(\lambda)$ - Photocurrent contributions from the n-region;

$J_{dr}(\lambda)$ - Photocurrent contributions from the depletion region.

From eq. 2.25 the total photo generated current can be easily calculated and is given by;

$$J_L = \int_0^{\lambda_m} F(\lambda).[1-R(\lambda)].SR(\lambda)d\lambda \quad (2.26)$$

It is assumed that most of the charge carriers generated at the front of the solar cell (in case of CIGS thin film solar cells this is in the CdS layer) are lost due to recombination. Hence $J_n(\lambda)$ component in eq. 2.25 is negligible and can be neglected while calculating the total photogenerated current.

Quantum efficiency measurements can be used to calculate the bandgap of the absorber material. Moreover, information on which regions of the solar cell lead to current loss can be obtained.

# CHAPTER 3 DEVICE STRUCTURE AND FABRICATION OF SOLAR CELLS

## 3.1 Device Structure

The thin film solar cell used for this research has the structure sodalime glass/Mo/CIGSeS/CdS/i-ZnO/ZnO:Al. The fabrication of this solar cell begins with either molybdenum coated 2 mm thick sodalime glass or an ordinary 2 mm thick sodalime glass. A thin layer of NaF is deposited followed by the deposition of the absorber layer of CIGSeS layer. On top of this absorber layer a n-type heterojunction partner of CdS is deposited. A transparent and conducting window bilayer of i-ZnO/ZnO:Al is deposited on the top and the cells are completed by deposition of Cr/Ag contact fingers through a metallic mask. Figure 3.1 shows the device structure of the CIGSeS thin film solar cell fabricated in the FSEC Thin Film Photovoltaics Lab.

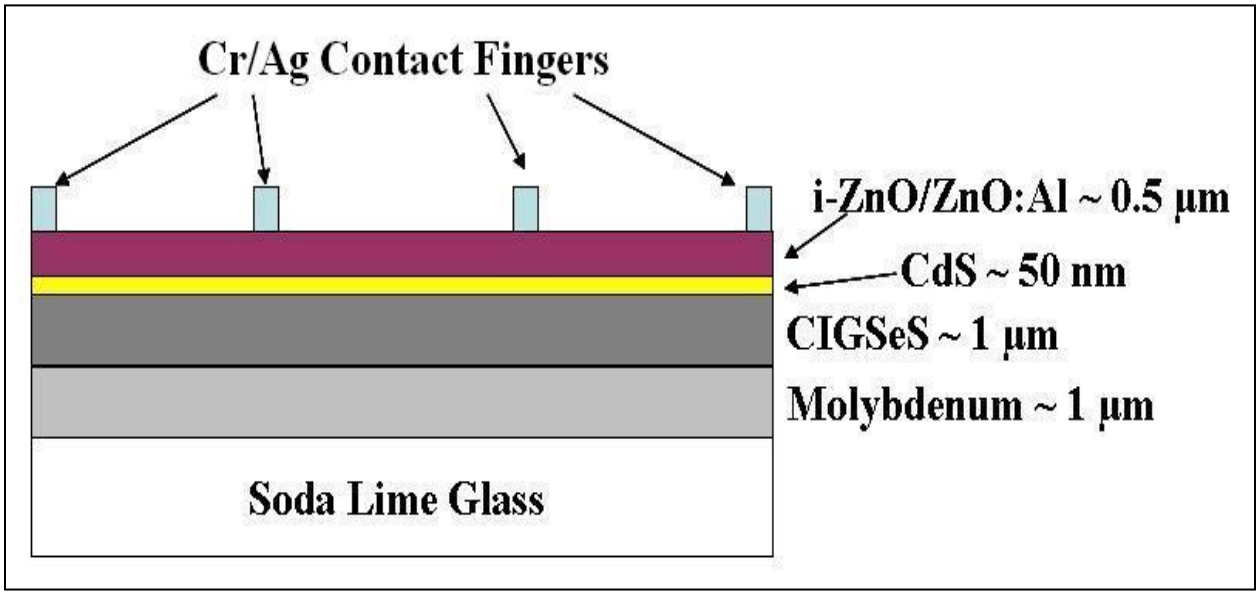


Figure 3.1: Device Structure of CIGSeS Thin Film Solar Cell Fabricated in FSEC Thin Film PV Lab

### *3.1.1 Substrate*

The substrate used in this research is sodalime glass (SLG) because of the main reason that it is cheap and easily available. Glass is corrosion resistant and another reason that SLG is used is diffusion of sodium from the glass seems to improve the cell performance. It improves the fill factors and the Voc. But this incorporation of sodium adds an uncontrollable factor in determining the reproducibility of the cell performance. The other issue with the sodalime glass substrates is that, at high temperatures glass softens and finally warps.

### *3.1.2 Molybdenum Back Contact*

The most widely used back contact in CIGS solar cells is molybdenum. Molybdenum forms a good Ohmic contact and offers high resistance to selenium corrosion. Several metals such as W, Mo, Ta, Nb, Cr, V, Ti and Mn were investigated as possible back contact material for CIGS solar cells. It was found that Ti, Cr, V, and Mn were found to react with selenium during absorber growth. Ta and Nb showed decent performance with only graded bandgap absorbers. It was found that W and Mo gave comparable performance [62]. Mo has become the back contact layer of choice because of its relative stability at the processing temperatures, resistance to alloying with Cu and indium, and its low contact resistance [63]. A relation between the current loss and back contact properties has been established and is given by [64];

$$J_{loss} = q\int f_{1.5}(\lambda).A_{BC}.d\lambda \tag{3.1}$$

where $A_{BC}$ - Optical absorbance of the back contact in the solar cell.

This can be calculated from energy flux balance into and out of this layer. f1.5(λ) is the spectral photon flux density of AM1.5 spectral intensity distribution. $J_{loss}$ is dependent on the

thickness of the absorber layer. For a thick absorber $J_{loss}$ is zero. But as the thickness starts to reduce $J_{loss}$ begins to increase depending on the reflective property of the metal.

The thickness of the Mo layer is around 1 micron. It is deposited using DC magnetron sputtering. The sputtering pressures determine the resistivity and adhesion of the films. It was found that Mo films deposited at higher pressures showed higher resistivity but better adhesion where as films deposited at lower pressures had lower resistivity but poor adhesion. Films deposited at high pressures have poor resistivity due to a rougher surface which results in the growth of rougher absorber layers. However, they adhere to the glass much better. Films deposited at lower pressures have a smoother surface which results in lower resistivity but they suffer from adhesion problem due to compressive stresses.

Recent studies have shown that there is a correlation of sodium diffusion into the absorber and the sputtering parameters of Mo back contact layer. It was shown that the sodium content in the absorber layer was low when Mo was deposited at low sputtering pressures as compared to when deposited at higher sputtering pressures [66].

The absorber layer was discussed in detail in the earlier chapter, therefore, the discussion will continue with with cadmium sulfide (CdS), the heterojunction partner.

### *3.1.3 Cadmium Sulfide Heterojunction Partner*

CdS is the commonly used n-type semiconductor as a heterojunction partner to p-type CIGS absorber layer to form p-n junction. CdS is a direct bandgap semiconductor with a bandgap of ~2.4 eV. CdS grown by chemical bath deposition (CBD) has a wurtzite structure with the c-axis perpendicular to the substrate plane and the crystal structure can be varied depending upon the deposition parameters [67]. The wurtzite structure of CdS is shown in figure

3.2. A recent study based on cross section images of the $CuInSe_2$/CdS interface has shown that CdS can grow epitaxially on $CuInSe_2$ [68]. The difference between the lattice constant of CdS and that of CIGS is very small. Hence, the interface of CdS and CIGS has a lower defect density.

CdS can be deposited using different processing techniques such as CBD, closed space sublimation (CSS), and RF sputtering. CBD is the most widely used technique for CdS deposition as the films grown by CBD are much more uniform and smoother as compared to the other techniques. CBD growth of CdS provides several advantages such as conformal growth and consequent protection against damage due to high energy ZnO deposition process. It provides a natural etching and cleaning of the absorber surface thus passivating the surface. Moreover, Cd is known to diffuse into the Cu poor absorber layer and occupying the Cu sites in the lattice thus reducing the acceptor defect density and a causing a consequent type inversion [69]. The band structure of CdS is such that it provides a favorable band alignment with the absorber layer [70]. CdS is a highly n-type material that results in an adequately wide depletion layer that extends into the absorber layer and covers most of the thin CIGS layer. This leads to minimization of tunneling and also to higher voltages [71].

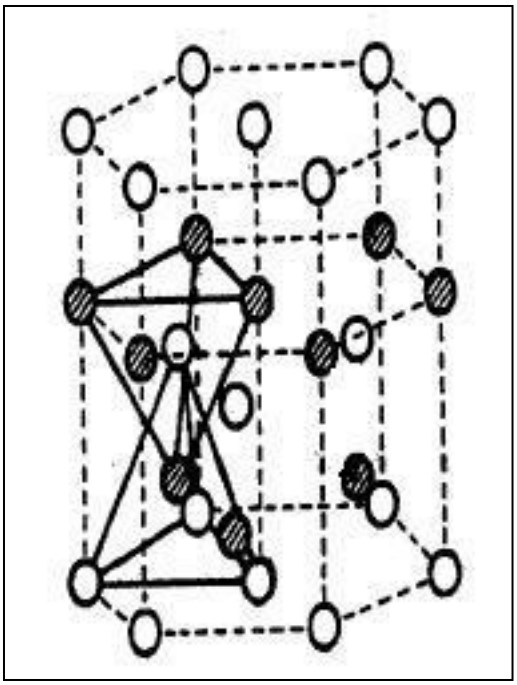

Figure 3.2: Wurtzite Structure of CBD Grown CdS

One of the disadvantages of CdS as a heterojunction partner for CIGS absorber layer is the bandgap limit which restricts the photons from the blue region to reach the absorber as most of the blue photons are absorbed in the CdS layer and are lost due to recombination. It is estimated that the total current loss due to blue photon absorption in CdS is approximately 6 $mA/cm^2$ [72]. Another disadvantage from the industry point of view would be the large amount of hazardous waste disposal and lower material yield.

Such disadvantages have led to the investigation of other materials to replace CdS as a window layer. Some of the other materials considered are ZnSe, $ZnIn_xSe_y$ and $In_xSe_y$ [73]. Moreover, research has been carried out on ZnO as a window layer [74].

### *3.1.4 Transparent and Conducting Zinc Oxide*

The main requirements for a front contact are high conductivity and good transparency. Zinc oxide is the most widely used material for front contact in CIGS solar cells as it has very

high bandgap of 3.3 eV and has good optical and electrical properties. The amount of doping is a tradeoff between the electrical and optical properties. The transmission drops off at higher wavelengths due to the free carrier absorption which is a function of doping concentration. It has a hexagonal wurtzite structure and is typically n-type. ZnO films show a transmission of about 90% between 400-1000nm. ZnO can be deposited by different processing techniques such as sputtering, chemical vapor deposition, etc.

Generally a bi-layer of ZnO is used as a front contact in CIGS thin film solar cells. The first layer is the highly resistive, intrinsic ZnO (i-ZnO) and the second layer is highly n-type layer of ZnO doped with Al (ZnO:Al). The thin i-ZnO layer is necessary to prevent diffusion of Al into the absorber layer thus avoiding the direct contact of the transparent and conducting oxide and CIGS absorber layer of Mo back contact. It is necessary to optimize the thickness of the i-ZnO layer as too thin a layer will not reduce the leakage currents enough and too thick a layer will lead to increase in the series resistance. The thickness of i-ZnO is shown to affect the Voc and the fill factors [75].

## 3.2 Device Fabrication

The sequential steps followed in the fabrication of CIGS/CIGSeS thin film solar cells is briefly discussed in this section.

### *3.2.1 Substrate Cleaning*

As is the case with Integrated circuit technology, in CIGS thin film solar cells it is of utmost importance to carry out thorough substrate cleaning. The reason for such thorough cleaning is that presence of small traces of contaminants is known to have a drastic impact on the device performance. Therefore, a systematic cleaning procedure has been devised in our lab.

Initially a 6”X 4” pieces of either Mo coated glass or plain soda lime glass are cut. This piece is then scrubbed in a special soap solution. The scrubbing is followed by rinsing of the glass substrate in running water for at least five minutes. The substrate is then placed in an ultrasonic bath, containing diluted soap solution in de-ionized (DI) water, for around five minutes. This is followed by rinsing of the substrate in DI water. The substrate is then dipped in an organic solvent, 2-propanol, for about 15 minutes. The substrate is then cleaned in flowing DI water. The substrate is then blow dried using industrial nitrogen. The substrate is immediately mounted in the vacuum chamber. Particular care is taken to minimize the time between the cleaning of the substrate and the mounting of the substrate in the vacuum chamber.

### *3.2.2 Silicon Nitride Barrier Layer Deposition*

A thin alkali barrier layer was deposited on the sodalime glass prior to the deposition of the molybdenum back contact so as to minimize the diffusion of sodium from the sodalime glass during the absorber preparation. Various alkali barrier layers have been used such as silicon nitride, silicon dioxide, aluminum oxide. However, the performance of silicon nitride as an alkali barrier was found to be better when compared to the other barriers [49]. Hence silicon nitride was used as the alkali barrier layer for this research. Silicon nitride was deposited on sodalime glass by reactive radio frequency (RF) magnetron sputtering process using a pure silicon target. Pure silicon target was used because it is cheaper (about one third in cost) and considerably robust as compared to the expensive and brittle silicon nitride ceramic targets. The partial pressure of argon and nitrogen gas mixtures, RF sputtering power and substrate movement duration per unit distance were systematically varied to obtain the desired film thickness of an optimized silicon nitride layer.

The cleaned substrates were mounted in the vacuum chamber and were maintained overnight in high vacuum. A combination of mechanical, turbo molecular pump and cryopump was used to establish a base pressure of ~$2x10^{-6}$ Torr. The base pressure was measured using Bayard Alpert type ionization gauge. Ultrahigh purity argon and nitrogen gas were introduced into the chamber. The pressures of the gases were controlled using mass flow controllers and measured using convectron gauges. The chamber gate valve was throttled to maintain the total pressure at $1.6x10^{-3}$ Torr of Ar:$N_2$::$8x10^{-4}$:$8x10^{-4}$ during the deposition. Depositions were carried out from a silicon target of dimensions 30 cm x 10 cm. The substrates were moved linearly along 10 cm width of the target with the help of a LabVIEW© controlled stepper motor. The sputtering process was performed under various power and substrate movement duration per unit distance to deposit films with a nominal thickness of ~750 – 1000 Å.

### *3.2.3 Mo Back Contact Deposition*

For this research, commercially available Mo coated sodalime glass was used as well as Mo deposition is carried out on ordinary sodalime glass. A diffusion barrier layer of silicon nitride is deposited prior to deposition of Mo. After the substrate is cleaned thoroughly as mentioned in the earlier section, it is placed in the deposition chamber. The deposition chamber is kept overnight in high vacuum to remove water and other contaminant vapors from the substrate. Silicon nitride deposition is carried out by reactive DC magnetron sputtering of silicon target in $N_2$/Ar ambient. This is followed by DC magnetron sputtering of Mo in Ar ambient. A Mo target of dimensions 30 cm x 10 cm was used and the target-substrate distance was maintained at 6 cm. CuGa and In targets used in this research have the same size as the Mo target and the target-substrate distance was also maintained at 6 cm. To achieve uniform thickness the

substrate was moved linearly over the Mo target along its width. Thickness variation in the range of ± 3% over a width of 10 cm and of ±5% over a width of 15 cm was achieved [76]. An extensive research was carried out earlier to optimize the process parameters for Mo deposition. It was concluded that a three layered Mo gave the optimum performance. Here the first and third layers were deposited by the high power and lower pressure cycle (300 W / 3 X $10^{-4}$ Torr). The middle layer was deposited by the low power and high pressure cycle (200 W / 5 X $10^{-3}$ Torr) [33]. Efforts will be continued to further optimize the Mo back contact layer in order to improve the overall device performance.

### *3.2.4 Sodium Precursor Deposition*

As mentioned earlier, various compounds can be used as sodium precursors. Among the available sodium precursors, NaF is stable in air, non-hygroscopic and evaporates stoichiometrically. Hence in this research, NaF was used as the sodium precursor. After the deposition of molybdenum back contact the substrates were allowed to cool down for ~2 hours in the sputtering chamber. The substrates were immediately moved to the evaporation chamber for the NaF deposition. A combination of mechanical and diffusion pump in combination with a liquid nitrogen trap was used to maintain high vacuum. The advantages of diffusion pump are low maintenance cost, low running cost, high pumping speed and reliability. The major disadvantage of diffusion pumps is the tendency to backstream oil vapors into the vacuum chamber. A liquid nitrogen trap was used to minimize backstreaming of the oil vapors. The NaF layer was deposited by the thermal evaporation process. The thickness of the NaF layer was varied from 40 Å to 120 Å. The distance between the substrate and the boat was ~7 inches. The power was adjusted to maintain the rate of deposition at ~1 Å per second. The total thickness and

the deposition rate were measured with "*Inficon XTC/2*" quartz crystal thin-film deposition controller. After the deposition, the gate valve to the diffusion pump was closed and the substrate was allowed to cool for ~2 hours.

### *3.2.5 CIGS/CIGSeS Absorber Layer Deposition*

For this research, a two step process is adopted in the deposition of CIGS/CIGSeS absorber layer. The first step consists of deposition of metallic precursors namely; Cu, In and Ga. These metallic precursors are then converted to CIGS/CIGSeS by annealing the metallic precursors in selenium and sulfur ambient at high temperatures. This second step is known as selenization and sulfurization respectively. The annealing of the metallic precursors is carried out by two ways namely; in conventional furnace and by rapid thermal processing (RTP).

The metallic precursors are deposited by DC magnetron sputtering from Cu-Ga alloy target (78 at.% Cu and 22 at.% Ga) and In target in Ar ambient. The substrate is made to m ove linearly along the width of the target and the speed is adjusted in order to achieve desired thickness. The metallic ratios are adjusted by adjusting the thickness of the metallic precursors. The metallic ratios are expected to be directly proportional to the thickness of each layer which in turn is inversely proportional to the speed of substrate movement or directly proportional to the time for which the moving substrate receives the sputtered species.

After the deposition of the metallic precursors with desired thickness the substrate is now placed in a conventional furnace and vacuum is taken in this chamber. The substrate is slowly heated to some intermittent temperature and then a metal-organic selenium source is introduced in the chamber along with $N_2$. The substrate is then heated to temperature above 500 °C at variable ramp [33]. For formation of CIGSeS absorber layer $H_2S$ is introduced in the furnace as

source of sulfur during the dwell time at higher temperatures. The substrate is then allowed to cool. The cooling rate is increased by placing a high speed fan directed towards one end of the furnace. The substrate is cooled in an inert ambient of $N_2$ to avoid any further addition of selenium or sulfur in the film. Optimization of the time-temperature profile used in the conversion of the metallic precursors into CIGS/CIGSeS is one of the topics of this research.

### *3.2.6 CdS Heterojunction Partner Deposition*

A layer of the heterojunction partner CdS is deposited using the chemical bath deposition (CBD) technique. Earlier, a new setup for CBD of CdS on 10 cm x 10 cm glass and stainless steel substrates was designed and developed [77]. Figure 3.3 shows the experimental setup used for the CdS deposition using CBD technique [78].

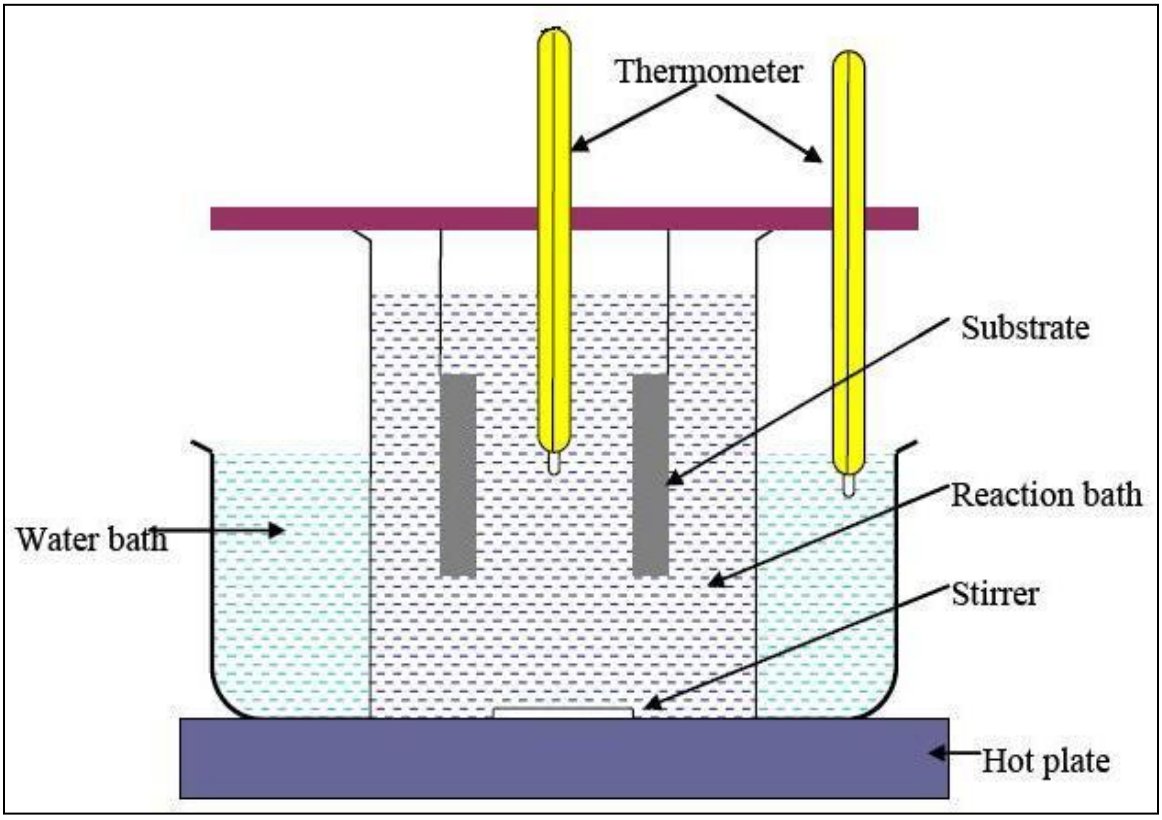


Figure 3.3: Experimental Setup for Chemical Bath Deposition

An aqueous alkaline solution with pH> 9, prepared in a beaker by addition of $NH_4OH$ as a complexing agent, 0.015M $CdSO_4$ as cadmium source, 1.5M Thiourea as sulfur source, is placed in a hot water bath. The temperature of this hot water is controlled such that requisite temperature of CdS deposition is achieved. The deposition is generally carried out in the range of 60 to 80 °C. A ~50 nm thick CdS layer is grown on the absorber layer using CBD technique.

### *3.2.7 Transparent and Conducting i-ZnO/ZnO:Al Deposition*

Bilayer of transparent and conducting i-ZnO/ZnO:Al is deposited using RF magnetron sputtering. After deposition of CdS by CBD the substrate is mounted in the vacuum deposition chamber and kept overnight in high vacuum. This aids in reducing the water vapor content from the surface of the substrate. The substrate is moved linearly along the width of the sputtering targets to at calculated speed to achieve the desired thickness. Research was carried out earlier at FSEC Thin Film PV Lab to optimize the process parameters for deposition of the front contact [79]. This served as the baseline process for deposition of front contact for this research. A thin layer of ~ 50 nm i-ZnO layer is deposited at RF power of 200 W and argon pressure of 1.5 mTorr and ~ 500 nm thick ZnO:Al is deposited at RF power of 300 W and argon pressure of 1.5 mTorr. ZnO:Al film with sheet resistance of 40-60 Ω/□ and transparency of ~90% is routinely deposited using this process. These parameters are known to be adequate for the preparation of highly efficient CIGSeS thin film solar cells.

### *3.2.8 Cr/Ag Front Contact Finger Deposition*

Cr/Ag front contact fingers are deposited though a metal mask using thermal evaporation. First ~50nm thick Cr is deposited followed by ~1 µm of Ag. Cr is deposited as a barrier layer to avoid diffusion of Ag into the ZnO:Al front contact layer. Moreover, Cr provides better adhesion

to ZnO than Ag. The metal mask is designed for preparation of cells with the total area of ~0.43 $cm^2$ so as to maximize the active area of the cell. The metal mask also provides a front contact pad so as to minimize shadowing of the active area by the probes during I-V measurement.

### 3.3 Material Characterization

Various material characterization techniques are used to aid in optimizing the process parameters. Electron Probe Micro Analysis (EPMA) is used to find out the metallic ratios and the cation ratio in the absorber film. X-ray diffraction (XRD) is carried out on the absorber film to calculate the lattice constant of the CIGS and CIGSeS films and thus the ratios of Ga/(In+Ga) and S/(Se+S). Moreover, XRD provides information on preferred orientation of the grown films. Optical microscopy followed by scanning electron microscopy (SEM) is used to characterize the surface morphology of the absorber layer. SEM images provide vital information such as the grain size and compactness of the absorber film. Moreover, cross-section SEM image indicates the presence of voids in the absorber film, if any, and also provides some information about the absorber and back contact interfaces. Transmission electron microscopy (TEM), Auger electron spectroscopy (AES), Secondary ion mass spectroscopy (SIMS) is carried out on selected samples to find bulk material properties and various interface properties and to find out the elemental depth profile in the absorber film respectively.

### 3.4 Electrical Characterization

After the devices are fabricated, I-V measurements are carried out using an in-house designed and built I-V setup. The I-V setup consists of Kepco power supply, Agilent technologies multimeter. The power supply and multimeter are interfaced to the computer using a Labview program. The Labview program also determines solar cell parameters such as open

circuit voltage (Voc), short circuit current (Isc), voltage and current at the maximum power point (Vmp and Imp), fill factor and consequently efficiency of the fabricated CIGS thin film solar cell. The AM 1.5 global spectrum conditions are simulated using a lamp with the intensity of one sun.

Before the measurements are done the absorber layer is scrapped off to make contact with the Mo layer. A layer of indium is soldered onto the Mo back contact layer to make better contact with the probes. One probe is placed on this indium soldered Mo back contact and the second probe is placed on the Cr/Ag contact pad to complete the circuit. The solar cell is biased over a range of -0.2 to 0.5 V and an I-V curve is plotted.

Quantum efficiency (QE) measurements are carried out on the completed solar cells to calculate the bandgap of the absorber layer.

# CHAPTER 4 RESULTS AND DISCUSSIONS

## 4.1 Interdiffusion of Metallic Precursors

In order to optimize the process parameters for selenization of metallic precursors, it is essential to understand the kinetics and mechanisms of phase transformation of the metallic precursors into CIGSeS absorber layer. Therefore, the metallic precursors were annealed to certain low temperatures for a fixed period of time that simulated the time-temperature profile of a baseline process that was set earlier. The metallic precursors were precursors were subjected to two different annealing cycles namely, 100°C for 15 min. and 120°C for 10 min. Material properties and alloy formation for these annealed precursors along with the as-deposited precursor were studied using X-ray diffraction and Auger electron spectroscopy.

Some intermixing of Cu and In was observed even in the as-deposited films due to the high energy of arriving atoms during sputtering. With increasing temperature intermixing of Cu and In increases, as expected. Figures 4.1, 4.2, and 4.3 show the AES depth profile of as-deposited film, film annealed at 100 °C for 15 min. and film annealed at 120 °C for 10 min.

XRD patterns showed that Cu-In binary phases were formed even in as deposited films. CuIn peak at $2\theta = 34.8°$ and 38.9°, $CuIn_2$ peak at $2\theta = 33.6°$, Cu peak at $2\theta = 43.6°$ and Mo peak at $2\theta = 40.8°$ were observed. The proportion of CuIn, $CuIn_2$ and non-alloyed Cu varied as follows: 0.43, 0.17, and 0.40 for as-deposited film, 0.47, 0.13, and 0.40 for 100°C/15 mins sample, 0.51, 0.09, 0.39 for 120°C/10 mins sample. Figures 4.4, 4.5, and 4.6 show the XRD patterns of each sample.

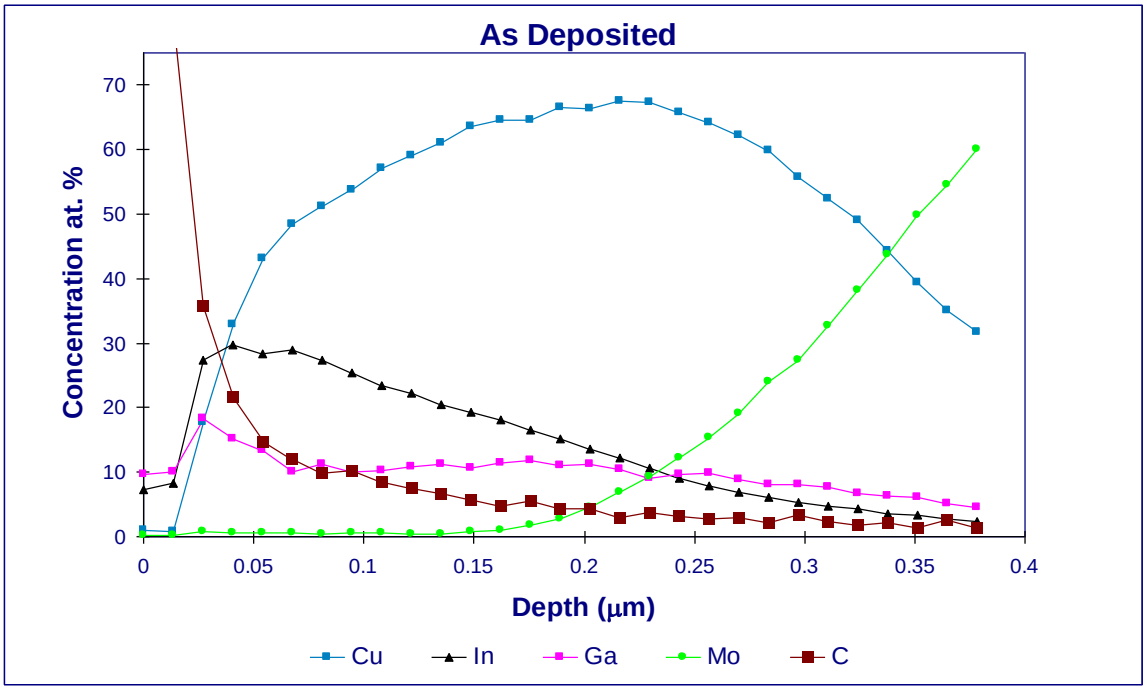


Figure 4.1: AES Depth Profile of As Deposited Film

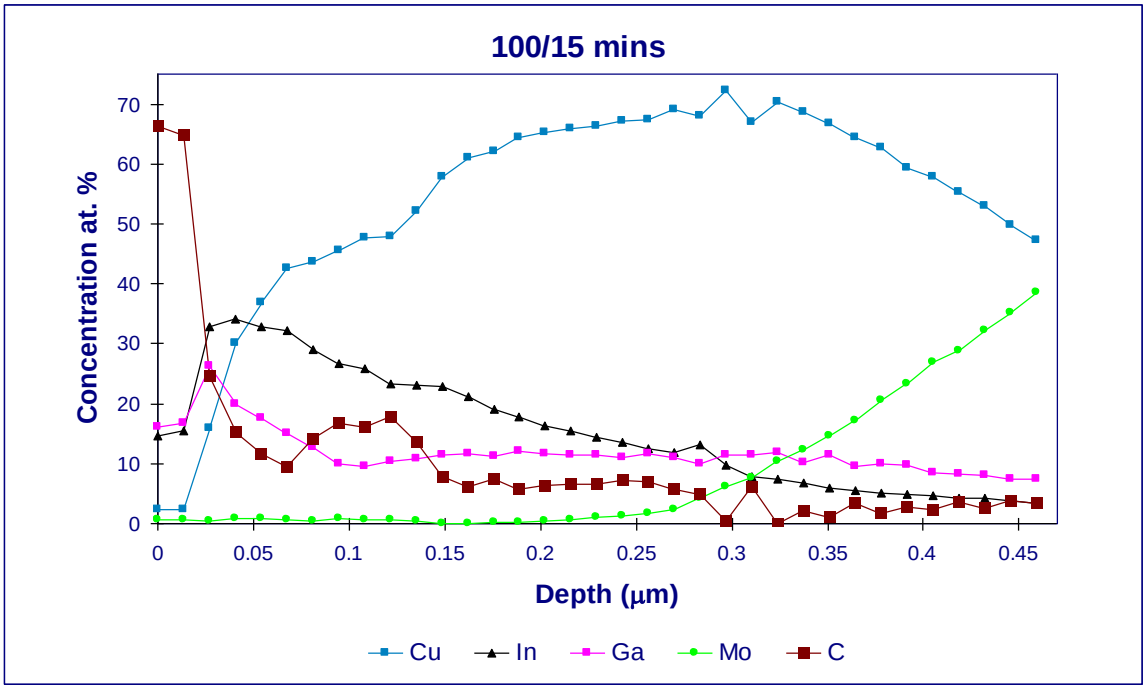


Figure 4.2: AES Depth Profile of Film Annealed at 100 °C for 15 mins

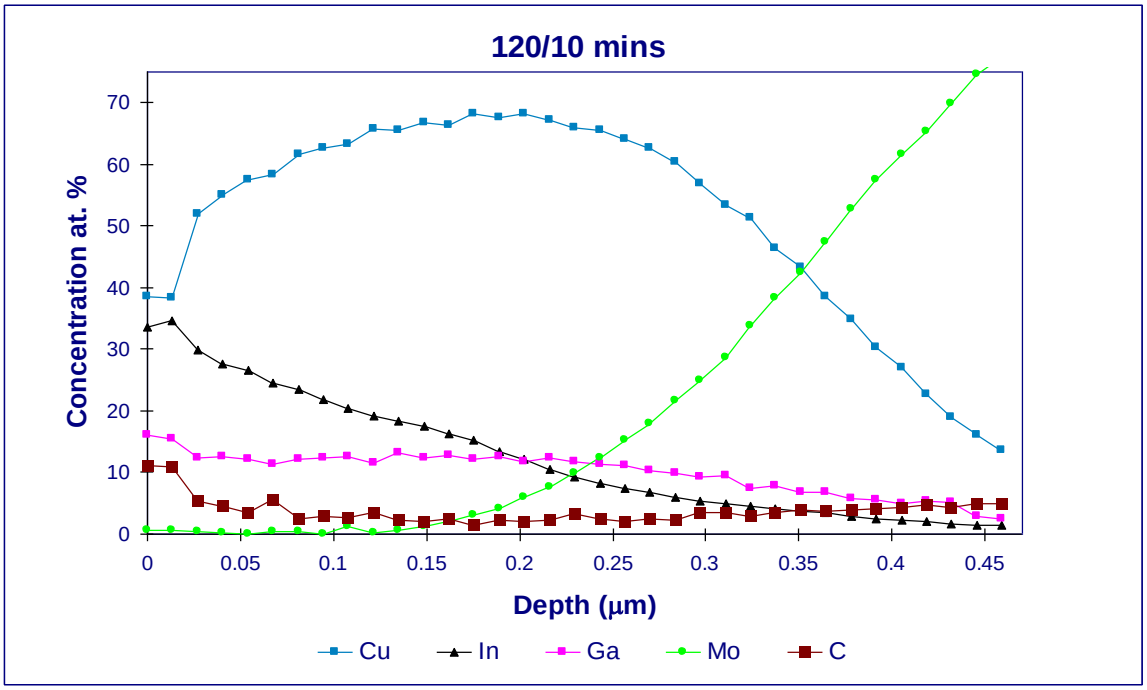


Figure 4.3: AES Depth Profile of Film Annealed at 120 °C for 10 mins

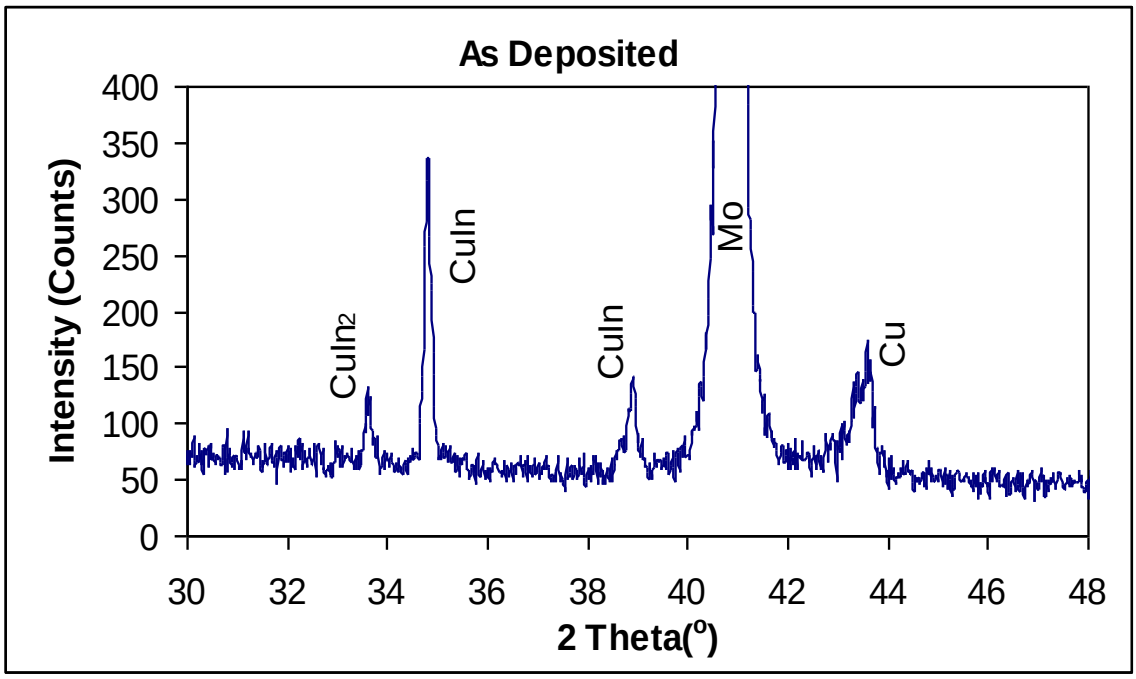


Figure 4.4: XRD Pattern of As Deposited Film

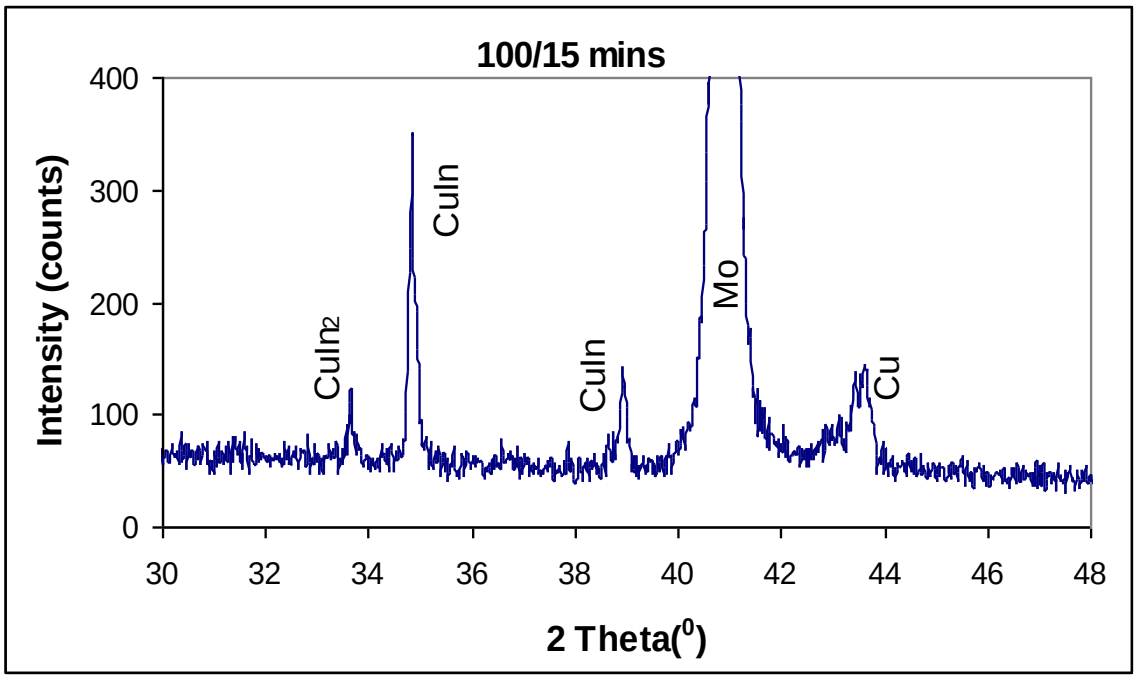


Figure 4.5: XRD Pattern of Film Annealed at 100 °C for 15 mins

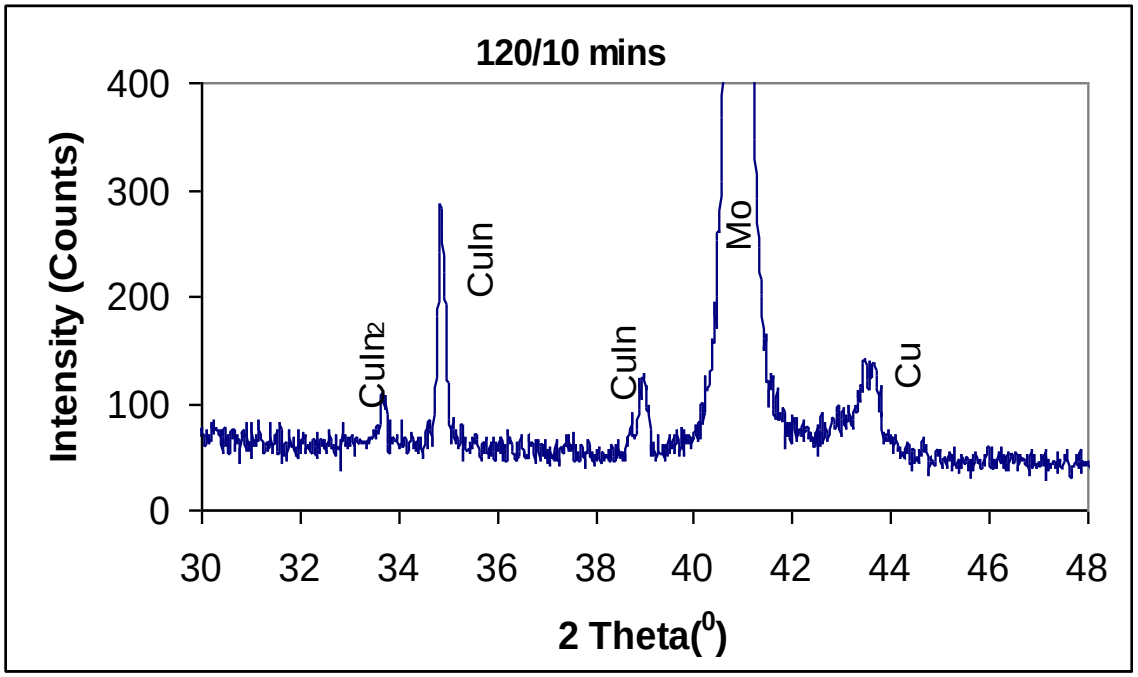


Figure 4.6: XRD Pattern of Film Annealed at 120 °C for 10 mins

The AES depth profile and the XRD pattern suggest that the Cu-In binary phases are formed throughout the bulk of the material. Intermixing and CuIn phase formation helps in avoiding formation of detrimental binary phases. The decreasing proportion of non alloyed Cu with increasing temperature suggests that Cu diffusion is the mechanism for transformation to CuIn and $CuIn_2$.

Based on these result a modification was made to the standard selenization process. In the standard selenization process, the selenium precursor was introduced at room temperature. In the modified selenization process the selenium precursor was introduced at higher temperature in the range of 140 °C to 145 °C. It was essential to introduce to the selenium precursor before the temperature crossed 156 °C which is the melting point of indium. Figure 4.7 shows the optical images of samples prepared by the standard selenization process and the modified selenization process. As can be seen from the figure the density of features on the absorber surface has reduced in the modified process. The improvement in the surface morphology was attributed to the better intermixing of the precursor. The hypothesis made here is that the selenium precursor when introduced at room temperature starts reacting with the metallic precursor thus reducing the intermixing of the precursors. This can result in the presence of elemental indium which beyond 156 °C is liquid-like and results in the micrononuniformities. The features or the micro non uniformities can result in increased shunting thus reducing the device performance.

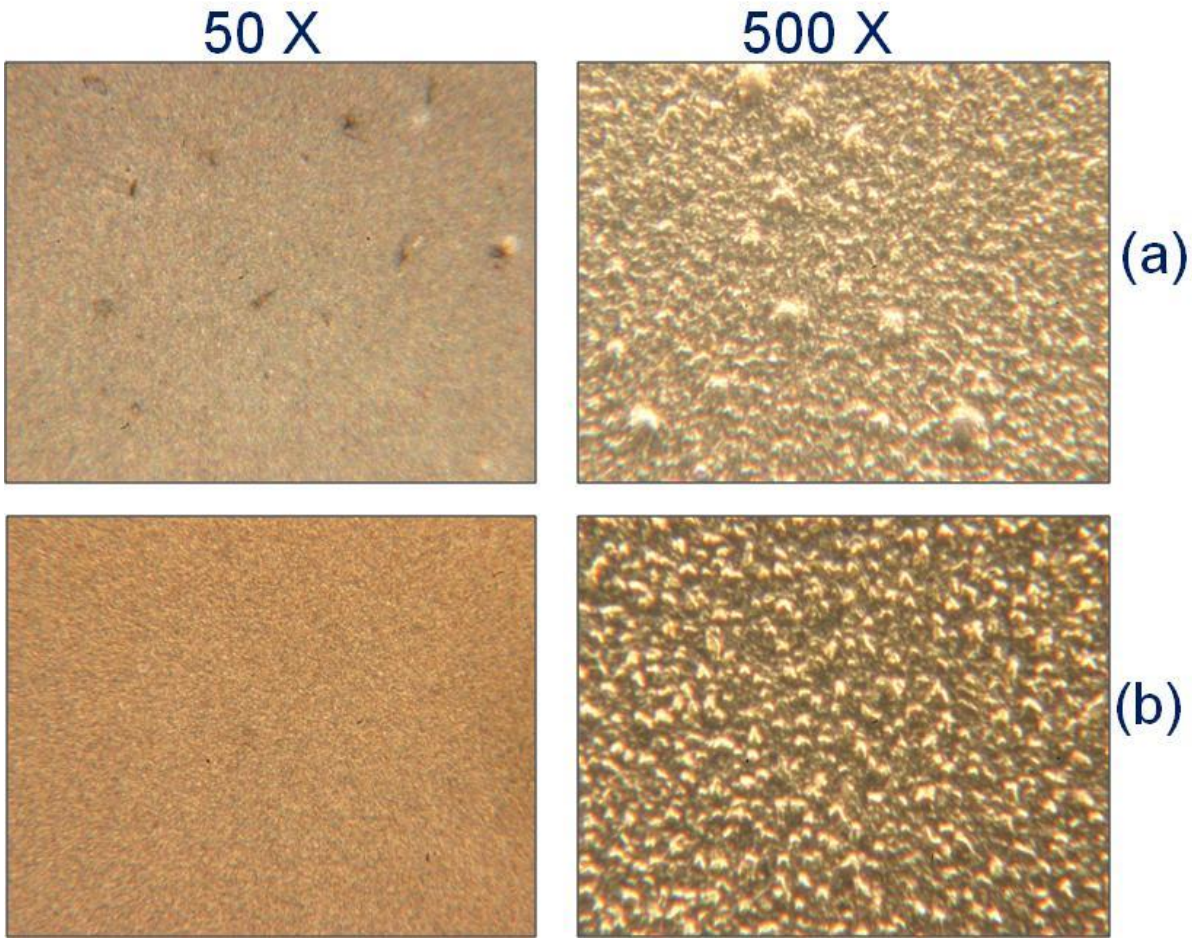


Figure 4.7: Optical Images of Absorber prepared by the standard and the modified selenization process

## 4.2 Very Thin (<1 µm) CIGS Thin Film Solar Cells Prepared in Conventional furnace

Experiments were carried out for reducing the thickness of the absorber layer from the present ~2.5 µm to <1 µm. The metallic precursors CuGa and indium were deposited using DC magnetron sputtering technique. The thickness of the metallic precursors was reduced to one third. Experiments were carried out to optimize the selenization time and also optimize the NaF thickness. The samples were etched in 10% KCN to remove Cu rich layer.

### *4.2.1 Effect of Selenization Time*

It is essential to optimize the annealing time –temperature profile during the second step i.e selenization in the preparation of the absorber film. Longer duration of annealing step would aid in improving the grain structure of film as well as aid in homogenization of the film. However, the presence of selenium during this annealing step results in selenium reacting with the molybdenum back contact. The reaction of molybdenum film with selenium results in the formation of $MoSe_2$ layer. As mentioned earlier $MoSe_2$ layer is highly p-type and at very low thickness helps in forming an ohmic contact. Essentially it acts a tunnel diode thus forming a near ohmic back contact for CIGS thin film solar cells. However, as the thickness of the $MoSe_2$ layer increase it again leads to a formation of Schottky contact resulting in higher recombination at the back contact. Therefore, it is essential to strike a balance while optimizing the selenization time-temperature profile. Therefore, experiments were carried out with varying selenization time keeping the selenization temperature constant. The purpose of this experiment was to understand the effect of duration of selenization on the absorber film as well as the device performance. Based on these experiments the optimal selenization time could be defined for absorber films with reduced thickness.

Three selenization times of 60, 45 and 30 minutes were experimented with while keeping the selenization temperature constant at 515 °C. The cells were completed by deposition of CdS heterojunction partner layer using CBD, window bilayer of i-ZnO/ZnO:Al by RF magnetron sputtering, and then Cr/Ag contact fingers by thermal evaporation. Current-voltage (I-V) characteristics were obtained for these cells using the I-V setup that was built in-house. Figures 4.8 to 4.10 show the variation in various PV parameters with respect to the selenization time.

It can be seen from the figures below that as the selenization time was reduced all the PV parameters improved. As mentioned earlier, the thickness of $MoSe_2$ layer is directly dependent on the selenization time. Therefore, as the selenization time is reduced the thickness of the MoSe layer is also reduced thus making a near ohmic contact at the back. Hence, the recombination losses near the back contact are reduced thus improving the current density. As can be seen the reverse saturation current is reduced by an order of magnitude for sample selenized for 30 minutes, which can explain the increase in the open circuit voltage.

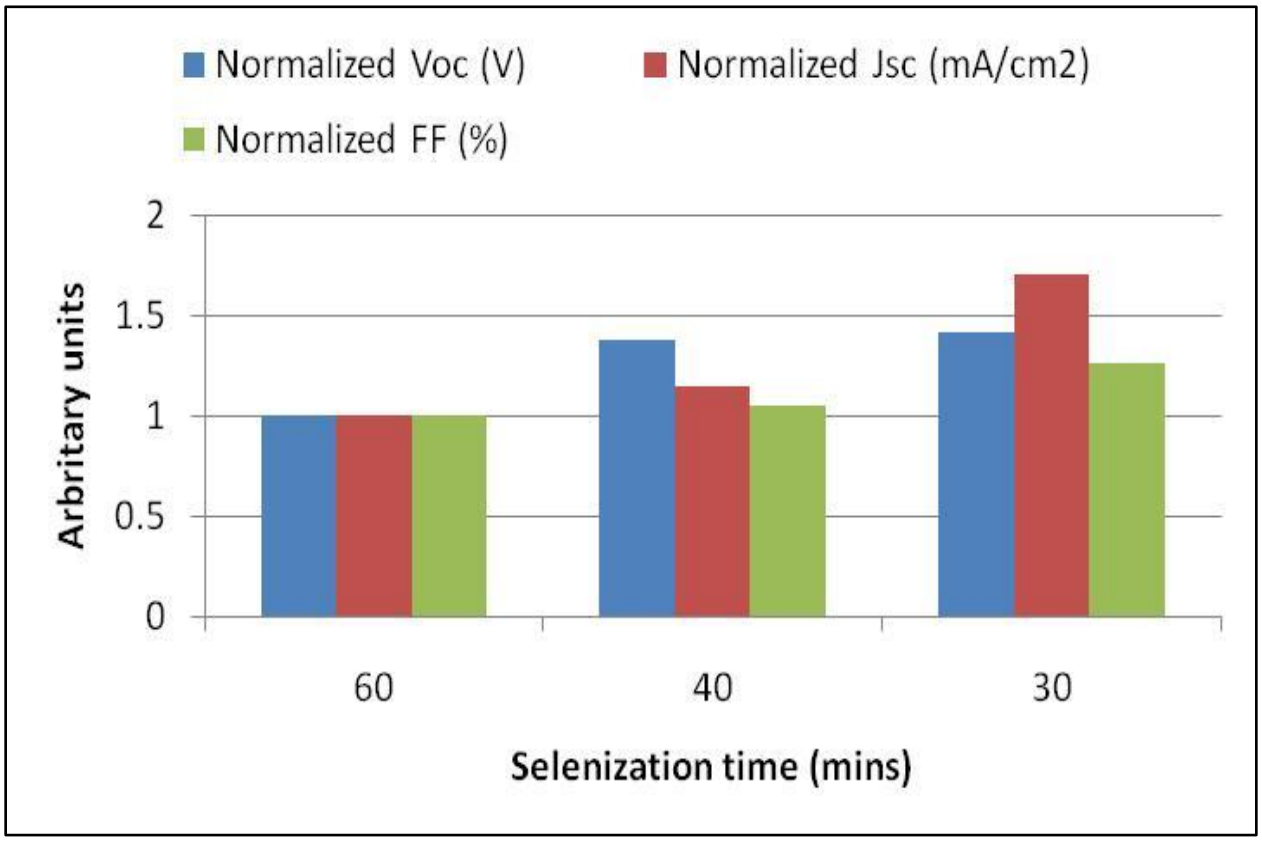


Figure 4.8: Variation of Open Circuit Voltage, Short Circuit Current Density, and Fill Factor with varying selenization time

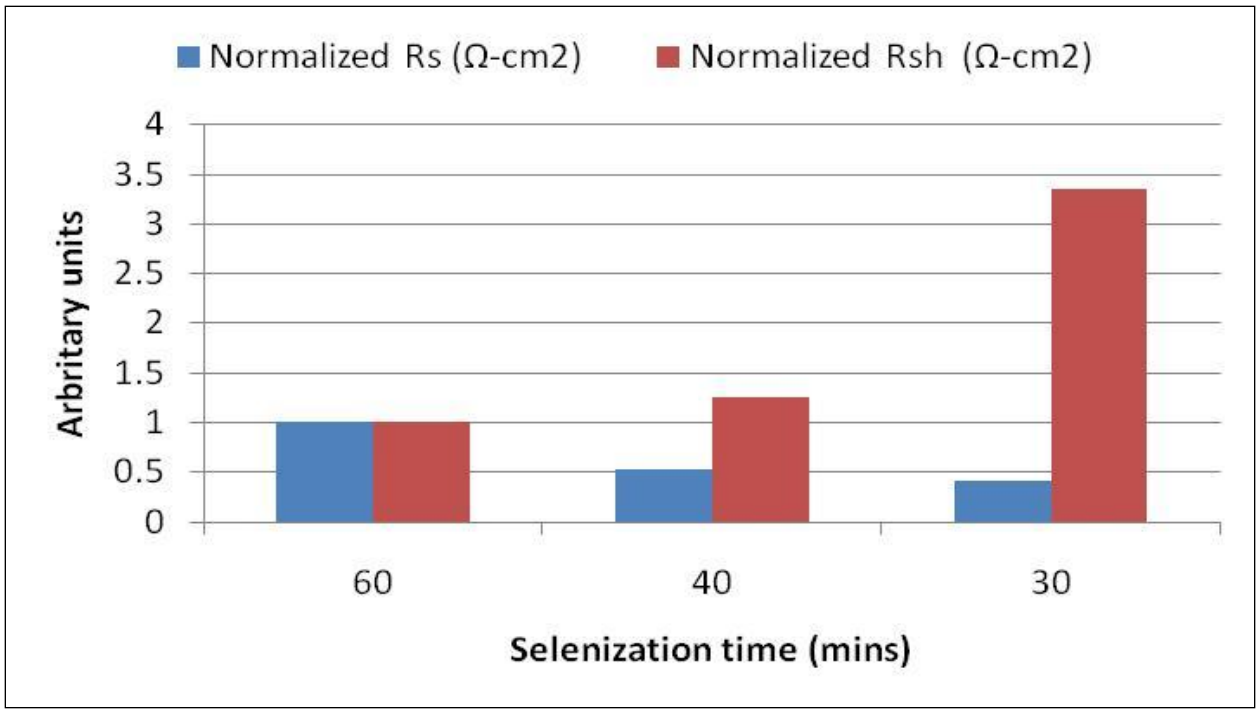


Figure 4.9: Variation of Series and Shunt Resistance with varying selenization time

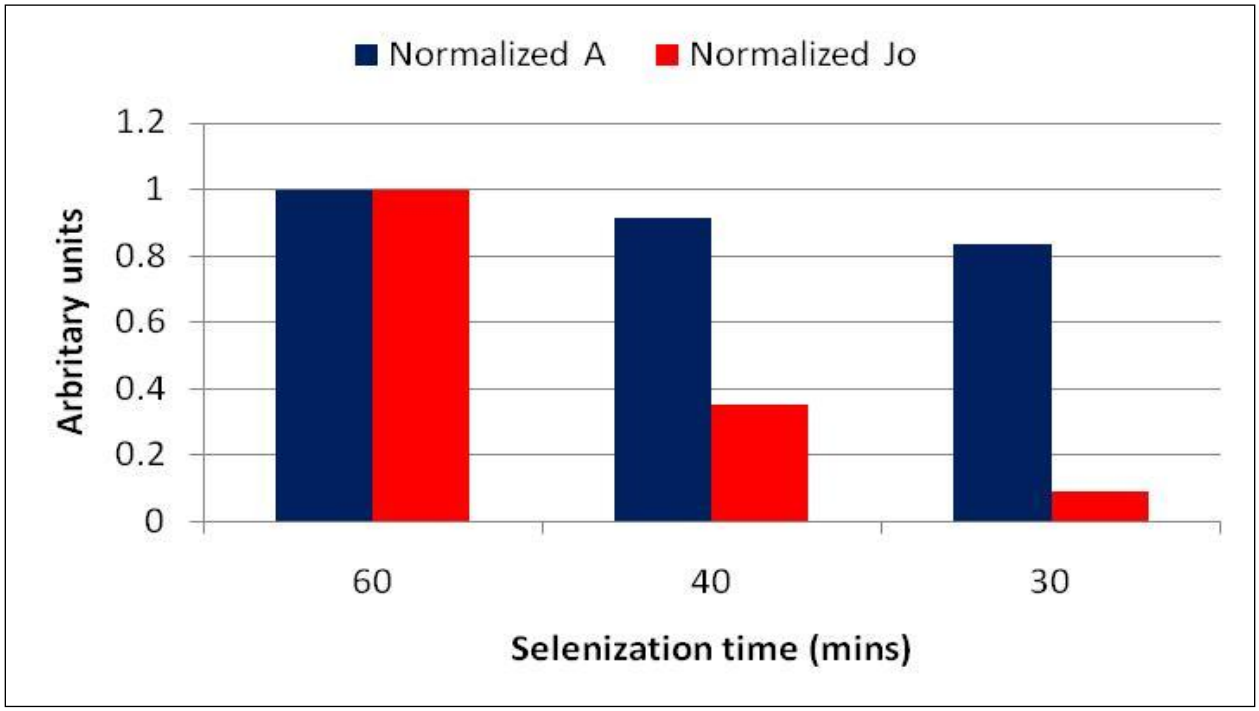


Figure 4.10: Variation of Diode Ideality Factor and Reverse Saturation Current with varying selenization time.

### *4.2.2 Effect of Varying NaF Thickness*

It is already known that the presence of sodium during the preparation of CIGS absorber is beneficial for the film. The benefits of sodium are multifold. Generally, the soda lime glass is the source of sodium; where in the sodium from the sodalime glass diffuses into the absorber film at high processing temperatures. However, this diffusion is not very well controlled and can be nonuniform resulting in micrononuniformities. The micrononuniformities result in non uniformity of device performance over large areas. Unfortunately, device performance over large areas is governed by the weakest link. Moreover, it is also possible that adequate amount of sodium will not diffuse from the sodalime glass causing degradation of device performance. Therefore, a known amount of sodium precursor, NaF, was deposited on the sample prior to the deposition of the metallic precursors. It has been proven in literature that 0.1at% of sodium is optimum for preparing device quality absorber films [48]. Therefore, as the absorber thickness reduces it is essential to optimize the NaF thickness in order to optimize the amount of sodium Attempts were made to verify whether the optimum amount of NaF was the same for the different processes or whether it was process dependent. In order to optimize the amount of sodium CIGS absorbers were prepared with various NaF thicknesses.

Four 1" X 4" Mo-coated sodalime glass (with a thin barrier layer) samples were used for this experiment. The first sample was kept with no NaF deposited on it. The other three samples had 30, 60 and 90 Å NaF deposited on them. These samples were then taken to the sputtering system and the metallic precursors were deposited on them. The four samples were then transferred to the conventional furnace for selenization. The samples were selenized for 40 minutes at 515 °C. Thus, it was made sure that only difference between these samples was the

amount of available sodium. Heterojunction partner, CdS was deposited by chemical bath deposition followed by RF sputtering of undoped ZnO and ZnO:Al TCO layers on 1" X 2" samples. The cells were completed by deposition of Cr/Ag contact fingers by thermal evaporation. The other 1" X 2" piece from each sample was used for scanning electron microscopy and X-ray diffraction analysis.

Figures 4.11 and 4.12 show the optical images and scanning electron microscopy images of the samples with various NaF thicknesses, respectively. As can be seen from the figures the grain size increases with increasing sodium content. Moreover, small features were visible on the sample with No NaF deposited on it. It should be noted that for these experiments a thin barrier layer was deposited prior to the deposition of the molybdenum back contact layer.

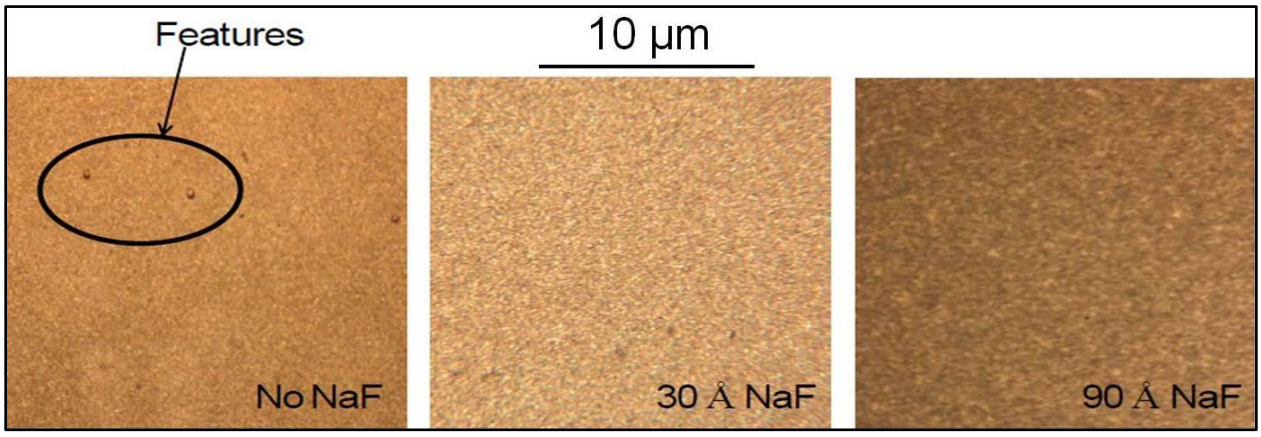


Figure 4.11: Optical Microscope images at 50X magnification for varying sodium content

Therefore, some sodium from the soda lime glass would have diffused into the absorber layer. This could explain that effect of sodium content is not observed on the surface morphology of the absorber films. The hypothesis here is that presence of sodium tends to affect the grain structure as mentioned in literature; however, actual sodium content does not have much control on the morphology of the absorber films.

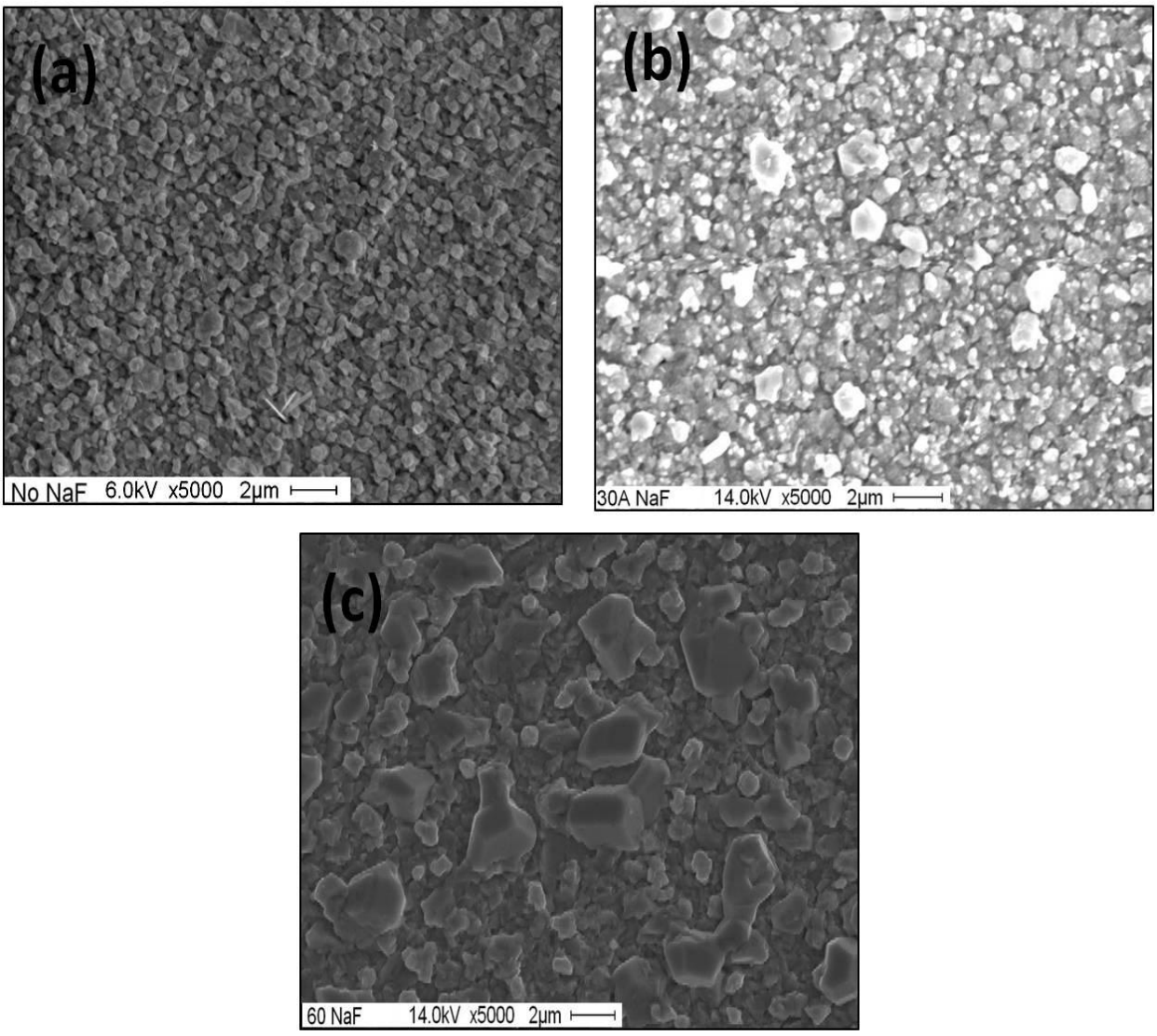


Figure 4.12: SEM images for samples with (a) No NaF, (b) 30Å NaF and (c) 60 Å NaF

Figure 4.13 shows the x-ray diffraction of the absorber films with varying NaF thickness. Based on the XRD graphs the preferred orientation of the films was determined. The detailed calculation for determining the preferred orientation is described in Appendix A. It can be seen that with increasing sodium content the absorber films tend to grow more preferentially in the 112 direction. This preferred orientation can be explained by the formation of the $NaInSe_2$

compound which aids in growing the grains in the 112 orientation. Table 4.1 shows the preferred orientation for varying NaF thickness.

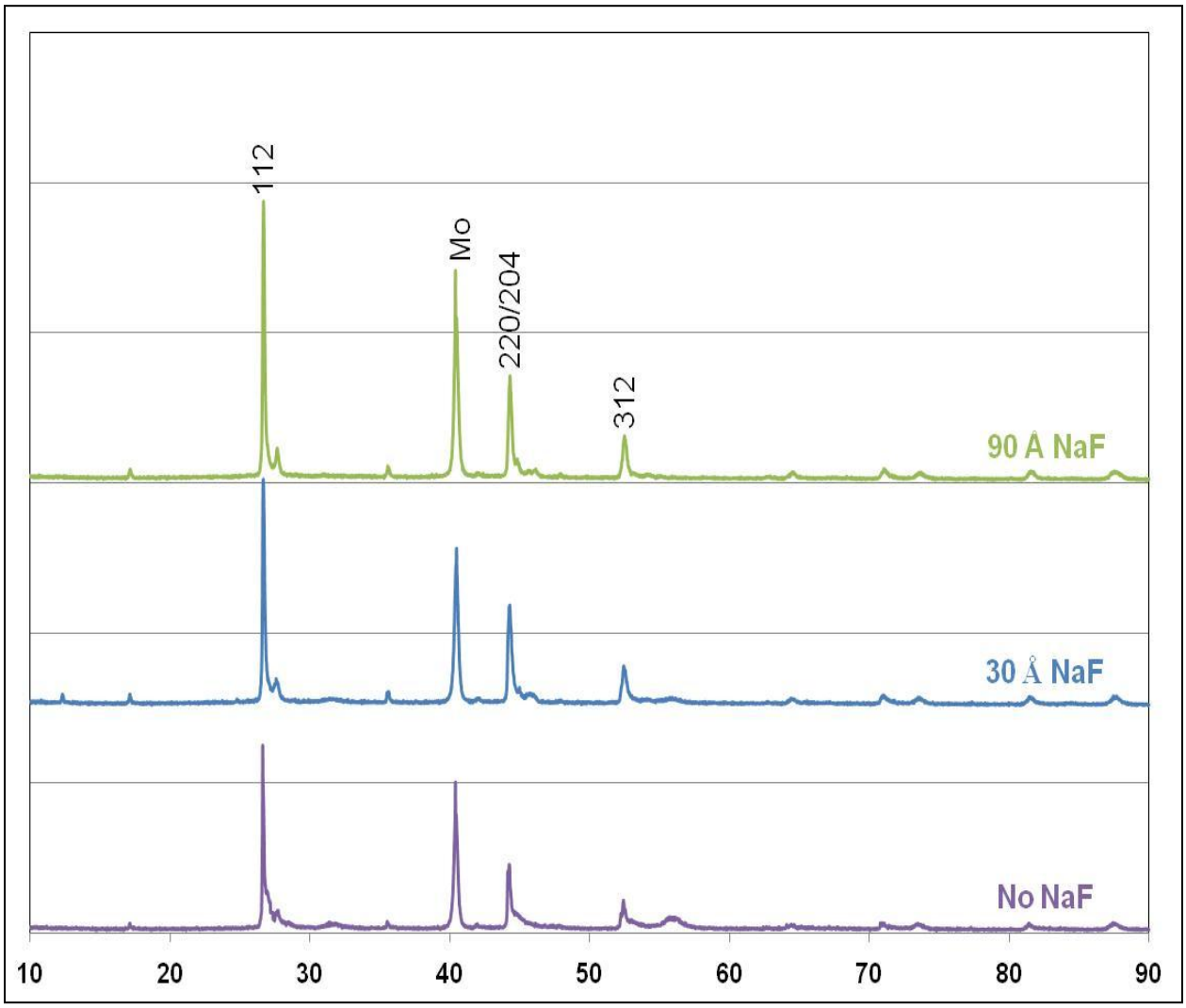


Figure 4.13: XRD Spectra for CIGS with varying NaF thickness

Table 4.1: Degree of Preferred Orientation for Varying NaF Thickness

| Orientation | Degree of Preferred Orientation | | |
|---|---|---|---|
| | No NaF | 30 Å NaF | 90 Å NaF |
| 112 | 0.945 | 0.977 | 1.231 |
| 220/204 | 0.627 | 0.724 | 0.713 |
| 312 | 0.536 | 0.639 | 0.604 |

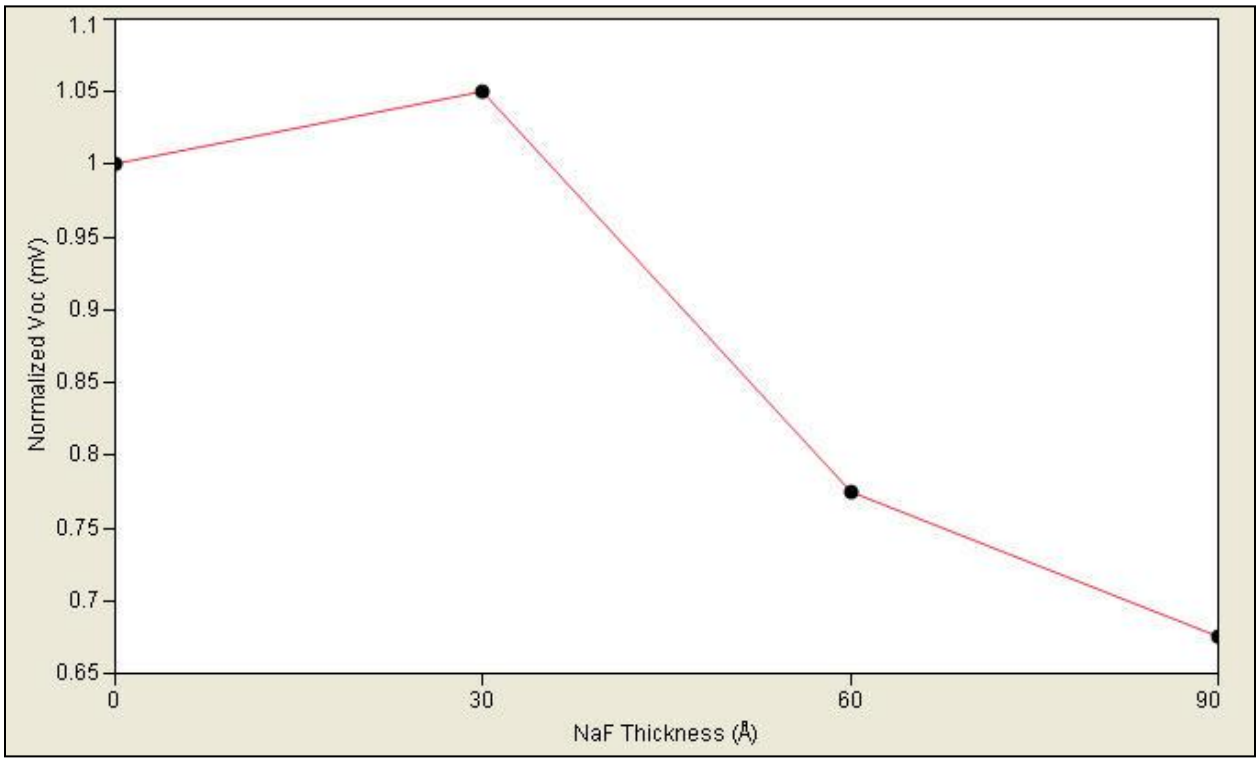

Figure 4.14: Variation in normalized Open Circuit Voltage with NaF thickness

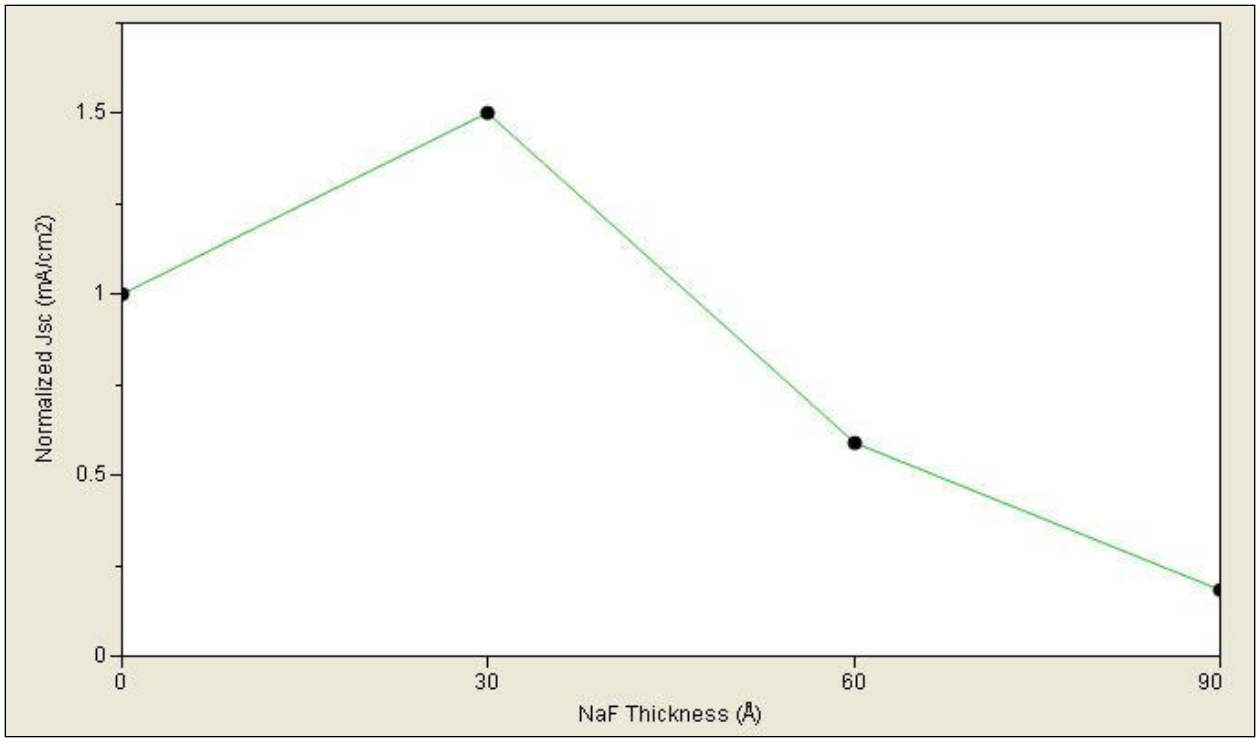


Figure 4.15: Variation in normalized Short Circuit Current Density with NaF thickness

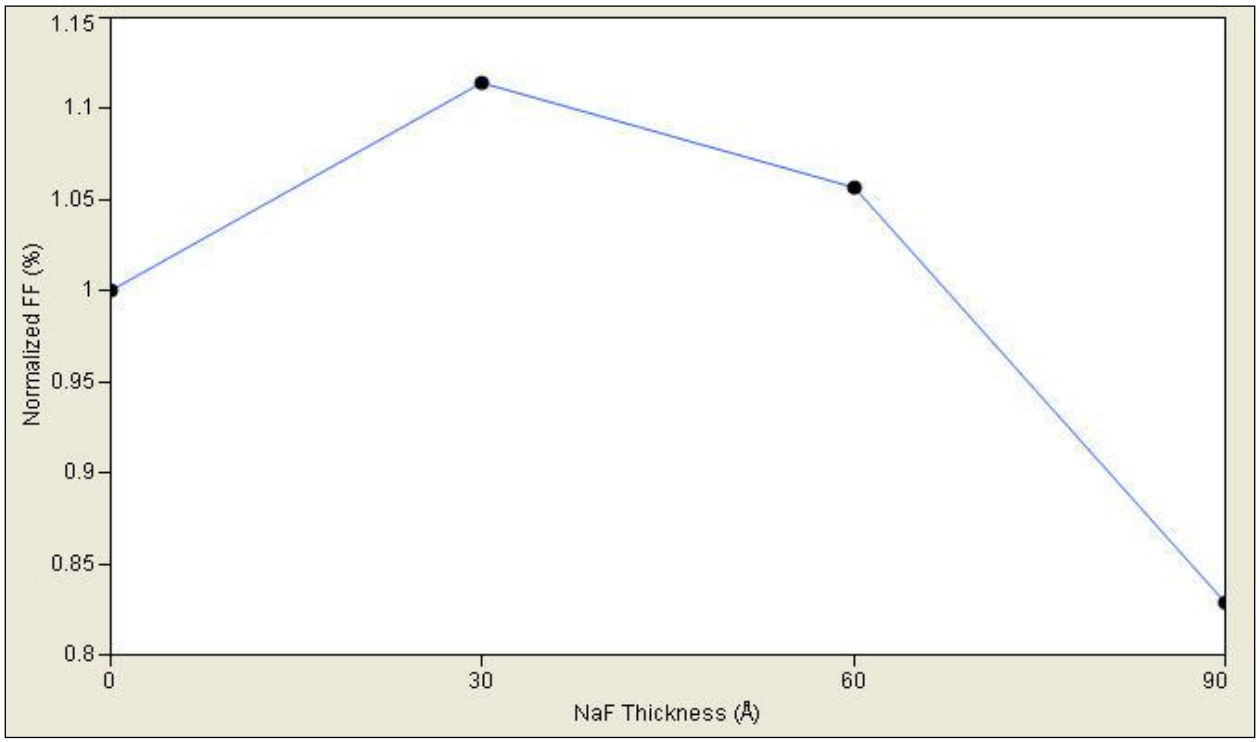


Figure 4.16: Variation in normalized Fill Factor with NaF thickness

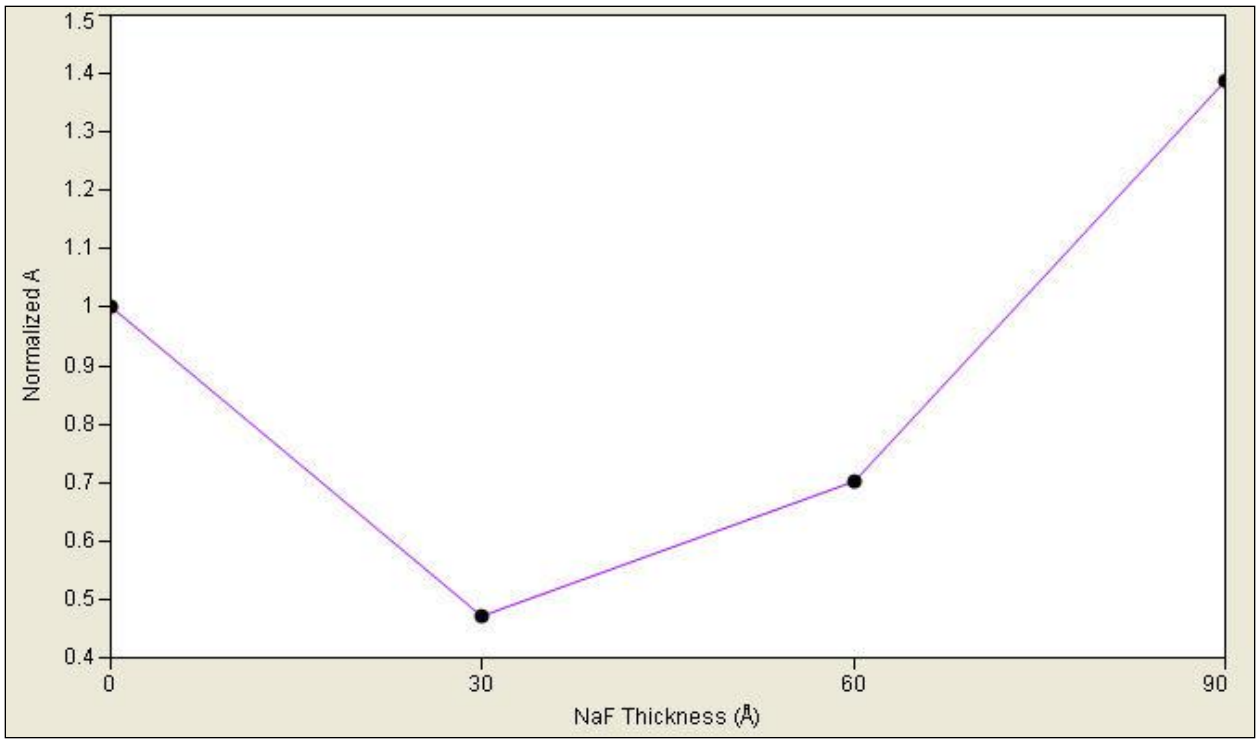


Figure 4.17: Variation in normalized Diode Ideality Factor with NaF thickness

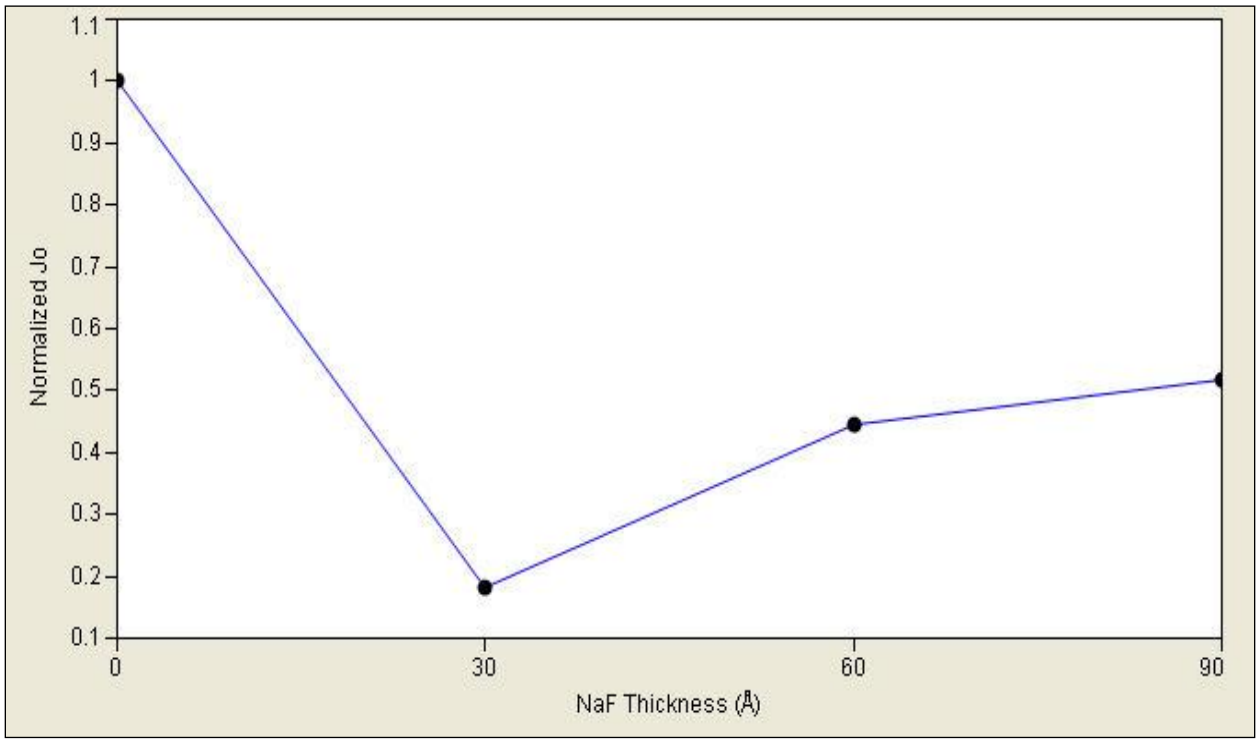


Figure 4.18: Variation in normalized Reverse Saturation Current with NaF thickness

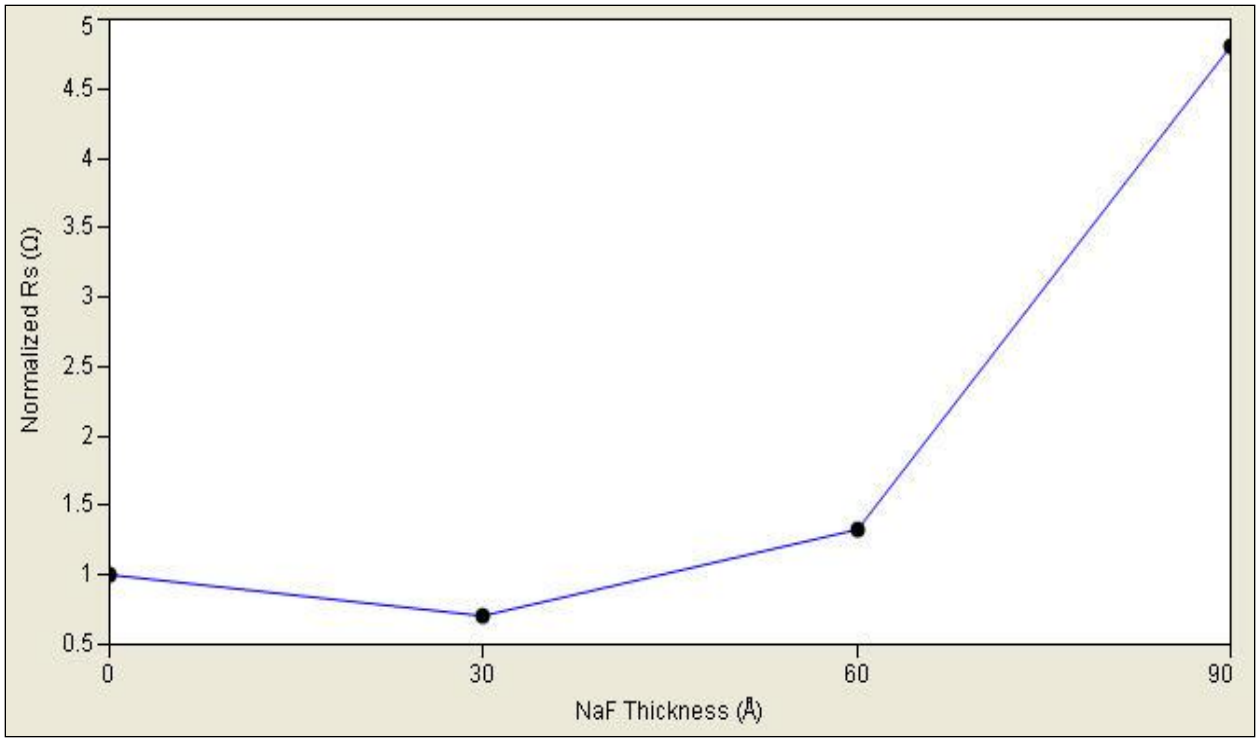


Figure 4.19: Variation in normalized Series Resistance with NaF thickness

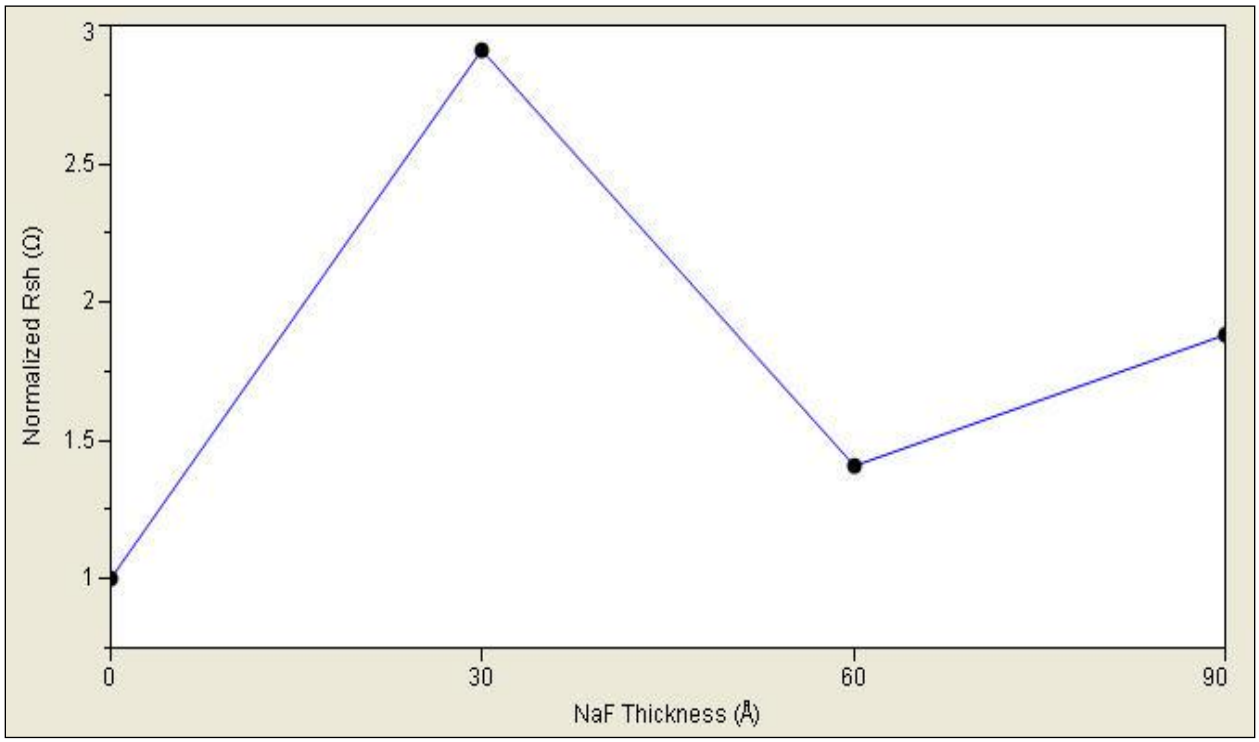


Figure 4.20: Variation in normalized Shunt Resistance with NaF thickness

As can be seen from the above figures 4.14 to 4.20 the sodium content tends to affect the device performance. It can be concluded from this experiment that there is optimum amount of sodium that tends to favor the device performance beyond which the device performance degrades. To the best of our knowledge, there are only some models available in literature that estimate the degradation of device performance with excess sodium content; however there is no experimental data in the literature to support the models. From the comparative graphs shown in the above figures 4.14 to 4.20 it is clear that of all the PV parameters are affected because of excess sodium content. As mentioned in chapter 1 the presence of sodium tends to increase the p type conductivity as sodium avoids the formation of neutral defect compound and also reduces the selenium vacancy. It should be noted that CIGS thin film solar cell is diffusion based devices which means that is essential that most of the photons be absorbed within the diffusion length. As the free carrier density increases the edge of the depletion width starts shifting more towards the junction. The shift in depletion region edge means the electrons have to travel a longer distance before they reach the depletion region and are transferred to the n-side by drift. This results in higher probability of the electrons being recombined before they are transferred to the n-side by drift. It should be noted that in case of absorber films prepared by the two step process and having reduced thickness the recombination probability increases further in the two step process large favorable grains grow at the cost of unfavorable grains. Therefore, smaller grains are formed near the substrate and large, columnar grains are formed near the surface. However, when the absorber thickness is reduced, there is not enough material available for the grains to grow into large columnar grains. Therefore it is postulated that for CIGS absorber films prepared by the two step process and having reduced thickness, the excess sodium influences the free

carrier density, thus, affecting the extent of the depletion width in the p-type film. This results in increase in the recombination of the minority carriers causing a corresponding reduction in the current density. The higher conductivity due to more than optimum sodium content can cause tunneling enhanced recombination that can reduce the open circuit voltage. Moreover, another model suggests that there is a possibility of a stable compound $Na_2Se$ being formed. $Na_2Se$ is known to be very conductive thus causing shunt paths and a corresponding reduction in the shunt resistance and open circuit voltage. Based on the device performance of the cells that were prepared with no additional sodium source, it can be concluded that the barrier layer that was used was still not fully effective in reducing the out-diffusion of sodium from the soda lime glass to a negligible level. Therefore, experiments were carried out to optimize the barrier layer thickness in order to minimize the out diffusion of sodium from the soda lime glass. The results for this experiment are discussed in details in the later sections.

### *4.2.3 Best Result for Very Thin (< 1 μm) CIGS Thin Film Solar Cells Prepared in Conventional furnace*

Based on the results for experiments with selenization time and varying NaF thickness it was concluded that the selenization time of 30 minutes with NaF thickness of 30 Å NaF would be the optimum conditions for selenization of very thin CIGS thin film solar cells prepared in conventional furnace. Therefore, cells were completed on absorber which had 30 Å NaF and selenized for 30 minutes at 515 °C. Figure 4.21 shows the current-voltage curve for the best cells as measured at FSEC PV Materials Lab. Highest efficiency of 6.26% was achieved as measured at FSEC PV materials Lab. It should be noted that generally an increase of 2-3% is observed when the same cell is measured at NREL. Table 4.2 shows the PV Parameters for the best device with area of 0.441 $cm^2$. As can be seen from the table diode ideality factor is ~2 which is

generally the case with most thin film solar cells. The short circuit current is lower than the theoretical current density achievable for CIGS thin films solar cells. As mentioned earlier and is known that generally absorbers grown by a two step process generally tend to have smaller grains near the back contact and larger, columnar grains near the surface. In case of thinner absorber films, the evolution of grains into large columnar grains is truncated and the overall grai size remains small. Therefore, the photons are absorbed in the small grain region (which means greater grain boundary density) and so higher possibility of recombination. This could explain the current loss in thinner absorber films. Another factor to consider is that since the gallium is not distributed evenly in the bulk of the film and tends to segregate near the back contact the bandgap is higher near the back as compared to the surface. Therefore, there is possibility of losing the lower energy photons which are absorbed deeper into the bulk of the film. Thus, the lower current density for thinner absorber films as compared to the thicker films with the same bandgap. The open circuit voltage for the best cell was 410 mV which clearly suggests that there is almost no gallium near the surface and that the bandgap near the surface is probably 1.02 eV i.e bandgap of CIS.

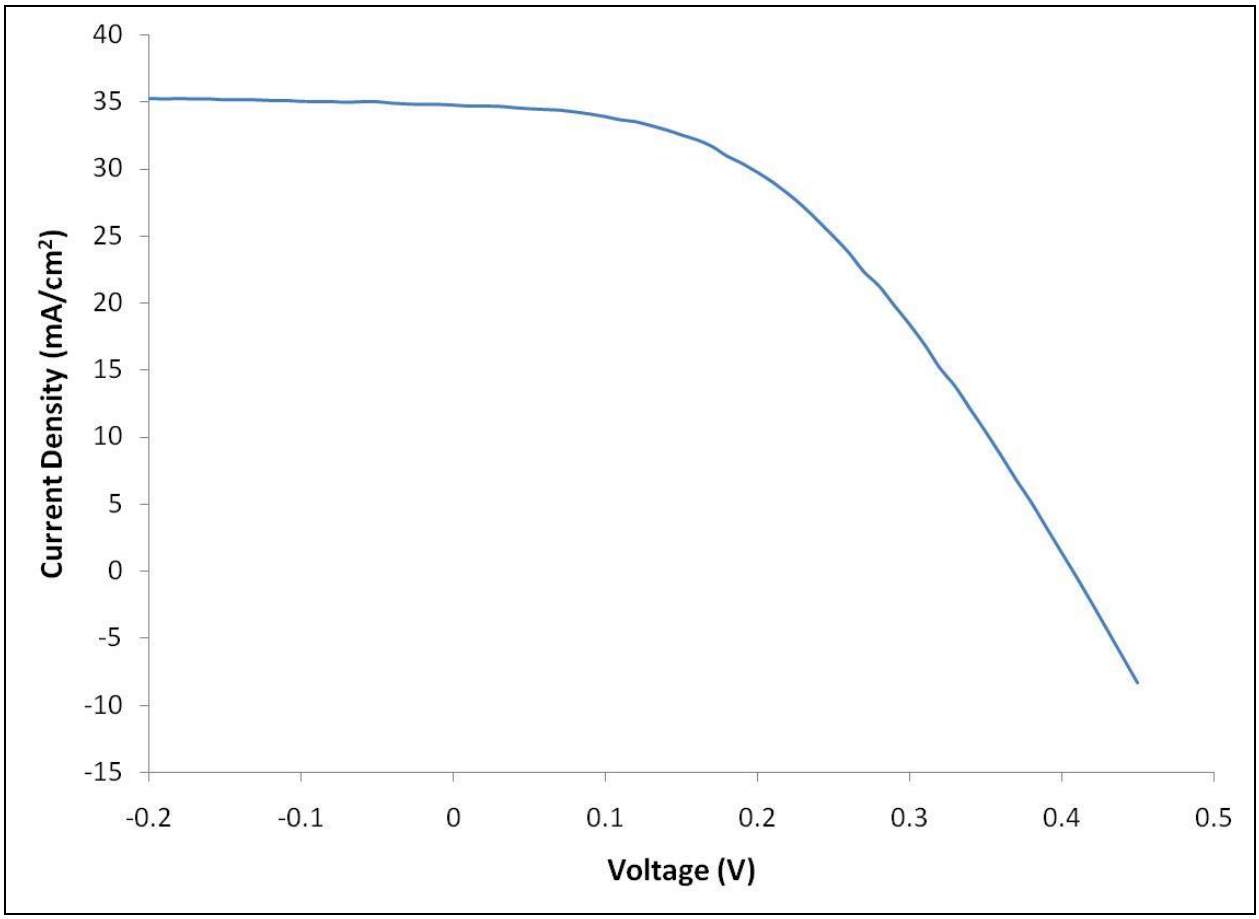


Figure 4.21: I-V Curve of Best Cell prepared in Conventional Furnace

Table 4.2: PV Parameters for the Best Cell for ~1 µm absorber prepared in conventional furnace

| Voc (mV) | Jsc ($mA/cm^2$) | FF (%) | $R_s$ ($\Omega$-$cm^2$) | $R_{sh}$ ($\Omega$-$cm^2$) | A | Jo |
|---|---|---|---|---|---|---|
| 410 | 34.75 | 48 | 3.6 | 319 | ~2 | 1.72E-06 |

## 4.3 Very Thin (< 1 µm) CIGSeS Thin Film Solar Cells Prepared with RTP

For the rapid thermal processing approach, the thickness of the material in the ultra thin absorber is less than half to that used for the regular CIGSS absorber(>2µm). For preparing samples with the RTP approach, experiments were first carried out for varying NaF thickness on CIGS absorbers. Further, selenization and sulfurization of the metallic precursors were carried

out to prepare CIGSeS thin film solar cells. Experiments were carried out to optimize the sulfurization time.

### *4.3.1 Effect of Varying NaF thickness on CIGS thin film solar cells prepared by RTP Approach*

As mentioned in earlier chapters, presence of sodium tends to improve the absorber film properties as well as the device performance. It should be noted that the kinetics of the selenization process in conventional furnace and by the RTP approach is different. Therefore, though the NaF thickness was optimized for very thin films prepared in conventional furnace, it is essential to re-optimize the NaF thickness for samples prepared by the RTP approach. Hence, experiments were carried out to optimize the NaF thickness for CIGS absorbers prepared by the RTP approach. The metallic precursors with appropriate thickness were deposited using DC magnetron sputtering. Elemental selenium was evaporated on the metallic precursors. the thickness of the selenium layer was such that total selenium content was approximately 2 times that required for stochiometric CIGS. All the samples were selenized for 4 minutes at 550 °C. The NaF was deposited by thermal evaporation before the metallic precursor deposition. No NaF was deposited for one of the samples and other two samples had 60 Å and 90 Å NaF deposited on them. The reason for considering higher NaF thickness as compared to those used for samples prepared in conventional furnace is that the total reaction time is significantly lower in the RTP approach. Therefore, it was hypothesized that for optimum amount of sodium to be diffused into the absorber it was essential to provide higher initial concentration.

Figure 4.22 shows the optical microscopy images of the absorber film with varying NaF thickness. As can be seen from the figure the film which had no NaF had lot of features and the feature density reduced as the NaF thickness increased. One of the advantages of sodium is that

it is a very mobile atom which translates into an increase in mobility of all adatoms leading to probable better intermixing of the metallic precursors.

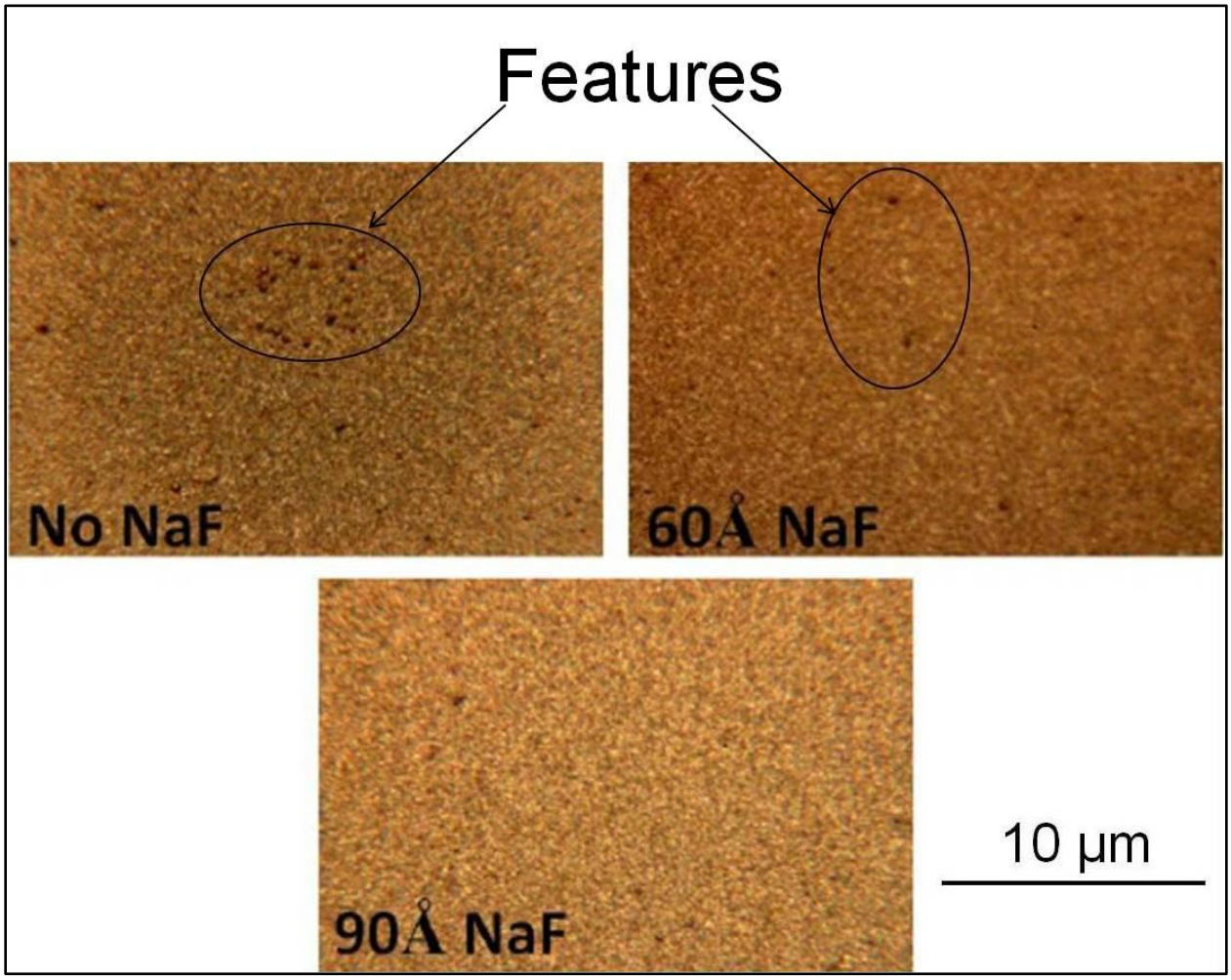


Figure 4.22: Optical Microscopy images at 50X magnification for samples with varying NaF Thickness

Figures 4.23 to 4.25 show the variation of various PV parameters with varying NaF thickness. As can be seen from the figures the device performance improves with increasing NaF thickness. The major improvement in the device performance can be attributed to the improved in the open circuit voltage. The increase in the open circuit voltage can be explained by the higher shunt resistance. On correlating the surface of the absorber film as seen in figure 4.22 and

the device performance, a relationship between film property and the device performance can be established. The feature density reduces as the NaF thickness increases. The presence of features results in poorer surface which means higher interface recombination sites. Moreover, the features make the film more rough and more difficult to be fully covered by CdS and it is possible that the ZnO:Al can come in contact with the absorber film thus forming shunt paths. One of the other things that should be noted is that there is hardly any change in the series resistance which was not the case for samples prepared in conventional furnace. The hypothesis presented here for such a behavior is that probably the selenization time is not optimized and that thicker $MoSe_2$ layer is forming near the back contact. Therefore, the formation of $MoSe_2$ is the dominant mechanism determining the series resistance. The reverse saturation current also reduces by almost by an order of magnitude as the NaF thickness is increased from 0 to 60 Å and can explain the increase in the open circuit voltage. Overall, it can be concluded that the presence of sodium tends to improve the film properties and the corresponding device performance.

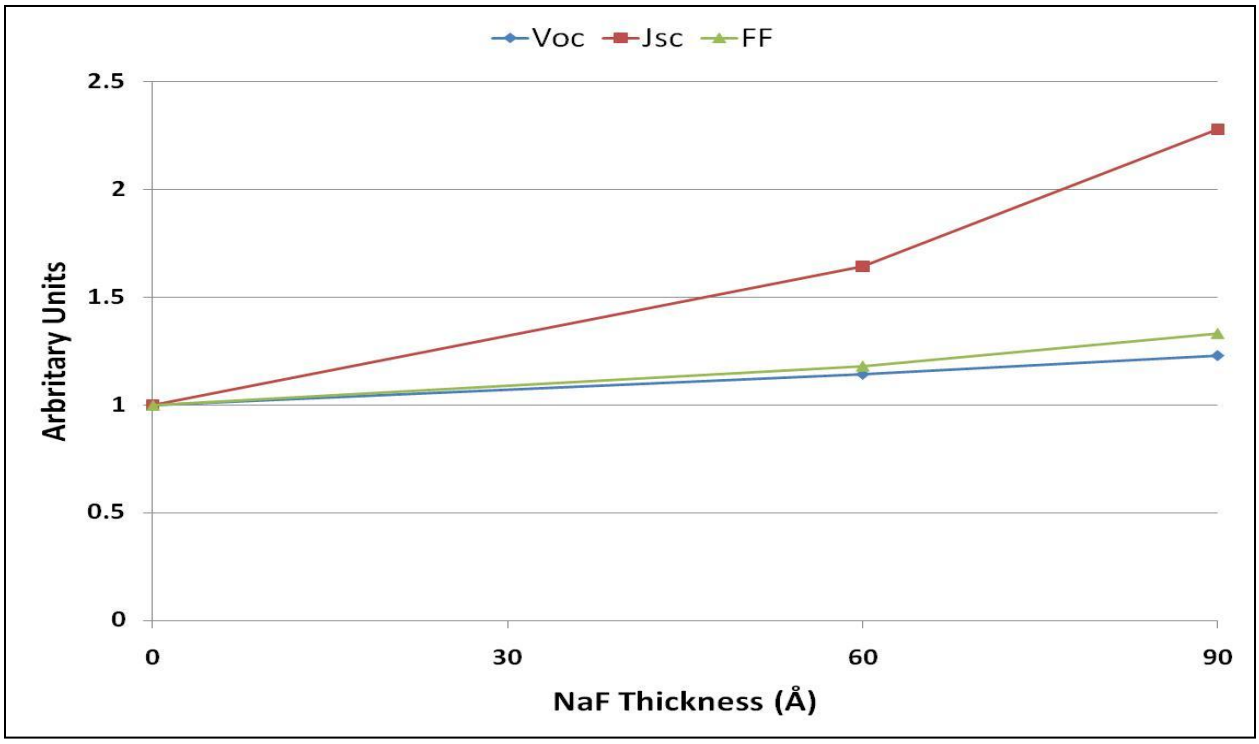


Figure 4.23: Effect of varying NaF thickness on open circuit voltage, short circuit current density and fill factor

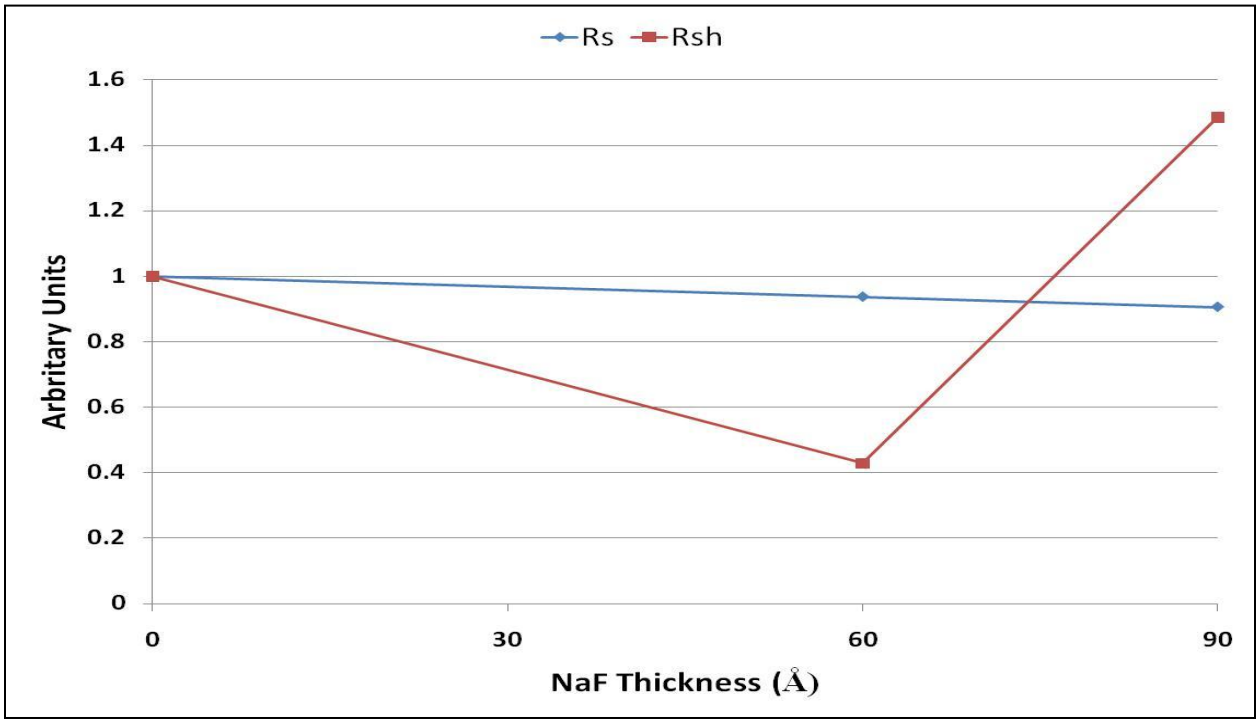


Figure 4.24: Effect of varying NaF thickness on series and shunt resistance

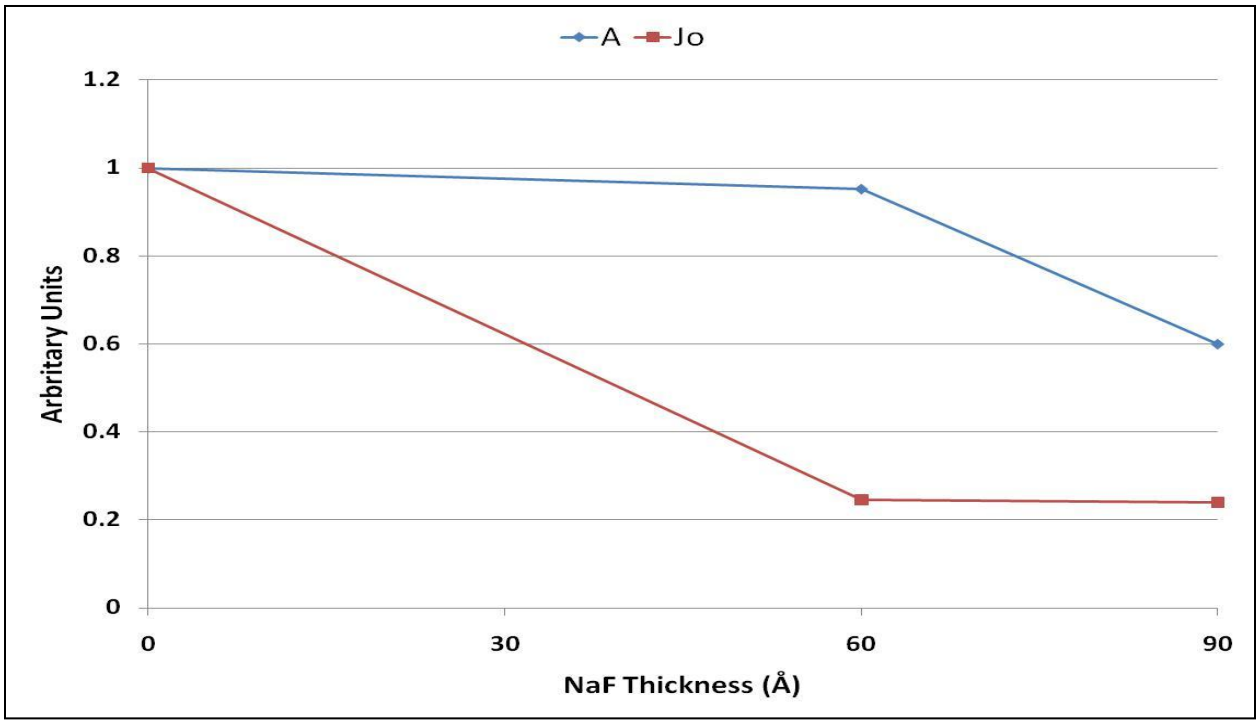


Figure 4.25: Effect of varying NaF thickness on diode ideality factor and reverse saturation current

It is very interesting to note that the optimized NaF thicknesses for absorbers prepared by RTP approach and in the conventional furnace are different. This behavior can be explained by the fact that the total reaction time of the two processes is significantly different. Moreover, the substrate used for the experiments has only a thin barrier layer so some sodium from the soda lime glass is expected to diffuse into the absorber film. Therefore, in case of RTP due to the very low deposition time hardly any sodium can diffuse from the soda lime glass which can explain the requirement higher NaF thickness in case of RTP as compared to conventional furnace. Therefore, one of the significant contributions from the above sets of experiments is that it has been proven that it is essential to optimize the sodium precursor thickness based on the process parameters such as deposition time and temperature, in addition to the thickness of absorber films.

### *4.3.2 Effect of Sulfurization time on CIGSeS thin film solar cells*

In the two-step process, gallium tends to segregate to the back and thus does not aid in increasing the bandgap near the surface. To achieve higher open circuit voltages, it is essential to have an absorber film with higher bandgap near the junction. Therefore, sulfurization of the partially selenized films was carried out to improve the device performance. From our earlier results, it was known that complete selenization of the metallic precursors was carried out in 4 minutes. Therefore, for the films that were going to be sulfurized the selenization time was reduced to 2 minutes. The sulfurization was carried out using $H_2S$ gas at 550 °C with $H_2S$ partial pressure of 15 mTorr. The NaF thickness was selected empirically to be 60 Å for this set of experiments.

The diffusivity of sulfur is very high. Therefore, is necessary to control the sulfur profile in the bulk of the film. The bandgap in the bulk of the absorber film increases if sulfur gets diffused into the bulk of the material. This increase in bandgap results in the reduction in the current produced by the solar cells since lower number of photons are absorbed in higher bandgap materials. Therefore, experiments were carried out to optimize the sulfurization time.

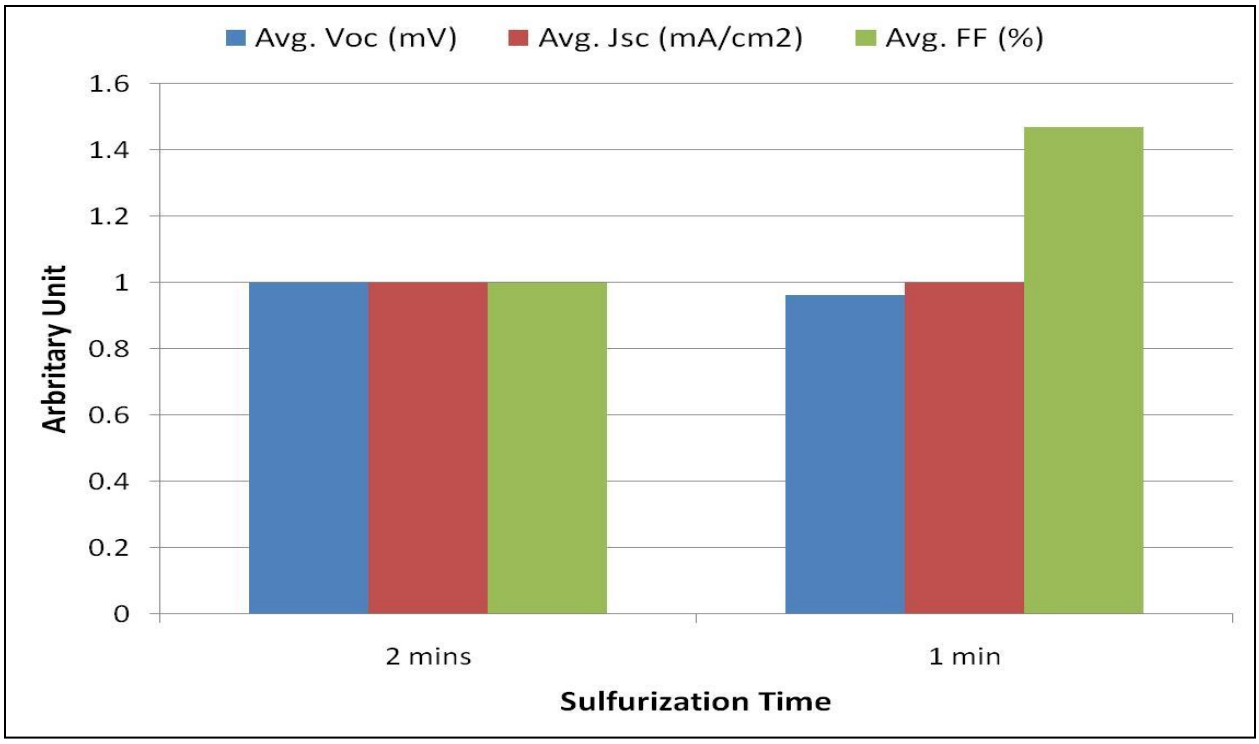


Figure 4.26: Effect of sulfurization time on open circuit voltage, short circuit current density and fill factor

Figures 4.26 to 4.28 show the variation in various PV parameters with respect to sulfurization time. As can be seen the improvement in device performance with reducing sulfurization time can be explained by improving fill factor. The shunt resistance increases significantly with reducing sulfurization time. Moreover, the reverse saturation current reduces by almost an order of magnitude by reducing the sulfurization time.

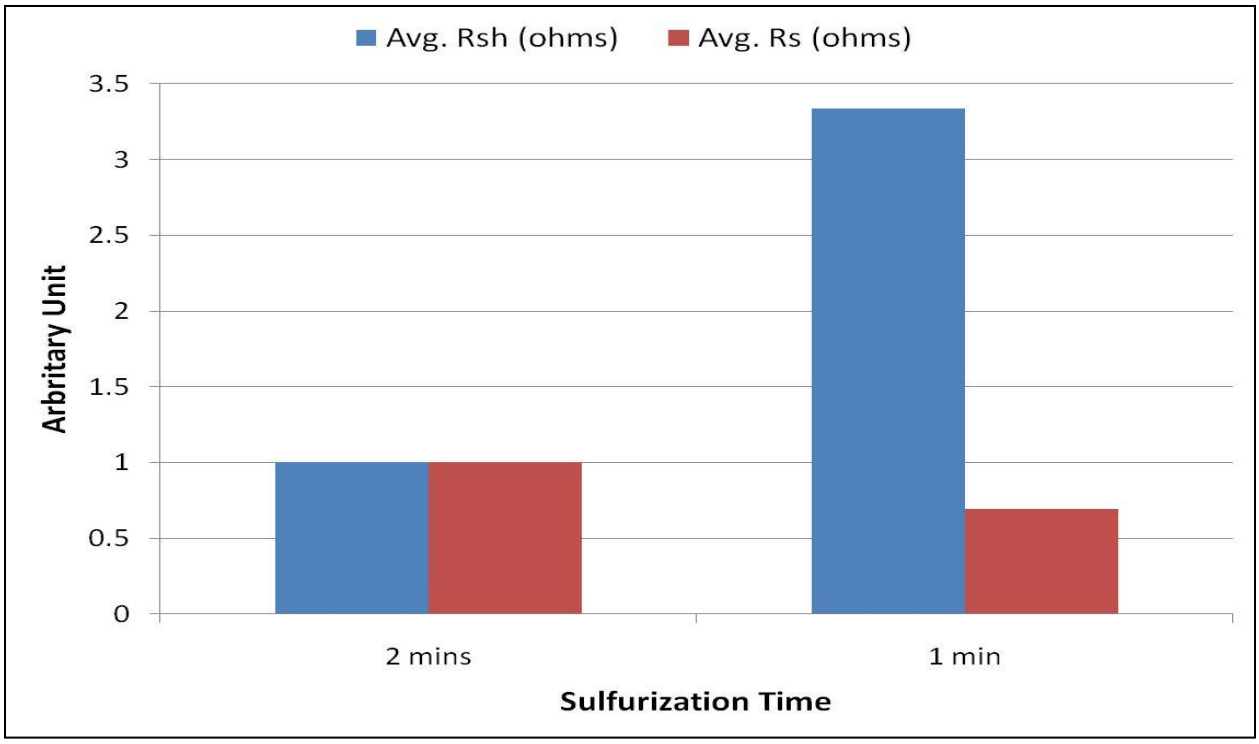


Figure 4.27: Effect of sulfurization time on series and shunt resistance

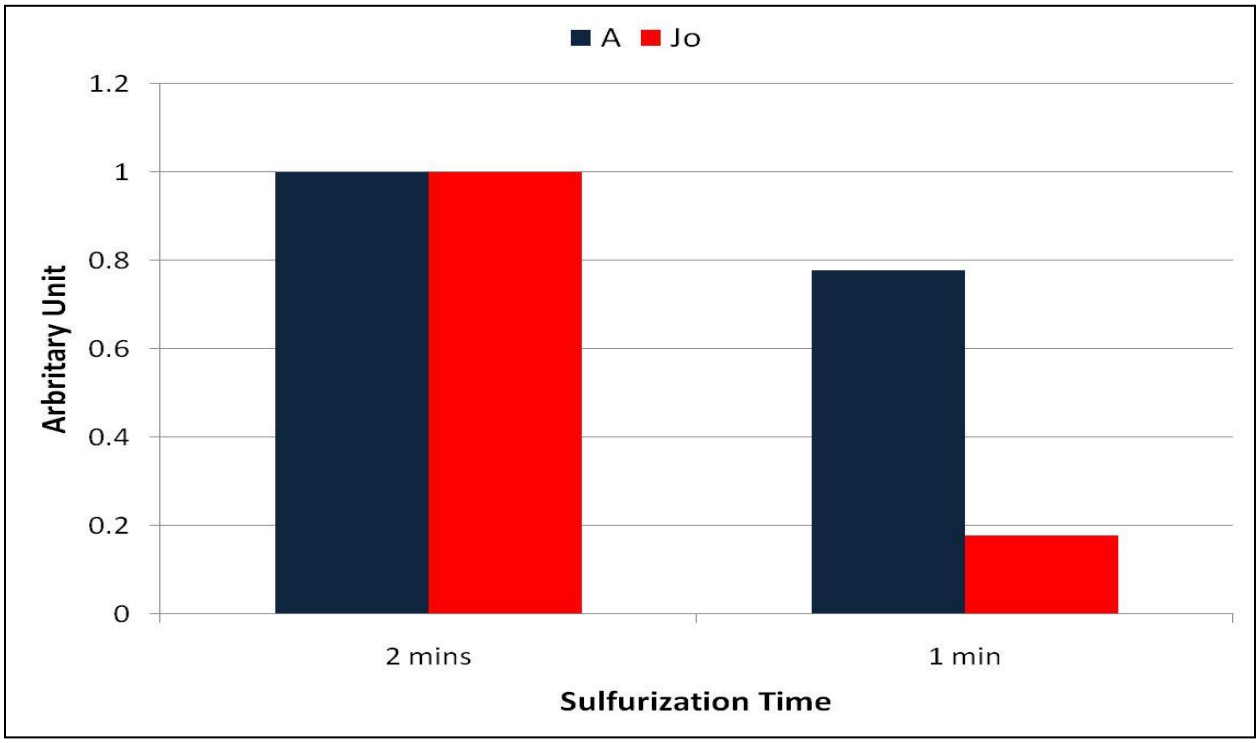


Figure 4.28: Effect of sulfurization time on diode ideality factor and reverse saturation current

As can be seen from the graph the improvement in the values of the fill factor, shunt resistance and the reverse saturation current is not reflected for open circuit voltages. This can be explained that the device prepared by sulfurizing for 2 minutes the series resistance was very high to the point that it moved the open circuit point and therefore, the open circuit voltage obtained from the I-V curve is not the correct value.

### *4.3.3 Best Result for Very Thin (< 1 µm) CIGSeS Thin Film Solar Cells Prepared by RTP Approach*

Based on the experiments carried out with varying NaF thickness and the sulfurization time, it was concluded that NaF thickness of 90 Å and sulfurization time of 1 minute was optimum. Therefore, samples were prepared with NaF thickness of 90 Å. The selenization time was 2 minutes and the sulfurization time was set at 1 minute. The cells were completed on the absorber and current voltage measurements were carried out using an in-house designed setup. Figure s.s shows the current-voltage characteristics for the best cells as measured at FSEC Thin Film Lab. Highest efficiency of 6.58% was achieved as measured at FSEC Thin Film Lab. It should be noted that generally an increase of 2-3% is observed when the same cell is measured at NREL. Table 4.3 shows the PV parameters for the best device with area of 0.441 $cm^2$.

The diode ideality factor is ~2.2 which is comparable to the diode ideality factor generally achieved in thin film solar cells. The reverse saturation current is of the order of $10^{-4}$ which is slightly on the higher side. This also could explain the slightly lower voltage obtained in this device. As expected the current density is lower due to the higher bandgap of CIGSeS thin film solar cells.

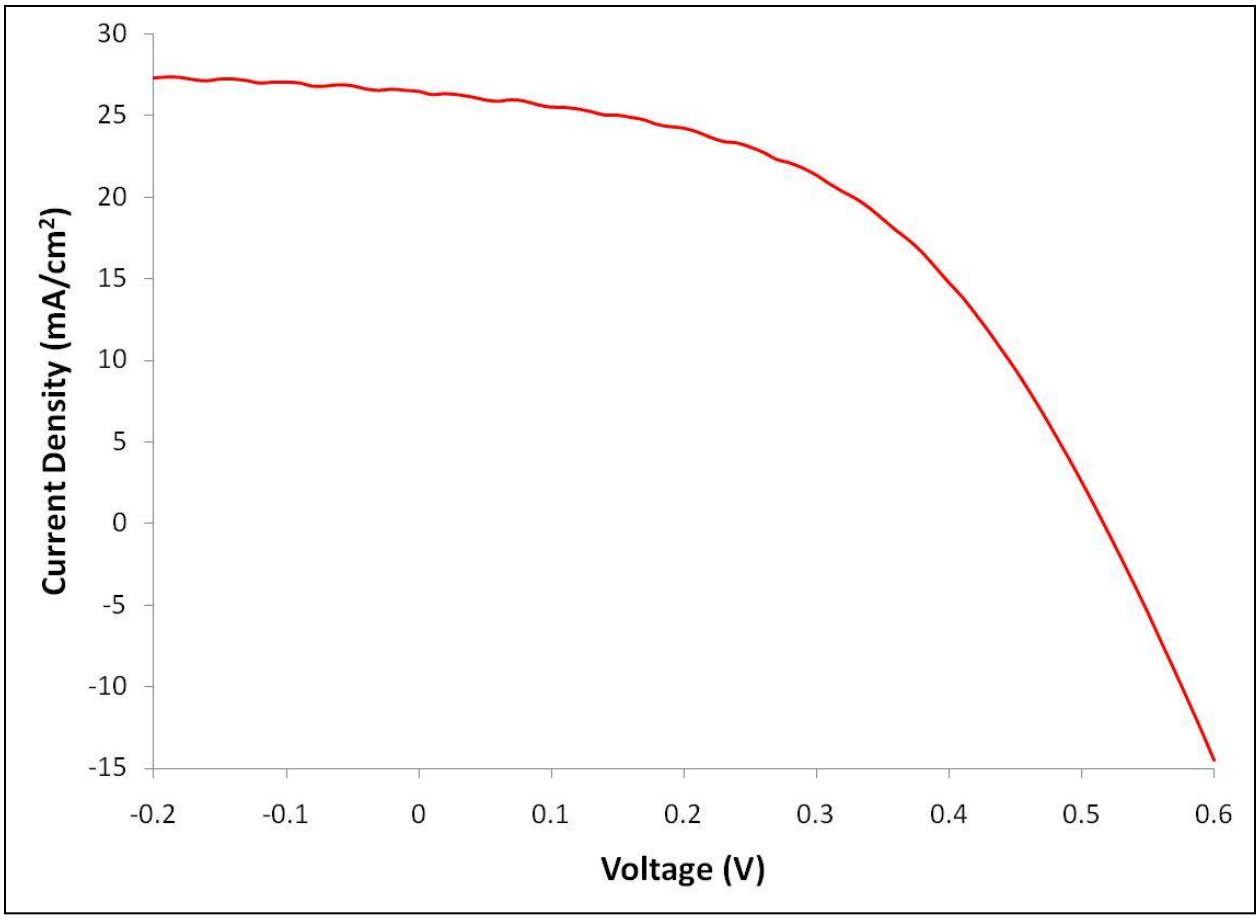


Figure 4.29: I-V Curve of Best Cell prepared by RTP

Table 4.3: PV Parameters for the Best Cell for ~1 µm absorber prepared by RTP

| Voc (mV) | Jsc ($mA/cm^2$) | FF (%) | $R_s$ ($\Omega$-$cm^2$) | $R_{sh}$ ($\Omega$-$cm^2$) | A | Jo |
|---|---|---|---|---|---|---|
| 520 | 26 | 47 | 3.9 | 261 | ~2.2 | 2.88E-04 |

## 4.4 Comparison of Best Cells prepared by RTP Approach and in Conventional Furnace

The highest efficiency achieved by the two techniques of selenization in the conventional furnace and seleniztion/sulfurization by RTP are comparable. However, there is a significant difference in the other PV parameters for the two types of devices. The voltages obtained for the CIGSeS solar cells prepared by RTP, the voltage are higher and the currents are lower than those obtained for CIGS devices prepared in the conventional furnace. The higher voltages and lower

currents for the CIGSeS devices is apparent because of the higher bandgap of the absorber film. The series resistance is almost comparable for both types of devices. However, the shunt resistance for the CIGS devices is higher than those for the CIGSeS devices. The higher shunt resistance for the devices prepared in the conventional furnace can be explained by the longer reaction time as compared to RTP process. Longer and optimized reaction time results in a better quality of film, thus, improving the shunt resistance. However, it is important to note that the total reaction time for RTP is almost $1/10^{th}$ of the reaction time in conventional furnace and the reduction is shunt resistance is not very significant. The reverse saturation current for the devices prepared by RTP is almost two orders of magnitude higher than that for devices prepared in conventional furnace.

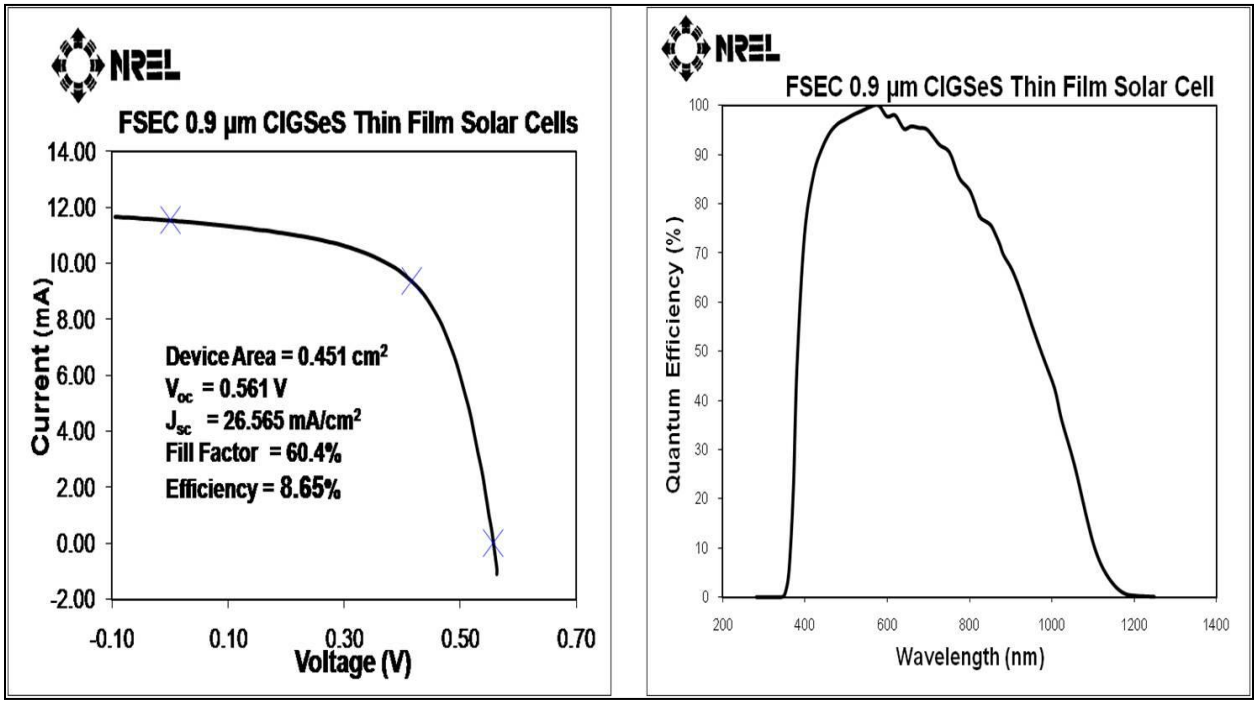


Figure 4.30: I-V and QE Curve for 0.9 µm thick absorber film as measured at NREL

Figure 4.30 shows the current-voltage characteristics and the quantum efficiency (QE) curve of 0.9 µm CIGSeS thin film solar cell as measured at NREL. As can be seen the efficiency

measured at NREL is almost 2.-3 % higher as compared to that measured in the in-house setup. The open circuit voltage increased by about 40 mV and the fill factor jumped by about 12%. As can be seen from the difference in PV parameters, the issues with the in-house I-V setup is improper contacts. New contact probes have been ordered to fix this problem. The quantum efficiency curve suggests that the bandgap of the absorber is approximately 1.12 eV. Figure 4.31 shows QE curve for a 0.9 µm device with the theoretical QE curve for a CIGS absorber. It can be clearly seen that the current loss is mainly occurring at the higher wavelengths with some losses in the bulk of the film. As mentioned earlier, for the thinner absorbers the photons are absorbed in the smaller grain region which could lead to higher recombination which would explain the losses in the bulk of the film. The lower energy or higher wavelength photons are generally absorbed deeper into the bulk of the film. Therefore, it can be concluded that the current loss is due to the recombination near the back contact.

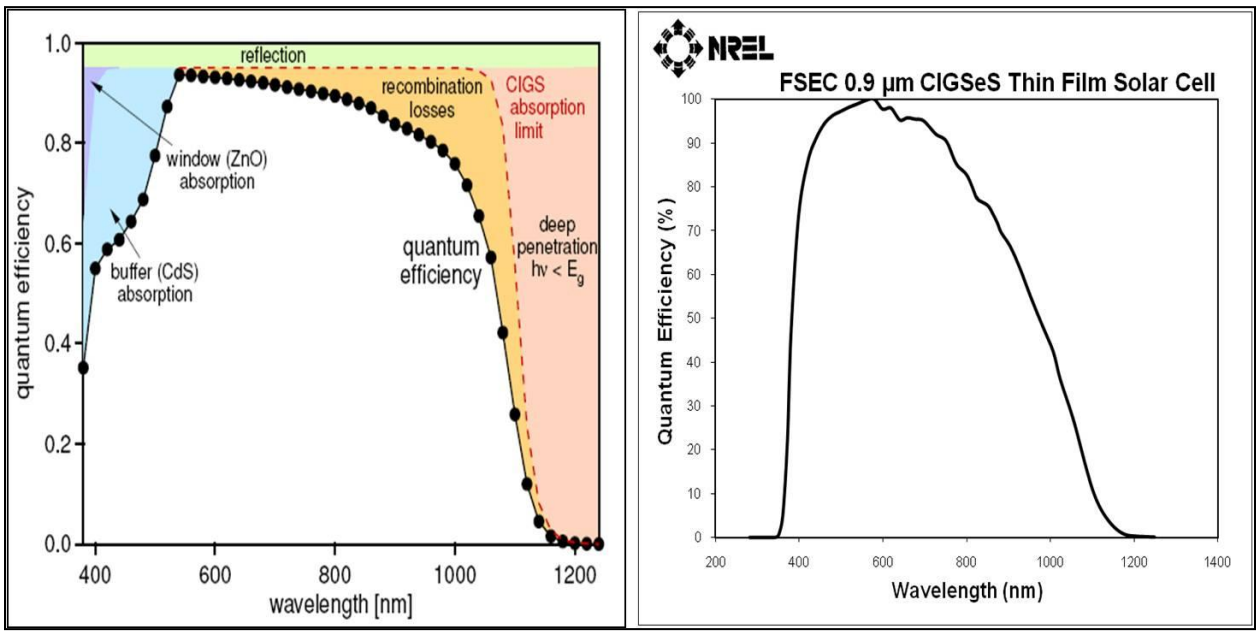


Figure 4.31: Comparison of Theoretical and Actual QE curve

The effort to optimize the processing parameters for very thin (<1µm) CIGS and CIGSeS thin film solar cell resulted in the highest certified efficiency of 8.65% as measured at NREL. The highest certified efficiency achieved for a thick (~2.5 µm) CIGSeS thin film solace cell prepared by the same two step process is 13.73%. Therefore, if we consider the device performance as function of absorber thickness we get that the efficiency for very thin (<1µm) CIGS and CIGSeS thin film solar cell is 9.61%/µm and that for a thick (~2.5 µm) CIGSeS thin film solace cell is 5.49%/µm. Thus a gain of 3-4 %/µm is achieved from the work. Hence, it is safe to infer that reducing the absorber thickness will result in reduction in cost because of lesser material usage without significantly affecting the device output.

### 4.5 Effect of Silicon Nitride Barrier Layer

Sodalime glass (SLG) is the most commonly used substrate in fabrication of CIGS thin film solar cells. Small amount of sodium is known to have a favorable effect on device performance; however, excess amount degrades device performance. The sodium out-diffusion from the SLG is uncontrollable. To obtain the advantages of sodium without losing process control, an alkali barrier layer such as $Si_xN_y$ is deposited before molybdenum layer followed by sodium precursor. It is essential to optimize thickness of the barrier layer in terms of the ability to effectively avoid the diffusion of sodium from the SLG into the absorber as well as in terms of the adhesion properties of the alkali barrier layer with the SLG substrate. CIGS thin film solar cells were prepared for various thickness of the silicon nitride barrier layer. The effect of the varied barrier layer thickness was studied and based on the results the optimized barrier layer thickness was determined. Reactive RF magnetron sputtering was used for the deposition of silicon nitride layer.

Initial experiments involved the determination of the deposition rate and verification of formation of the silicon nitride layer. The deposition rate was determined by carrying out the thickness calibration using a profilometer and the silicon nitride formation was verified by energy dispersive spectroscopy (EDS) mapping in transmission electron microscopy (TEM). Once the deposition rate for silicon nitride was determined, samples were prepared with 0 Å, 400 Å, 800 Å and 1200 Å silicon nitride. Four layered molybdenum was deposited on each of the sample. In our setup, the substrate moves linearly over the sputtering target and the thickness of the deposited film is determined by the speed at which the substrate moves. It can be safely assumed that an inverse linear relationship exists between the deposited film thickness and the speed of substrate movement. Based on the earlier experiments to determine the deposition rate of the silicon nitride the speed to substrate movement was altered to obtain the various thickness of silicon nitride layer.

As mentioned earlier, absorber layer was deposited and the device was completed. The absorber film was prepared at elevated temperatures of ~500 C and it was interesting to determine if the increase in the silicon nitride thickness was having any effect on the adhesion of the device to the sodalime glass substrate. It was observed that for absorber films grown on samples with higher silicon nitride thickness, the films were peeling off from the edges. This indicated that the adhesion of the film reduced as the silicon nitride thickness increased. However, it should be noted that during the deposition of the silicon nitride layer and molybdenum back contact layer the substrate was not kept in overnight vacuum which is the general practice during the deposition of various layers. The lack of overnight vacuum could lead to presence of moisture and that could lead to change in the stress buildup in the silicon nitride

film leading to loss of adhesion and it is essential to carry out some more experiments to confirm the reason for loss of adhesion with increase in the silicon nitride thickness.

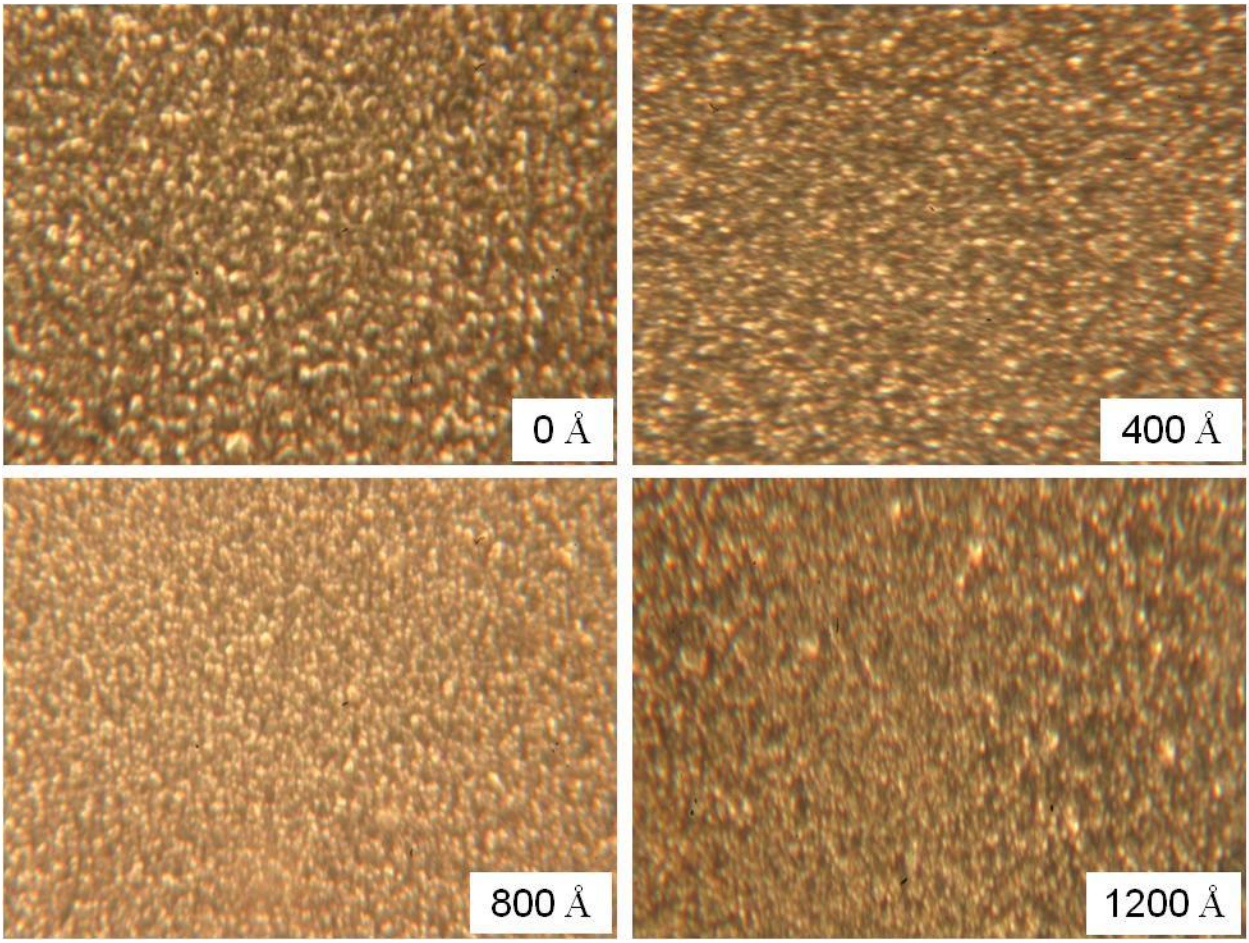


Figure 4.32: Optical Image of each sample at 500X magnification

Figure 4.32 shows the optical image of each sample at 500X magnification and figure 4.33 shows the SEM image for each sample at 10000X magnification. The hypothesis behind this experiment is that as the thickness of the alkali barrier layer increases the probability of sodium diffusion into the absorber film reduces. As can be seen from figures 4.32 and 4.33 the morphology of the absorber for samples with silicon nitride thickness up to 800 Å is similar and when the thickness is increased beyond 800 Å the grain size reduces. The surface morphology

suggests that the diffusion of sodium becomes negligible at and above sodium nitride barrier layer thickness of 800 Å.

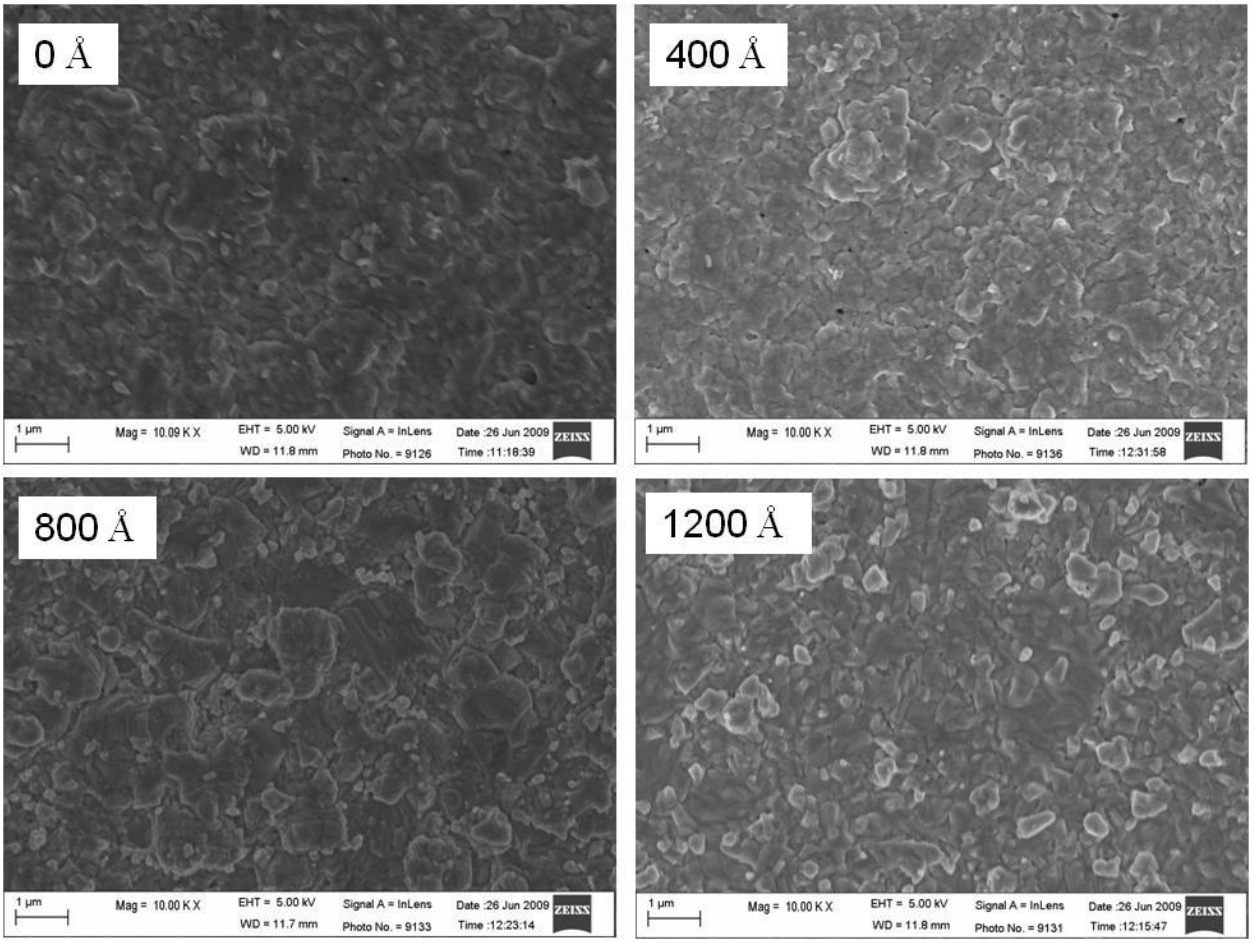


Figure 4.33: SEM image of each sample at 10,000X magnification

The I-V measurements were carried out using an in-house built I-V setup and are not certified. Generally, a significant decrease in the series resistance and increase in the current values has been observed when the same sample is measured at National Renewable Energy Laboratory (NREL) as compared to when measured in the in-house built I-V setup. It should be noted that small area CIGSeS thin film solar cells with NREL certified efficiencies of 9-10% are routinely prepared at FSEC PV Materials Lab. Since the device performance is not certified for

comparison purposes a normalized photovoltaic parameters have been considered. Figures 4.34 - 4.37 show the comparison of various photovoltaic parameters such as open circuit voltage ($V_{oc}$), short circuit current density ($J_{sc}$), fill factor (FF) and series and shunt resistances respectively.

It was observed that the device performance deteriorated as the thickness of the silicon nitride thickness was increased. The open circuit voltage was not reduced significantly however there was a significant drop in short circuit density. The significant drop in the current density can be explained by the significant rise in the series resistance. Presence of sodium is known to improve the p-type conductivity by reducing the compensating donor defects. As the silicon nitride thickness increases the amount of sodium diffusing from the SLG to the absorber layer reduces. The increase in the series resistance with increase in the silicon nitride thickness can be related to absence of sodium and corresponding increase in the donor defect density. Another explanation for the increase in series resistance can be increase in the thickness of the $MoSe_2$ layer. In the presence of sodium selenium incorporation into the CIGS film is improved. Therefore, with the increasing silicon nitride thickness and the corresponding reduction in available sodium, it is possible that higher amount of selenium reacts with the molybdenum back contact forming a thicker $MoSe_2$ layer. This could also explain the peeling of the CIGS film at higher silicon nitride thicknesses. It can be seen in figure 10 that there is an initial drop in the shunt resistance with increase in the silicon nitride thickness, however, the shunt resistance does not reduce with further increase in the silicon nitride thickness. The initial drop in the open circuit voltage can be explained by the drop in the shunt resistance.

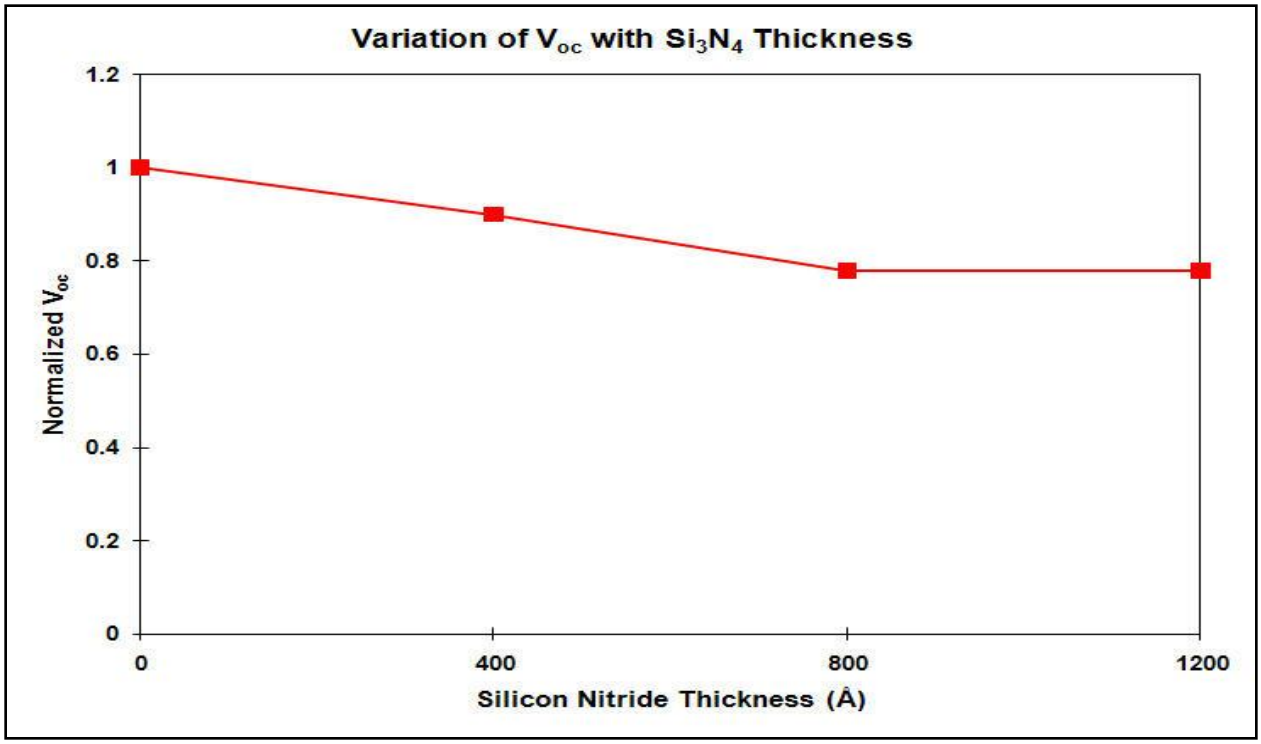


Figure 4.34: Variation of Open Circuit voltage with silicon nitride thickness

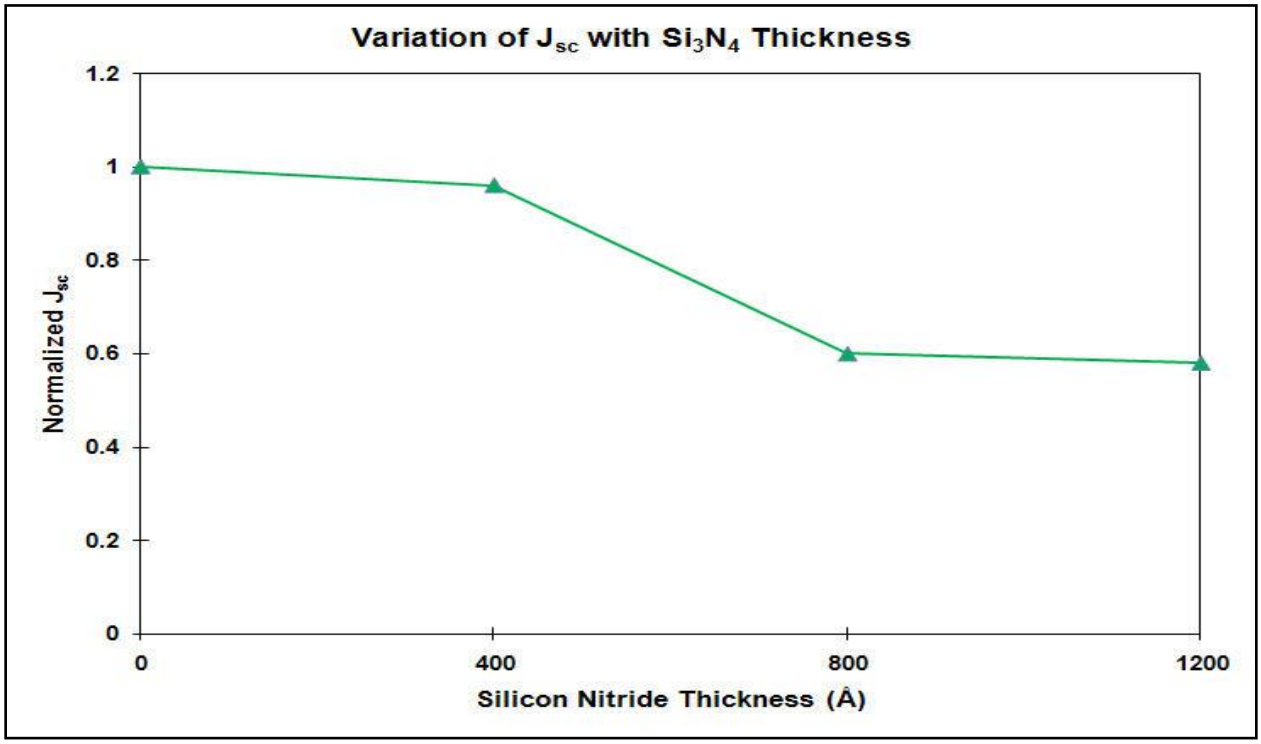


Figure 4.35: Variation of Short Circuit current density with silicon nitride thickness

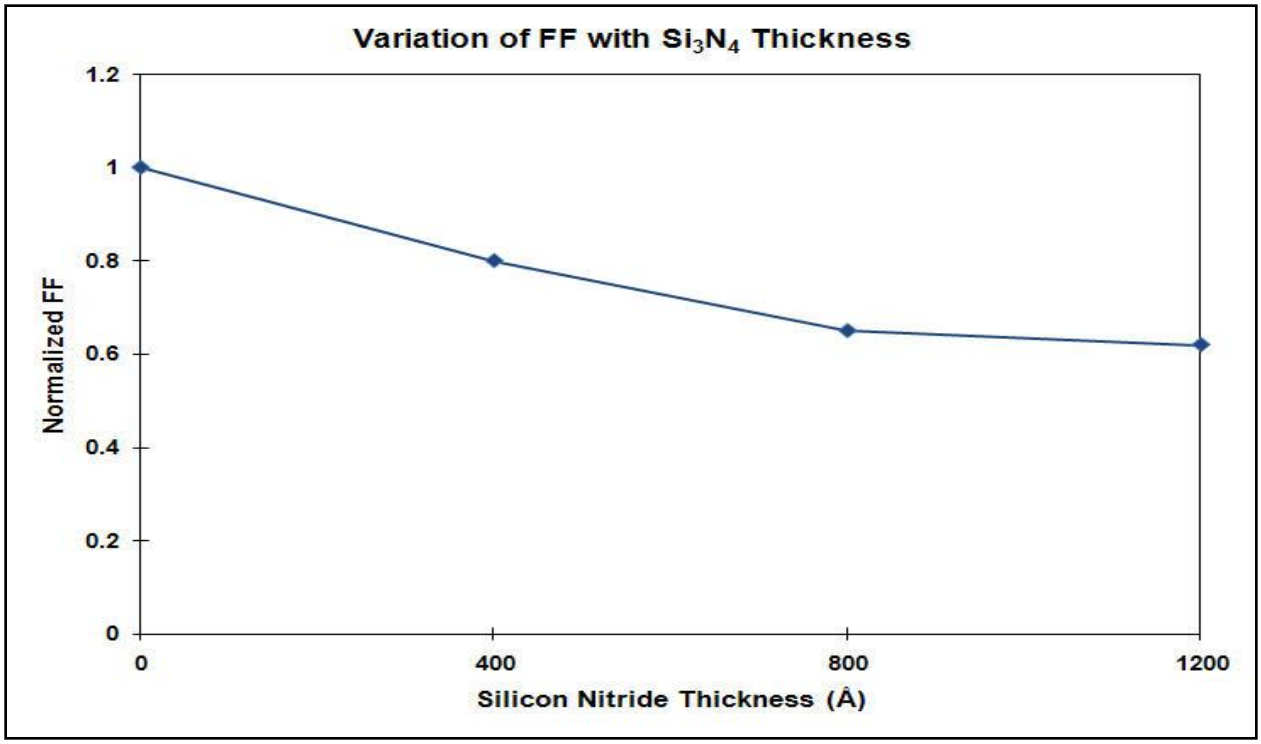


Figure 4.36: Variation of fill factor with silicon nitride thickness

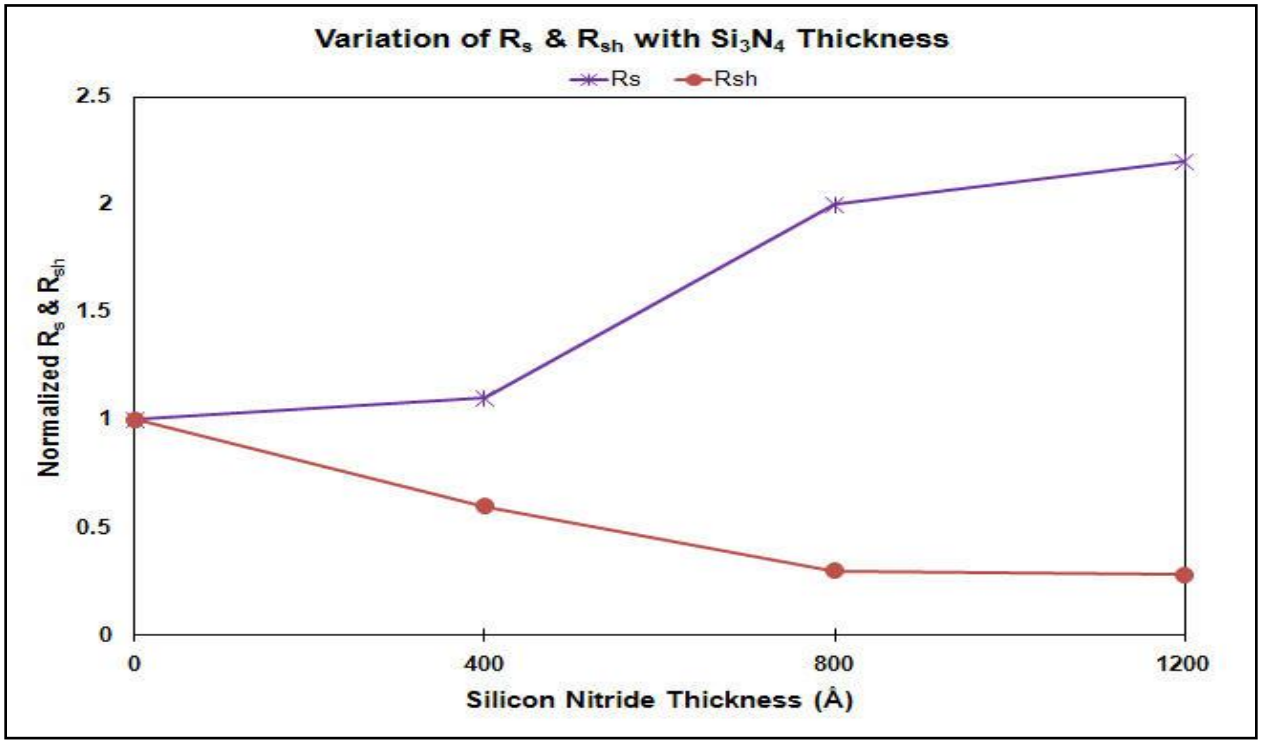


Figure 4.37: Variation of series and shunt resistance with silicon nitride thickness

An alkali barrier layer of silicon nitride was successfully deposited using reactive RF sputtering from silicon target in $Ar+N_2$ ambient. The deposition rate for the silicon nitride layer was determined and samples with various thickness of silicon nitride were prepared. CIGSeS thin film solar cells were deposited on these samples and the I-V measurements were carried out. As expected the photovoltaic parameters deteriorated as the silicon nitride thickness increased. The open circuit voltage did not decrease significantly; however, the short circuit current density decreased to half for the sample with 800 Å thick silicon nitride barrier layer. The series resistance increased drastically as the silicon nitride thickness increased with a corresponding drop in the fill factor of the device. The shunt resistance dropped with the initial increase in the silicon nitride barrier layer thickness and later did not change much with further increase in thickness. From the preliminary results it can be concluded that 800 Å thick silicon nitride barrier layer is adequate in effectively blocking the diffusion of sodium from the sodalime glass substrate to the absorber film.

### 4.6 Effect of working distance on properties of sputtered Mo films

The properties of sputtered films such as resistivity, residual stress are dependent on the sputtering process parameters of sputtering power, working gas pressure and the working distance (distance between the substrate and the target). Earlier experiments were carried out at FSEC to understand the effect of working gas pressure and sputtering power on the molybdenum film properties. The working distance was kept constant during these experiments. It is essential to understand the effect of working distance on the molybdenum film properties. Therefore, same set of working gas pressure and sputtering power were experimented with another working distance to understand the effect of working distance on the film properties. In the earlier work

the working distance was maintained at approximately 9 cm and for the new set of experiments the working distance was adjusted to approximately 6.5 cm. It should be noted that with the change in the working distance the condition of the discharge plasma changes resulting in the change in the current and voltage characteristics of the plasma.

Thin, narrow glass strips were procured for the experiments to measure the stress induced by the molybdenum films. Bend analysis technique was used to calculate the residual stress on the molybdenum films deposited at various processing conditions. The radius of curvature is calculated for the bent substrate and the residual stress is calculated using Stoney's equation which is given by;

$$\sigma_i = \frac{E_s h_s^2}{6(1-\upsilon)h_c}\left(\frac{1}{R} - \frac{1}{R_0}\right)$$

Where $E_s$ is the Young's modulus of the strip, $h_s$ is the thickness of the glass strip, $h_c$ is the film thickness, $\upsilon$ is Poisson's ratio of the glass strip, R and $R_0$ are the radii of the curvature of the strip or the film after and before deposition respectively. Figure 4.37 shows the bending occurring on the glass strips due to the stress developed by the sputtered molybdenum films.

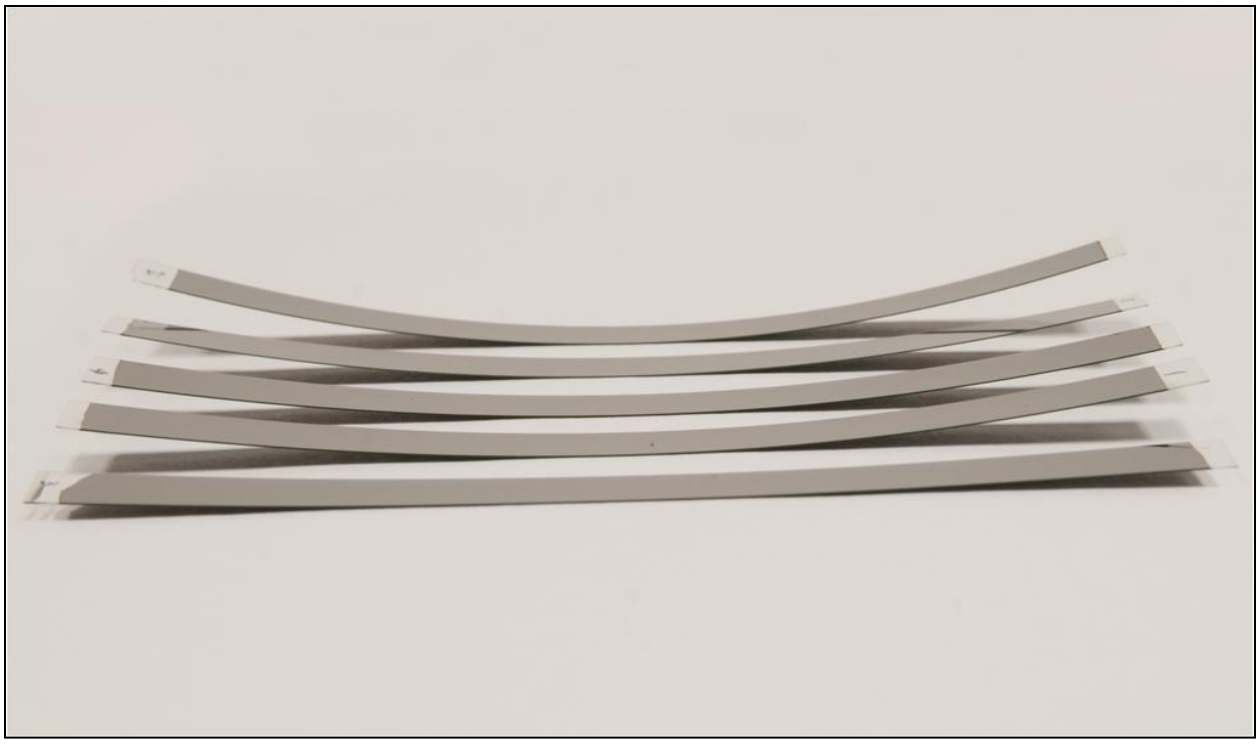

Figure 4.38: Bending of glass strips with molybdenum films deposited at various processing conditions

Figures 4.39 shows the variation in residual stress on the films deposited at working gas pressure of 1 mTorr while varying the sputtering power. Figure 4.40 shows the variation in residual stress on the films deposited at varying working gas pressure while keeping sputtering power constant at 200 W. At lower sputtering power of 200 W tensile stresses exist on the films. At higher sputtering power of 275 W some compressive stresses are exerted by the molybdenum film.

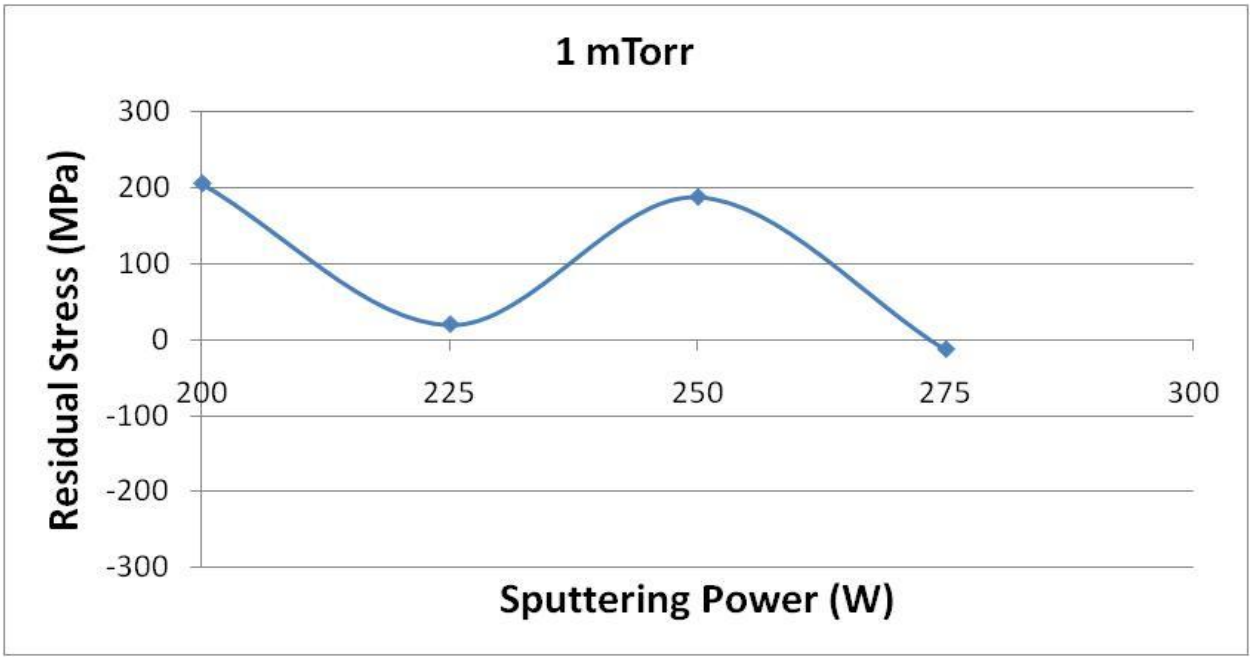


Figure 4.39: Variation of Residual Stress with varying sputtering power

Variation of residual stress with varying working gas pressure suggests a U shaped curve where the tensile stress maximizes at 1 mTorr and then the tensile stress reduces as the working pressure is increased. Beyond 3 mTorr the residual stress crosses into the compressive stress regime. As compared to earlier work, at working distance of 6.5 cm the dependence of residual stress on the processing conditions is completely different. As mentioned earlier, the properties of the plasma change with changing working distance and it was found out that the discharge voltage required to achieve same sputtering conditions of power and pressure for working distance of 6.5 cm was higher as compared to that required for working distance of 9 cm. This higher discharge voltage results in higher kinetic energy of the sputtered atoms as well as the neutralized argon atoms.

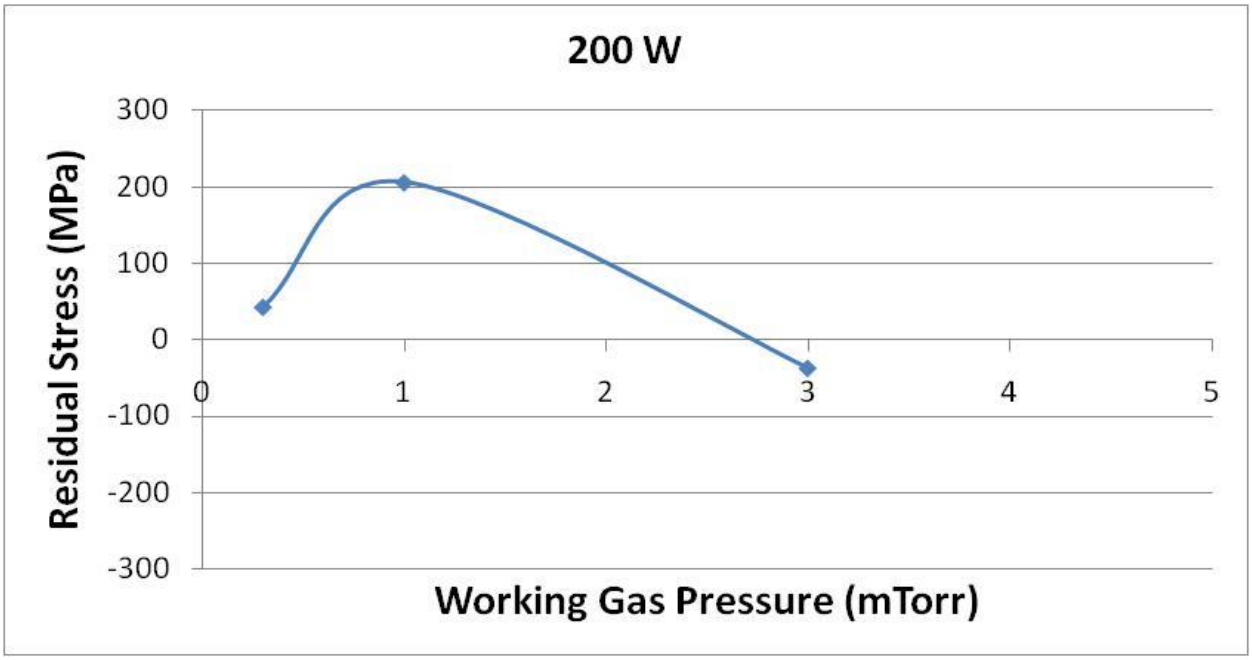


Figure 4.40: Variation of Residual Stress with varying working gas pressure

Four point probe technique was used to measure the sheet resistance of the films and the resistivity of the films was calculated. Figures 4.41 and 4.42 show the variation of resistivity with varying sputtering power and working gas pressure, respectively. The variation in the resistivity value of the molybdenum films with varying process conditions is not large. The resistivity increases with increasing gas pressure because as the pressure increases the scattering of sputtered atom and the neutralized argon atoms. Therefore, the incident kinetic energy of the sputtered atoms and the neutralized argon atoms reduces which can lead to a slightly open structure causing an increase in resistivity.

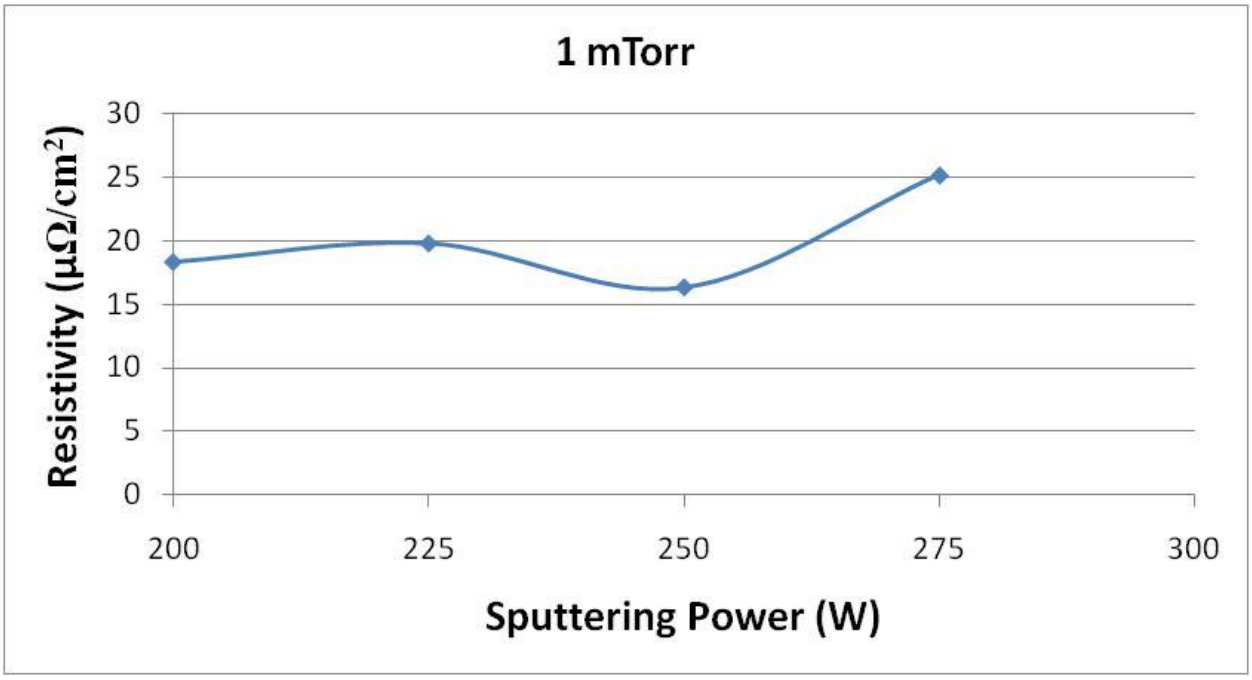


Figure 4.41: Variation of Resistivity with varying sputtering power

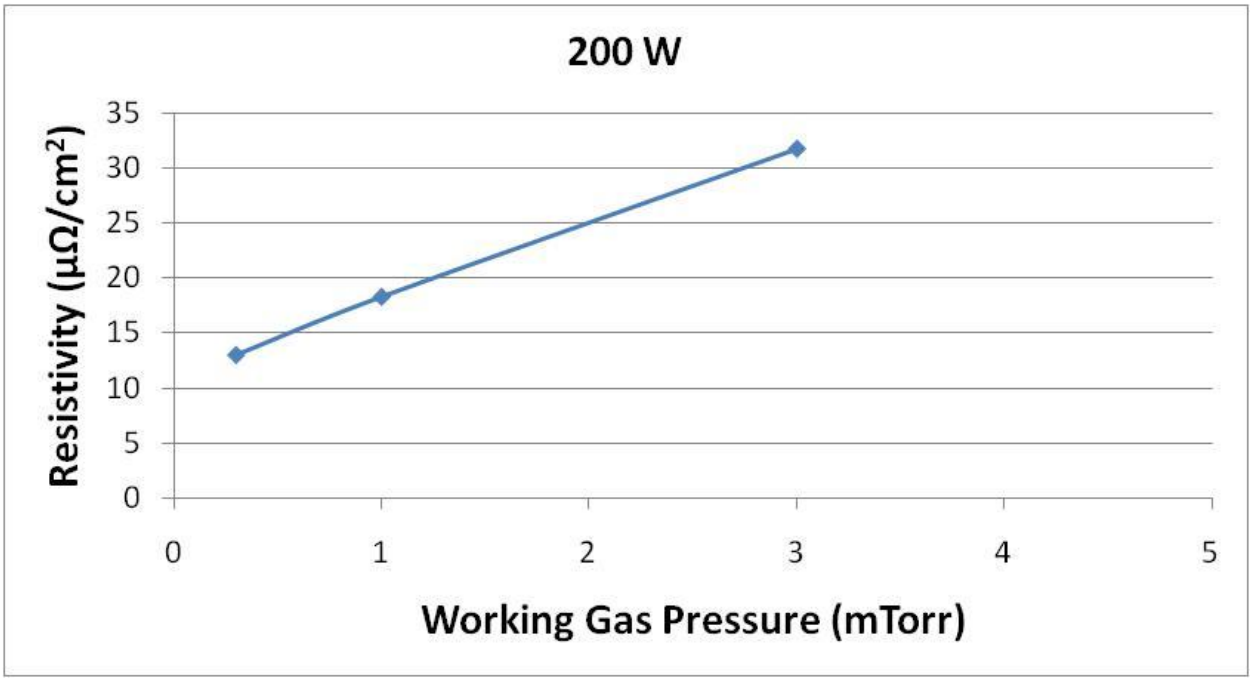


Figure 4.42: Variation of Resistivity with varying working gas pressure

# CHAPTER 5 CONCLUSION AND FUTURE WORK

The primary goal of this research was to achieve comparable efficiencies for very thin absorber films. To optimize the process parameters for the very thin absorber films, it was essential to understand the effect of processing parameters such as selenization time-temperature profile, amount of NaF thickness on the absorber film properties as well as the device properties. Experiments were carried out to understand the effect of annealing at lower temperatures. The metallic precursors were annealed in nitrogen ambient. It was found that phase transformation occurs and that it is beneficial towards the formation of an improved absorber film. Based on the study the standard process was modified to achieve absorber films that were almost feature free. The selenization time was varied to understand the effect of selenization time on device performance and to optimize the selenization time based on the results of this experiment. It was found that the selenization time had direct effect on the reverse saturation current and correspondingly the open circuit voltage. As the selenization time was reduced the reverse saturation current reduced thus giving higher voltages. Based on this experiment, it was concluded that 30 minutes is the optimal selenization time for very thin (<1 μm) absorber films. The advantages of sodium during absorber growth has been proven from the earlier work carried out by our group as well as by other groups. There are also several models explaining the advantages of optimum amount of sodium during the absorber growth. Moreover, there are several other models which suggest that excess sodium can cause degradation of device performance. From the work carried out earlier at FSEC the optimum amount of NaF that was needed for device quality films is known. However, it was essential to study if the optimum amount of sodium was dependant on the reaction process parameters. Experiments with varying

NaF thickness were successfully carried out for thinner (<1 μm) absorber films prepared in the conventional furnace. The NaF thickness was varied from 0 Å to 90 Å while keeping all other process parameters the same. Optical microscopy, scanning electron microscopy as well as X-ray diffraction analysis was carried out on the absorber film to understand the effect of sodium content on the film properties. It was found that the degree of preferred orientation increased with increasing sodium content. However, there was no significant improvement in the surface morphology of the films beyond the optimal sodium content. Cells were completed on the absorber films with varying NaF thickness. Based on the device measurements it was concluded that 30 Å NaF was the optimal thickness for very thin absorber film prepared in conventional furnace. In comparison to the earlier work carried out at FSEC on thicker absorber films, it was observed that the optimum amount of sodium required in case of thinner absorber films was lower than that required for thicker absorber films. For the cell completed on absorber film with higher NaF thickness the device performance degraded. To the best of our knowledge, it is the first time where the detrimental effects of excess sodium based on PV parameters obtained from experimental data have been reported. The current density and the open circuit voltage were significantly reduced with increasing NaF thickness. It is suggested here that increasing p-type conductivity beyond the optimal value causes tunneling enhance recombination causing the voltages to drop and the narrowing depletion width causes the electron-hole pairs to be created beyond the diffusion length, thus causing collection issues resulting in dropping currents. Very thin (<1 μm) CIGS thin film solar cells were prepared in the conventional furnace using the optimal selenization time of 30 minutes and the optimal NaF thickness of 30 Å. Highest efficiency of 6.26% as measured at FSEC was achieved.

Experiments with varying NaF thickness were carried out for absorber films prepared by RTP. It was essential to carry out these experiments to verify if the optimal amount of sodium was process dependant. Very thin (<1 μm) CIGS absorbers were prepared by RTP with varying NaF thickness. Cells were completed on the absorbers and I-V measurements were carried out. Based on the experiments it was concluded that optimal NaF thickness required for absorbers prepared by RTP is 90 Å. Thus it can be safely said that the optimum amount of sodium required while preparing absorber films is dependent on the process used for preparation of the absorber as well as on the thickness of the absorber film. Experiments were carried out by changing the sulfurization time for CIGSeS absorber films. For sulfurization to occur it is essential that the films are partially selenized. Therefore, the selenization time was reduced for these experiments. The devices were completed and I-V measurements were carried out. It was found out that sulfurization time of 1 minute was optimal for very thin absorber films. On increasing the sulfurization time the shunt resistance and the reverse saturation current degraded significantly. Very thin (<1 μm) CIGSeS thin film solar cells were prepared by RTP using the optimal sulfurization time of 1 minute, selenization of 2 minutes and the optimal NaF thickness of 90 Å. Highest efficiency of 6.58% as measured at FSEC was achieved.

The best cell was sent to NREL for measurement since it was known from earlier work that the efficiency as measure at NREL was at least 2-3% more as compared to efficiency as measured at FSEC. Highest efficiency of 8.65% was achieved on very thin (<1 μm) CIGSeS thin film solar cells. By calculating the efficiency per unit thickness it is possible to compare the efficiency achieved on thinner and thicker absorber films prepared by the same process. Based on this calculation it was found that the efficiency for optimized thinner devices was 9.6%/μmas

compared to 5.49%/μm for optimized thicker devices. In other words, a thickness reduction of 64% resulted in an efficiency drop of 32%. Thus it can be said that thinner CIGSeS devices can help in reducing the cost of production without significantly affecting the efficiency. It should be noted that further optimization of the thinner devices can be achieved and some suggestion for improving the device performance have been provided later in this section as future work.

It has been accepted in the industry so far that a very thin barrier layer is acceptable. It was believed that the very thin barrier layer would not complete eliminate the out diffusion of sodium from the soda lime glass, however, it would be sufficient to eliminate the micrononuniformities. Experiments were carried out to verify if this assumption was correct. Various thicknesses of silicon nitride barrier layers were deposited prior to molybdenum deposition. The silicon nitride barrier layer thickness was varied from 0 Å to 1200 Å. Optical microscopy and scanning electron microscopy analyses were carried out on the absorber films. The observations made from this experiment complemented the conclusions from earlier experiments with varying NaF thickness. I-V measurements were carried out on the devices and it was found that the device performance degraded with increasing silicon nitride thickness. It was found that the device performance did not degrade further beyond silicon nitride thickness of 800 Å. Based on this result it can be concluded that 800 Å is the optimal silicon nitride barrier layer thickness for reducing the sodium out diffusion from glass to the minimal and negligible level. Moreover, with further increasing the barrier layer thickness there is a possibility of delamination due to the stress built in thicker films.

Effect of working distance on the properties of sputtered molybdenum film was studied. It was found that by changing the working distance the properties of the plasma change and

higher energy atoms are generated and that as the working distance reduces the kinetic energy of the sputtered atoms is in the higher energy region for a large range of sputter power and working gas pressure. Hence, no significant variation in resistivity of films deposited at various sputter process parameters was observed. With the reduced working distance it was possible to control the residual compressive stress in deposited molybdenum films which was not possible at the larger working distance.

***Future work***

Systematic study was carried out to understand the effect of sodium on very thin absorber films. Based on the efficiencies achieved on thinner absorber films, it would be worthwhile to probe further and improve the efficiency of the devices. The current loss due to the thinner absorber can be compensated by experimenting with alternative higher bandgap heterojunction partners such CdZnS. Higher bandgap heterojunction partners would enable the absorption of blue photons thus increasing the total current d-ensity. Another observation made during this work was that the surface roughness was reduced with decreasing absorber thickness. Hence it is it suggested that experiments be carried out to reoptimize the thickness of the i-ZnO layer. With smoother absorber films, it might be possible to reduce the i-ZnO thickness in order to reduce the series resistance without reducing the shunt resistance and thus improve the fill factor.

Scientific and Engineering contributions made through this research effort are as follows;

1. It was proved that optimal amount of sodium required for device quality films is process dependent. This means it is essential to optimize the sodium precursor thickness every time the absorber preparation process is altered.

2. The detrimental effects of excess sodium were proved by experimental data. The effect on various PV parameters was explained based on the available models.
3. It was found that the assumption that a thin barrier layer is sufficient to avoid micrononuniformity in the absorber layer was wrong and that there exists an optimal thickness for the barrier layer to successfully reduce the amount of sodium out diffused from sodalime glass to negligible values beyond which it becomes possible to provide an optimum amount of NaF to avoid the occurrence of micrononuniformity.
4. It was shown that the effect of working distance is not just linked to the mean free path of sputtered atoms but it also alters the plasma properties and thus it is possible to better control the residual stress in the molybdenum thin films.

# APPENDIX A: Degree of Preferred Orientation Calculation

The intensities of all the CIGSe or CIGSeS reflections were determined by integrating the areas below the peaks. The ratio of the each intensity was calculated with respect to the total area of intensities of all the peaks. The integrated intensities of the XRD data of a randomly prepared (usually a powder) sample are usually considered to calculate the degree of preferred orientation. The JCPDS data is from a randomly prepared sample. Hence to calculate the degree of preferred orientation the JCPDS data was used for the comparison. The degrees of preferred orientation for the three peaks with highest intensity are provided below.

Degree of preferred orientation calculations for CIGS thin film absorber without NaF

| **JCPDS** | | **Peak** | **No NaF** | | | **Degree of Preferred Orientation** |
|---|---|---|---|---|---|---|
| **Intensity** | $\frac{Peak\ Area}{\sum Peak\ Areas}$ | | **Area** | **2θ** | $\frac{Peak\ Area}{\sum Peak\ Areas}$ | |
| 100 | 0.364 | 112 | 874 | 26.68 | 0.344 | 0.945 |
| 80 | 0.291 | 220/204 | 463 | 44.28 | 0.182 | 0.627 |
| 50 | 0.182 | 312/116 | 247 | 52.50 | 0.097 | 0.536 |

Degree of preferred orientation calculations for CIGS thin film absorber with 30 Å NaF

| **JCPDS** | | **Peak** | **40 Å NaF** | | | **Degree of Preferred Orientation** |
|---|---|---|---|---|---|---|
| **Intensity** | $\frac{Peak\ Area}{\sum Peak\ Areas}$ | | **Area** | **2θ** | $\frac{Peak\ Area}{\sum Peak\ Areas}$ | |
| 100 | 0.364 | 112 | 905 | 26.66 | 0.356 | 0.977 |
| 80 | 0.291 | 220/204 | 534 | 44.28 | 0.210 | 0.724 |
| 50 | 0.182 | 312/116 | 295 | 52.44 | 0.116 | 0.639 |

Degree of preferred orientation calculations for CIGS thin film absorber with 90 Å NaF

| **JCPDS** | | **Peak** | **80 Å NaF** | | | **Degree of Preferred Orientation** |
|---|---|---|---|---|---|---|
| **Intensity** | $\frac{Peak\ Area}{\sum Peak\ Areas}$ | | **Area** | **2θ** | $\frac{Peak\ Area}{\sum Peak\ Areas}$ | |
| 100 | 0.364 | 112 | 1139 | 26.70 | 0.448 | 1.231 |
| 80 | 0.291 | 220/204 | 509 | 44.32 | 0.200 | 0.688 |
| 50 | 0.182 | 312/116 | 280 | 52.40 | 0.110 | 0.604 |

# REFERENCES


[1] Stern Review: The Economics of Climatic Changes

[2] K. Zweibel, "Harnessing Solar Power-the Photovoltaic Challenge", Plenum, New York (1990)

[3] D.M.Chapin et al, "A New Silicon P-N Junction Photo-cell for Converting Solar Radiation into Electrical Power" Journal of Applied Physics, 25, 676, (1954)

[4] D.C. Reynolds et al, "Photovoltaic Effect in Cadmium Sulfide", Physical Review, 96:533–534, (1954)

[5] Y. Hamakawa, "Thin Film Solar Cells: Next Generation Photovoltaics and its Application", Springer, Germany (2004)

[6] M.A.Green et al, "Solar Cell Efficiency Tables (Version 31)", Prog. Photovolt: Res. Appl.,16,61, (2008)

[7] W.Horig et al, "The Optical Properties of $CuInSe_2$ Thin Films", Thin Solid Films, 48, 67, (1978)

[8] B.J.Stanbery, "Copper Indium Selenides and Related Materials for Photovoltaic Devices", Critical Reviews in Solid State and Materials Sciences, 27(2), 73, (2002)

[9] J.Kessler et al, "Electro-optical and Photoelectrochemical Studies of $CuIn_3Se_5$ Chalcopyrite Films", Proceedings of the 23rd Photovoltaics Specialist Conference, 549, (IEEE, 1993)

[10] A.Rockett et al, "Current Status and Issues in Polycrystalline $CuInSe_2$ for Photovoltaics application", Proceedings of the MRS Meeting, V426, 143, (1996)

[11] T. Haalboom, T. Gödecke, F. Ernst, M. RuHle, R. Herberholz, H.W. Schock, C. Beilharz and K.W. Benz, "Phase Relation and Microstructure in Bulk Materials and Thin Films of

the Ternary System Cu-In-Se," *Proceedings of the 11th International Conference on Ternary and Multinary compounds*, ICTMC-11, University of Salford, 249, (1997)

[12] L.L.Kazmerski et al, "Growth and Characterization of Thin Film Compound Semiconductor Heterojunctions", Journal of Vacuum Science Technology, 13, 65, (1977)

[13] N.G.Dhere et al, "Composition and structure of CuInSe2 thin films prepared by vacuum evaporation of the constituent elements", Solar Cells, 13, 59, (1984)

[14] W.E.Devaney et al, "Vacuum Deposition Processes for $CuInSe_2$ and $CuInGaSe_2$ Based Solar Cells", Solar Cells, 24, 19, (1988)

[15] R.W.Birkmire et al, "High Efficiency $CuInSe_2$ Based Heterojunction Solar Cells: Fabrication and Results", Solar Cells, 16, 419, (1986)

[16] L.D.Laude et al, "Laser-induced Synthesis of Thin $CuInSe_2$ Films", Solar Cells, 16, 199, (1986)

[17] M.C.Joliet et al, "Laser-induced synthesis of thin $CuInSe_2$ films", Applied Physics Letter, 46, 266, (1985)

[18] R.D.L.Kristensen et al, "Flash Evaporation of $CuInSe_2$ Films", Solar Energy Material, 17, 329, (1988)

[19] N.Romeo et al, "Growth of Large-grain $CuInSe_2$ Thin-Films by Flash-Evaporation and Sputtering", Solar Cells, 16, 155, (1986)

[20] T.F.Ciszek, "Growth and Properties of $CuInSe_2$ Crystals Produced by Chemical Vapor Transport with Iodine", Journal of Crystal Growth, 70, 405, (1984)

[21] C.W.Bates Jr., et al, "Spray Pyrolysis and Heat Treatment of $CuInSe_2$ for Photovoltaic Applications", Thin Solid Films, 88, 279, (1982)

[22] J.Bougnot, et al, “Chemical Spray Pyrolysis of $CuInSe_2$ Thin Films”, Solar Cells, 16, 221, (1986)

[23] J.Piekoszewski, et al, “RF-Sputtered $CuInSe_2$ Thin Films”, Solar Energy Material, 2, 363, (1980)

[24] B.Schumann, et al, “Epitaxial Layers of $CuInSe_2$”, Solar Cells, 16, 43, (1986)

[25] N.Takenoshita, “Liquid Phase Epitaxial Growth and Electrical Characterization of $CuInSe_2$”, Solar Cells, 16, 65, (1986)

[26] Y.Ueno, et al, “Electrodeposition of $CuInSe_2$ Films from a Sulphate Bath”, Thin Solid Films, 157, 159, (1988)

[27] V.K.Kapur, et al, “Low Cost Methods for the Production of Semiconductor Films for $CuInSe_2$/CdS Solar cells”, Solar Cells, 21, 65, (1987)

[28] V.K.Kapur, et al, “Non-vacuum Processing of $CuIn_{1-x}Ga_xSe_2$ Solar Cells on Rigid and Flexible Substrates using Nano-particle Precursor Inks”, Thin Solid Films, 53, 431, (2003)

[29] N.G.Dhere, et al, “CIGS2 Thin-Film Solar Cells on Flexible Foils for Space Power”, Prog. Photovolt: Res. Appl., 10, 407, (2002)

[30] G.Hades, et al, “Electroplated $CuInS_2$ and $CuInSe_2$ Layers: Preparation and Physical and Photovoltaic Characterization”, Thin Solid Films, 128, 93, (1985)

[31] B. M. Basol, et al, “$Cu(In,Ga)Se_2$ Thin Films and Solar Cells Prepared by Selenization of Metallic Precursors”, Journal of Vacuum Science and Technology, 14(4), 2251, (1996)

[32] S.F. Chichibu, M. Sugiyama, M. Ohbasami, A. Hayakawa, T. Mizutani, H. Nakanishi, T. Negami and T. Wada, "Use of diethylselenide as a less-hazardous source for preparation of

CuInSe2 photo-absorbers by selenization of metal precursors," Journal of Crystal Growth, 243, 404, (2002)

[33] A. Kadam, "Preparation of efficient $CuIn_{1-x}Ga_xSe_{2-y}S_y$/CdS thin-film solar cells by optimizing the molybdenum back contact and using diethylselenide as selenium precursor," Orlando, Fla.: University of Central Florida; 139, (2006); Available: http://purl.fcla.edu/fcla/etd/CFE0001035

[34] J.J.Loferski, "Theoretical Considerations Governing the Choice of the Optimum Semiconductor for Photovoltaic Solar Energy Conversion", Journal of Applied Physics, 27, 777, (1954)

[35] W.S.Chen et al, "Development of Thin Film Polycrystalline $CuIn_{1-x}Ga_xSe_2$ Solar Cells", Proceedings of the 23rd Photovoltaics Specialist Conference, 577, (IEEE, 1993)

[36] D.S.Albin et al, "A Study on the Optical and Microstructural Characteristics of Quaternary CIGS Polycrystalline Thin Films", Proceedings of the 21st Photovoltaics Specialist Conference, 562, (IEEE, 1990)

[37] W.N.Shafarman et al, "Characterization of $CuInSe_2$ Solar Cells with High Ga Content", Proceedings of the 25th Photovoltaics Specialist Conference, 898, (IEEE, 1995)

[38] S.H. Wei, et al, "Band offsets and optical bowing of chalcopyrites and Zn-based II-VI alloys", Journal of Applied Physics, 78, 3846, (1995)

[39] M.A. Contreras et al, "High efficiency graded bandgap thin-film polycrystalline Cu(In,Ga)Se2-based solar cells", Solar Energy Materials and Solar Cells, 41/42, 231, (1996)

[40] Ingrid Repins et al, "19.9% efficient ZnO/CdS/$CuInGaSe_2$ Solar Cell with 81.2% Fill Factor", Prog. Photovolt: Res. Appl., 16, 235, (2008)

[41] M. Bär, W. Bohne, J. Röhrich, E. Strub, S. Lindner, M. C. Lux-Steiner, Ch.H. Fischer, T. P. Niesen and F. Karg, "Determination of the band gap depth profile of the pentenary Cu(In1−XGaX)(SYSe(1−Y))2 chalcopyrite from its composition gradient", Journal of Applied Physics, 96, 7, 3857, (2004)

[42] T. Nakada, et al, "Improved Cu(In,Ga)$(S,Se)_2$ Thin Film Solar Cells By Surface Sulfurization", Solar Energy Materials and Solar Cells, 49, 285, (1997)

[43] S.H.Wei, et al, "Effects of Na on the Electrical and Structural Properties of $CuInSe_2$", Journal of Applied Physics, 85, 7214, (1999)

[44] M.A.Contreras, et al, "On the Role of Na and Modifications to Cu(ln,Ga)$Se_2$ Absorber Materials Using Thin-MF (M=Na, K, Cs) Precursor Layers", Proceedings of 26$^{th}$ Photovoltaic Specialists Conference, 359, (IEEE, 1997)

[45] D.Braunger, et al, "Polycrystalline Cu(In,Ga)$Se_2$ Solar Cells", 2$^{nd}$ World Conference of Photovoltaic Solar Energy Conversion, 511, (1998)

[46] D. Braunger, D. Hariskos, G. Bilger, U. Rau and H.W. Schock, "Influence of sodium on the growth of polycrystalline Cu(In,Ga)Se2 thin films," Thin Solid Films, 361, 161, (2000)

[47] S. H. Wei, S. B. Zhang, and A. Zunger, "Effects of Na on the electrical and structural properties of CuInSe2," Journal of Applied Physics, 85, 10, 214, (1999)

[48] D. Rudmann, D. Bremaud, A.F. da Cunha, G. Bilgec, A. Strohc, M. Kaelin, H. Zogga, A.N. Tiwarid, "Sodium incorporation strategies for CIGS growth at different temperatures" Thin Solid Films, 480, 55, (2005)

[49] Jorg Palm , Volker Probst, Franz H. Karg, “Second generation CIS solar modules” Solar Energy, 77, 757, (2004)

[50] K. Granath, M. Bodegard, and L. Stolt, “The effect of NaF on Cu(In,Ga)Se2 Thin Film Solar Cells,” Solar Energy Materials and Solar Cells, 60, 279, (2000)

[51] J. E. Granata, J. R. Sites, S. Asher, and R. Matson, “Quantitative incorporation of sodium in CuInSe2 and Cu(In,Ga)Se2 photovoltaic devices,” Proceedings of 26th IEEE Photovoltaic Specialists Conference, 387, (IEEE 1997)

[52] Rockett, J. S. Britt, T. Gillespie, C. Marshall, M. M. Al Jassim, F. Hasoon, R. Matson, and B. Basol, "Na in selenized Cu(In,Ga)Se2 on Na-containing and Na-free glasses: Distribution, Grain structure, and Device performances," Thin Solid Films, 372, 212, (2000)

[53] M. Ruckh, D. Schmid, M. Kaiser, R. Schaffler, T. Walter, and H. W. Schock, “Influence of substrates on the electrical properties of Cu(In,Ga)Se2 thin films,” Proceedings of the IEEE First World Conference on Photovoltaic Energy Conversion, 1, 156, (IEEE 1994)

[54] N. K. Shiro Nishiwaki, Takayuki Negami, and Takahiro Wada, "MoSe2 Layer Formation at the Cu(In,Ga)Se2/Mo Interfaces in High Efficiency Cu(In1-xGax)Se2 Solar Cells," Japanese Journal of Applied Physics, 37, L71, (1998)

[55] P. A. G. O'Hare, I. R. Tasker, J. M. Tarascon, “A Flourine-Combustion Calorimetric Study of Two Molybdenum Selenides: MoSe2 and Mo6Se6,” Journal of Chemical Thermodynamics, 19, 61, (1987)

[56] N. K. T. Wada, S. Nishiwaki, T. Negami, “Characterization of the Cu(In,Ga)Se2/Mo interface in CIGS Solar Cells,” Thin Solid Films, 387, 118, (2001)

[57] W. N. Shafarman and J. E. Phillips, "Direct current-voltage measurements of the Mo/CuInSe2 contact on operating solar cells," Proceedings of the 25th IEEE Photovoltaic Specialists Conference, 917, (IEEE 1996)

[58] D. F. M. R. Wurz, A. Meeder, A. Rumberg, S. M. Babu, Th. Schedel-Niedrig, U. Bloeck, P. Schubert-Bischoff, M. Ch. Lux-Steiner, "Formation of an Interfacial MoSe2 layer in CVD Grown CuGaSe2 Based Thin Film Solar Cells," Thin Solid Films, 431, 398, (2003)

[59] S.M.Sze, "Physics of Semiconductor Devices", Wiley, New York, (1981)

[60] Martin A.Green, "Solar Cells - Operating Principles Technology and Systems Applications", Prentice Hall Inc., (1982)

[61] A.M.Barnett et al, "Thin-film solar cells: A unified analysis of their potential", IEEE Trans. Elec. Dev., 27, 615, (1980)

[62] Orgassa K., et al, "Alternative back contact materials for thin film Cu(In,Ga)$Se_2$ solar cells", Thin Solid Films, 431-432, 387, (2003)

[63] K. Granath, et al, "Mechanical Issues of Mo Back Contact for Cu(In,Ga)$Se_2$", 13th European Photovoltaic Solar Energy Conference, 1983, (1995)

[64] V. Mohankrishanaswamy, "Processing and Characterization of CIGS Solar Cells", M.S. Thesis, University of South Florida, Tampa, (2004)

[65] J.H.Scofield et al, "Sputtered Mo Bilayer Contact for $CuInSe_2$ Based Polycrystalline Thin Film Solar Cells", Thin Solid Films, 260, 26, (1995)

[66] Hamda A. Al – Thani, Falah S. Hasoon, Matt Young, Sally Asher, Jeff L. Alleman, Mowafak M. Al – Jassim and Don L. Williamson, IEEE, 2002.

[67] I.Kaur, et al, "Growth Kinetics and Polymorphism of Chemically Deposited CdS Films", Journal of Electrochemical Society, 127, 943, (1980)

[68] D.Haneman, "Properties and Applications of Copper Indium Di-selenide", Critical Reviews in Solid State and Materials Sciences, 14, 377, (1988)

[69] K.Djessas, et al, "$CuInS_2$ Thin Films for Solar Cell Applications", Journal of Electrochemical Society, 147, 1235, (2000)

[70] D.Schmid, et al, "A Comprehensive Characterization of the Interfaces in Mo/CIS/CdS/ZnO Solar Cell Structures", Solar Energy Materials and Solar cells, 41/42, 281, (1996)

[71] M.A.Contreras, et al, "Optimization of CBD CdS process in high-efficiency $Cu(In,Ga)Se_2$-based solar cells", Thin Solid Films, 403, 204, (2002)

[72] R.H.Mauch et al, "Optimization of Windows in ZnO/CdS/CIS Heterojunctions", Proceedings of the 22nd Photovoltaics Specialist Conference, 8989, (IEEE, 1991)

[73] Y.Ohtake et al, "CIGS Thin Film Solar Cells with Continuously Evaporated Cd-Free Buffer Layer", Proceedings of the 25th Photovoltaics Specialist Conference, 549, (IEEE, 1995)

[74] R.Bhatt et al, "Dependence of Reactively Sputtered ZnO Electronic Properties on Growth Parameters for Use as a Buffer Layer in CIGS Solar Cells", Proceedings of the 26th Photovoltaics Specialist Conference, 383, (IEEE, 1997)

[75] S. Ishizuka, et al, "Fabrication of Wide-gap $Cu(In_{1-x}Ga_x)Se_2$ Thin Film Solar Cells: A Study on the Correlation of Cell Performance with Highly Resistive i-ZnO Layer Thickness", Solar Energy Materials and Solar Cells, 87, 541, (2005)

[76] N. G. Dhere, et al, “Development of CIGS2 Thin Film Solar Cells”, Materials Science and Engineering B, 116(3), 303, (2005)

[77] S. S. Kulkarni, “Design and Construction of Scrubber, Optimization of Sputter Deposition parameters and CdS Chemical Bath Deposition for Large Area CIGS2 Thin Film Solar Cells”, Master’s Thesis, University of Central Florida, (2003)

[78] Bhaskar Kumar, “Zinc Cadmium Sulphide And Zinc Sulphide as Alternative Heterojunction Partners for CIGS2 Solar Cells”, Master’s Thesis, University of Central Florida, (2007)

[79] Harshad P. Patil, “Study Of Transparent Conducting ZnO/ZnO:Al Layer, Front Grid Contact, for Photovoltaic Cells and Ruthenium Sulfide Photoanode for Photoelectrochemical Cells”, Master’s Thesis, University of Central Florida, (2003)